Defining the Nutrient Inputs that Support Pancreatic Cancer Metabolism

by

Peter N. Sajjakulnukit

A dissertation submitted in partial fulfillment
of the requirements for the degree of
Doctor of Philosophy
(Cancer Biology)
in the University of Michigan
2024

Doctoral Committee:

Professor Yatrik Shah, Chair
Professor Charles Burant
Associate Professor Alla Karnovsky
Associate Professor Costas Lyssiotis
Associate Professor Marina Pasca di Magliano

Peter N. Sajjakulnukit

pnsajja@umich.edu

ORCID iD: 0000-0002-8556-7481

Dedication

To my family, friends, peers, and all those who have supported me throughout the years with encouragement, faith, and laughter. And, most importantly, to all those afflicted by this terrible disease with the strength to keep fighting. To my peer Seth Boyer, to my friend Debbie Anderson, and to my family Phanu Limmanont and Shelley Trainor.

Acknowledgements

There are so many that have contributed to my journey as both a scientist and a person. I would first like to thank Mr. Paul Duffy, my high school biology teacher, who instilled a love of science in me from an early age and made school fun.

I would also like to thank Dr. Maureen Kachman, whom without none of this would have been possible. You took a chance on me and introduced me to science when I was very unsure of my future. You introduced me to metabolomics, my passion and career, and for that I will forever be grateful.

To my first boss and mentor Chuck, thank you for always being a steady, guiding force, and for always faithfully believing in me. Your support and unique perspective have continued to challenge me to think deeper and think broader.

To my mentor and friend Costas, thank you. Working with you these past seven years has been the best of my life. You took me in as a junior technician, pushed me in my pursuit of graduate school, and guided me throughout my graduate studies. You helped build me up from a one-dimensional student into a well-rounded academic weapon. Your enthusiasm for science and collaborative mindset has truly shaped my scientific journey thus far, and undoubtedly in the future. I look forward to many more years ahead as colleagues and friends.

I would like to thank my lab mates and collaborators. Your daily interactions and conversations, both scientific and not, have made my journey so enjoyable. Working alongside such great friends and colleagues makes science fun and a little more lighthearted. Specifically, past Lyssiotis Lab members: Barb Nelson, Dan Kremer, Hanna Hong, and Sam Kerk. You have helped guide me in science and in life, and I value our years together as such a fun group. To my collaborators: Dan Wahl, Tom Wubben, Yatrik Shah, Sriram Venneti, Carl Koschmann, and many, many others, I thank you for sharing your science with me and trusting in me to help.

To my friends, of which I have been so blessed to have many. To my Rochester friends who many have been by my side since first grade, I love you all. Blake, Mike, Jake, Abby, Dylan, and Evan, your close friendship over the years has meant the world to me and I love that we'll grow old together. To my Ann Arbor friends, thanks for all the memories, however clear they remain. From my undergrad friends Zack, Alex, Shean, Anna, and Adrienne, you always made Ann Arbor feel like home. Having Ann Arbor be my home for both undergrad and graduate school has blessed me with a whole new crew, of which I'd like to thank Shannon, Zach, Steve, Anne, and Ania. You all have continued to make Ann Arbor feel like home.

To the many iterations of Hillel Hockey, thanks for letting old man Pete keep playing over the last decade. Lessner, Benedek, Wink, Norty, Hank, and Fisch, you all kept me young and fun. To my Spicy Boys: Toes, Pav, Fletch, Darek, and Mike Low, thanks for the team bonding and making hockey feel like a family.

To my partner Natalie, thank you for loving me unconditionally and supporting me every day. You are truly a partner in every sense of the word, and I cannot wait for this next chapter of my life with you. What can't we do?

Finally, to my parents, Boonserm and Noppawan Sajjakulnukit. Thank you for all your support throughout my life. You have pushed me to become the man I am today, always holding me to a higher standard and believing in my success. You have sacrificed so much to set me up for success, and I do not take that for granted. I love you and thank you for everything.

Table of Contents

List of Tables

List of Figures

Abstract

Pancreatic ductal adenocarcinoma (PDA) is a particularly deadly form of cancer with a long-term survival rate of merely 12%. PDA is often detected in late stages and has few effective therapeutic options. This treatment evasion can be attributed largely in part to its surrounding tumor microenvironment (TME). PDA exists in a dense, highly fibrotic TME that results in hypoxia and a lack of serum-derived nutrients. To survive in these harsh conditions PDA rewires its metabolism and adapts its nutrient inputs. Understanding these cancer-specific pathways is vital in better characterizing PDA and identifying future therapeutic targets.

The aim of this work was to profile the nutrients capable of fueling PDA metabolism. In achieving this aim, we first employed a large-scale unbiased nutrient screen called the Biolog Mammalian Phenotyping Assay®, in which we cultured 20 PDA and two control cell lines in various nutrient-depleted conditions while providing them a wide array of substrates to measure metabolic activity rescue. Through this assay we profiled carbon and nitrogen-containing metabolites, a panel of ions, metabolic efforts, and chemotherapy drugs. From these data we chose to further investigate the carbon and nitrogen sources as potential rescue options for PDA metabolism.

Through these data we found that uridine consumption is markedly increased in PDA under nutrient-depleted conditions, and this strongly correlates to high expression of the enzyme uridine phosphorylase-1 (UPP1) which is responsible for catabolizing uridine into uracil and ribose 1-phosphate. Using metabolomics and several orthogonal methods, we demonstrate that

uridine-derived ribose enters central carbon metabolism to fuel glycolysis and oxidative phosphorylation, restoring PDA growth. Further, we show that PDA UPP1 expression is regulated by the KRAS-MAPK pathway, and expression is further increased upon nutrient-deprivation of glucose or uridine. Importantly, we demonstrate that UPP1 is active in mouse models, and following UPP1 knockout, uridine-derived carbons no longer enter oxidative metabolism, resulting in reduced tumor growth in an *in vivo* mouse model. These studies highlight the ability of PDA to utilize alternative substrates within the TME, while also providing a potential target for disrupting a cancer-specific pathway.

To further explore nutrients that support PDA growth, we looked at the effect of nitrogen-containing substrates in the Biolog assay. To achieve this aim, we used the statistical processing language R to collate and process the raw metabolic data from the large-scale assay. We calculated the maximum catabolic rate of each nitrogen-containing substrate and found glutamine-containing metabolites to consistently rescue PDA metabolism under nutrient-depleted conditions. Glutamine is the most abundant non-essential amino acid in circulation and provides a valuable source of both carbon and nitrogen in biochemical processes. Plotting the distribution of all glutamine-containing substrates, we observed a broad spectrum of catabolic rates, with glutamine-glutamine dipeptides being among the most rapidly consumed, and glutamine-glutamate among the slowest. These findings emphasize the role and importance of glutamine-derived carbon and glutamine-derived nitrogen and provoke future studies.

Overall, this work aims to profile the nutrient inputs that PDA is capable of consuming to support metabolism. By uncovering these alternate energy sources and pathways, we provide new and much needed insight into the characteristics of PDA and present future potential targets for metabolic therapies.

Chapter 1 Introduction to Pancreatic Cancer

1.1 Disease Overview

Cancer is among the leading causes of death worldwide, only second to cardiovascular disease[1]. In 2020, there was an estimated 1.8 million cancer diagnoses in the US alone, with an estimated 600,000 mortalities[1]. Encouragingly, the overall mortality rate of cancer-related deaths had decreased worldwide from 2005 to 2015[1]. This is due to early detection, and better characterization of cancer subtypes leading to more targeted therapies. However, as promising as these advances are, there are still many types of cancers that remain particularly deadly. When examining overall cancer incidence by type, the top four deadliest cancer types for men and women combined are lung, colorectal, pancreas, and breast[2,3]. Among these, pancreas cancer remains relatively stagnant in its treatment options and continues to grow in mortality rates[2,3].

Pancreatic ductal adenocarcinoma (PDA), the most common form of pancreatic cancer, is currently the third leading cause of cancer-related deaths and projected to increase to the second by 2040, only surpassed by lung cancer[2,3]. While PDA sits at 10th most common in incidence rate, it has the lowest 5-year survival rate among major cancer types making it a particularly important area of research. PDA accounts for 90% of all pancreatic malignancies, with the other major subtype, pancreatic neuroendocrine tumors (panNETs), presenting much more favorable prognoses[4]. Approximately 60-70% of PDAs are in the head of the pancreas, with the remainder residing in the body and tail regions[5].

A major reason why PDA is so deadly is that usually detected in late stages, as it is largely asymptomatic early on. When symptoms do present, they appear most commonly as abdominal pain, weight loss, asthenia, and jaundice[5]. In addition to the lack of symptoms, PDA currently has a severe lack of early detection markers. The location of the pancreas makes it a difficult organ to routinely examine, as it resides in the abdominal cavity behind the liver and stomach, and above the duodenum[6]. Overall, these factors contribute to the late-stage detection of PDA which presents limited treatment options and ultimately high mortality rates. The 5-year survival rate for PDA has increased painstakingly slowly in the past 50 years, from 2.5% in 1973 to merely 12% in 2023[5,7].

1.2 Therapeutic Landscape

Due to late-stage detection, only 15-20% of PDA diagnoses are available for resection[8]. The anatomical location of the pancreas results in complications in resection for late-stage tumors with vasculature intertwining multiple other organs. Additionally, there is often distant metastasis upon diagnosis, making removal of the primary tumor ultimately ineffective[8]. In the cases where resection is possible, a pancreaticoduodenectomy, or Whipple procedure, is common. This involves removing the head of the pancreas, along with portions of the small intestine, gallbladder, and bile duct in a major reconstructive procedure[9]. Even in these resectable cases, long term survival increases to merely 20%, serving to highlight the dismal prognosis for the majority of PDA cases and the disease overall[10].

Recent advancements in treatment options for other cancer types, most notably immune-checkpoint therapy, have proven to be largely ineffective in PDA[11]. This leaves the main treatment options to be chemotherapy and radiation. The standard of care for the last 50 years has been the chemotherapy regime of gemcitabine, with recent advancements in the last decade including combination chemotherapies[12]. The combination of 5-fluorouracil (5-FU), leucovorin, irinotecan, and oxaliplatin, commonly referred to as FOLFIRINOX, is the most aggressive therapy recommended for patients, although it generally requires patients to be in robust health due to significant side effects of treatment. The more palliative combination option is gemcitabine alongside an albumin nanoparticle conjugate of paclitaxel (nab-paclitaxel)[6]. These two therapies have emerged as the primary and secondary options for standard of care for PDA and are administered depending on the patient's progress and overall health.

1.3 PDA Tumor Microenvironment

PDA exists in a complex tumor microenvironment, a landscape surrounding the tumor that is wholly unique to other environments in the body. Within a PDA tumor, a majority of the tumor is comprised of non-cancer cells, consisting of fibroblasts, extracellular matrix (ECM), and a diversity population of inflammatory and immunosuppressive cells to support the tumor[6]. The high abundance of fibroblasts and ECM leads to a very dense, fibrotic, tumor microenvironment with interstitial pressures up to ten times to that of a normal organ. This structure serves as a physical barrier for the tumor from exposure to chemotherapies and anti-tumoral immune cell infiltration[13]. Studies have shown that combination therapies aimed at disrupting the ECM via depletion of hyaluronan, a major component of the ECM, improved chemotherapy efficacy with gemcitabine[14].

In addition to physical protection from therapies, the dense fibrotic environment commonly leads to a collapse and lack of penetrating vasculature, and a resulting lack of oxygen and serum derived nutrients. This results in the formation of a harsh and nutrient-deprived tumor microenvironment[13,15]. To survive and proliferate in this microenvironment, cancer cells can rewire their metabolic pathways to adapt to their presently available environment. This includes adapting their nutrient inputs to utilize those available, in the absence of classically consumed serum-derived nutrients. These nutrient inputs can be derived from the surrounding cells in the

TME in a symbiotic cellular crosstalk relationship, or by upregulated salvage pathways such as autophagy, a nutrient scavenging process regulated by nutrient access and energetic balance[16,17]. Through these mechanisms PDA rewires its metabolic pathways to adapt to and thrive. However, these altered pathways also present unique dependencies and sets the stage for future targeted therapies of these cancer-specific pathways.

1.4 Cancer Metabolism

In PDA, metabolic rewiring is largely affected by mutant KRAS (KRAS*), the main oncogenic driver. KRAS is a small GTPase that functions are a molecular switch induced by binding guanosine triphosphate (GTP) or guanosine diphosphate (GDP) to induce an active or inactive state, respectively. In quiescent non-cancerous cells, KRAS has low expression and remains in its inactive state for most of the time. KRAS is activated by extracellular stimulation of receptor tyrosine kinases (RTKs) or other cell-surface receptors, leading to active GTP binding and a signaling cascade to a multitude of regulatory signaling pathways for controlling mitotic processes. KRAS is mutated in almost all PDA, resulting constitutive activity and cancer promoting in its proliferative effects[18].

A majority of KRAS mutations occur as G12D and G12V, in which the glycine residue on codon 12 is mutated to an aspartate or valine, respectively[18]. With KRAS*, the main oncogenic driver in PDA great efforts have been made at targeting this GTPase. Historically, these efforts have been unsuccessful, leading many to label it as “undruggable”[19]. However, recent advancements have successfully developed small-molecule inhibitors capable of targeting KRAS* in multiple subtypes (G12C and G12D), showing great promise in clinical trials[19–21].

When KRAS* is constitutively active, many metabolic pathways are altered to benefit cancer cell survival. One such adaptation that has been well characterized is the use of glucose metabolism[15,22]. Glucose is the main serum-derived nutrient for cells and is utilized in the generation of ATP. Normally, under oxidative conditions this glucose is completely oxidized to carbon dioxide in the mitochondria to yield the highest amount of ATP[15]. However, due to the relative lack of vasculature and serum-derived nutrients glucose access is limited, resulting in KRAS* upregulating both the glucose transporter GLUT1 to promote glucose uptake, and glycolytic enzymes to promote glycolysis[22].

To recapture lost mitochondrial ATP production, KRAS* also rewires glutamine metabolism to fuel the TCA cycle and produce ATP[15]. Glutamine is a highly abundant non-essential amino acid and exists as a significant source of both carbon and nitrogen. KRAS* rewires glutamine metabolism by promoting its use as a carbon source in the TCA cycle for mitochondrial ATP used for proliferation[22,23]. Additionally, KRAS* promotes the use of glutamine for redox balance in a rewired malate-aspartate shuttle to counteract the collective ROS build up within cancer cells as a byproduct of their proliferation[22,24]. These alterations in metabolic pathways are driven by KRAS* to promote cancer cell survival in its TME, yet also present potential metabolic vulnerabilities that are cancer-specific, as these pathways are not dependent in non-cancerous cells.

In addition to adaptations in glucose and glutamine metabolism, PDA utilizes nutrient scavenging pathways in response to nutrient availability in the TME[25]. Autophagy is a nutrient scavenging process regulated by nutrient access and energetic balance that is shown to be upregulated in PDA[26-28]. Under conditions of metabolic stress, autophagy degrades cellular organelles and macromolecules to support metabolic homeostasis. This process provides amino acids that facilitate PDA growth under nutrient deprived conditions. Importantly, PDA is highly sensitive to autophagy inhibition, and studies have shown through both genetic and pharmacological inhibition of the autophagy pathway that tumor growth in PDA mouse models is reduced[26,28]. By inhibiting KRAS* downstream through the MAPK pathway, autophagy dependence is increased, leading to a synergistic effect in combination therapy of inhibiting both MAPK and autophagy *in vivo*[29]. These KRAS* driven adaptations demonstrate the metabolic plasticity of PDA cells and highlight the importance of understanding these characteristics in targeting this disease.

1.5 Metabolomics Overview

The substrates and small molecules that fuel and become byproducts of chemical reactions in biological systems are called metabolites. They consist of carbohydrates, nucleotides, amino acids, lipids, and many other biochemical classes[30,31]. These building blocks constitute the metabolome, which often has the strongest effects on biological phenotypes. This is due to the metabolome occurring downstream of both the transcriptome and genome. Therefore, when studying metabolism, it is essential to identify and quantify these small molecules, which is the overall aim of metabolomics.

To achieve this feat, an important technology is liquid-chromatography in tandem with mass spectrometry (LC/MS). Liquid-chromatography is a technique utilizing a column to separate metabolites based on chemical properties. While many column types exist, they generally consist of a stationary phase inside the column in conjunction with a mobile phase liquid being passed through the column[32,33]. The affinities for both the mobile and stationary phases result in separation of metabolites in a liquid sample across a given length and timeframe. The major column categories consist of hydrophilic interaction chromatography (HILIC) and reverse-phase chromatography (RPC), which separate polar metabolites based on hydro-affinity each in different gradient directions[34]. Between these two chromatography techniques, a significant amount of the metabolome can be separated.

After metabolite separation a mass spectrometer is utilized to detect and identify the metabolites within a sample by mass-to-charge ratios (m/z) and retention times (RT). The major components of a mass spectrometer include an ion source to convert compounds into ions; a mass analyzer to resolve these ions by time-of-flights or electromagnetic fields; and a detector to detect the ions and register the signals as m/z and abundance values[33]. The mass spectrometer can detect and quantify metabolites by measuring the m/z value as ions are passed to the detector. To increase the dynamic range of the instrument, the LC system is used to separate the sample across a range of time and stagger the ions as they reach the detector. Through the tandem LC/MS system thousands of metabolites can be quantified in a single experimental run.

1.5.1 Metabolomics Methods

There are many different applications for metabolomics, but almost all are derived from two major method categories: targeted and untargeted analyses[30,34]. When designing a targeted experiment, one has an identified list of metabolites of interest and the instrument 'looks' only for the metabolites of interest. This approach is generally used for hypothesis-driven experiments with a metabolic pathway of interest or mechanism of action being interrogated. By using a limited, known metabolite library, one can optimize metabolite isolation protocols, increase instrument detection sensitivity, run highly customized workflows such as absolute quantification with a standard ladder, and reduce analysis time. These approaches are quite powerful in cancer metabolism studies, as they can quickly and robustly profile multiple metabolic pathways in a single sample run, allowing comparison of metabolic profiles under given sample conditions, such as differing cancer types, or gene alterations.

While targeted methods are quick and offer more precise quantification, they rely upon verified standards and having a pre-defined metabolic pathway of interest. Thus, they are limited to preconceived knowledge. To broaden the scope of study, untargeted metabolomics methods can be employed. Untargeted methods aim to capture a full picture of the metabolome by measuring vast amounts of metabolites. These experiments generally are hypothesis-generating and aim to detect significant shifts in metabolic profiles or identify novel biomarkers and metabolites[35]. However, while metabolite coverage is increased, resolution and quantification may be sacrificed, as the experimental parameters are not optimized for such a broad spectrum of metabolite classes. Additionally, to capture unknown metabolites, the instruments use very loose filter settings, allowing most ions to reach the detector. This results in large datasets, commonly registering tens of thousands of significantly abundance signals, which are termed features. Features can be full metabolites, metabolites that have gained or lost atoms throughout the system from the formation of adducts or neutral losses, respectively, and occur as fragments, or artifacts within the sample. These ionizable species will be registered by the MS and outputted as a m/z value. Therefore, while the breadth of coverage is increased, the amount of effort needed to clean, process, and analyze the data is extensive and is a considerable hurdle in untargeted metabolomics[36]. Compound identification is commonly a rate-limiting factor in these studies[35].

1.5.2 Metabolomics Instrumentation

The instrumentation commonly used for targeted experiments is a triple quadrupole (QqQ) MS[30,33]. These instruments utilize three quadrupole mass analyzers in a series to quickly separate ions by mass. The first and third quadrupoles filter out masses based on user specifications, while the middle quadrupole acts as a cell for collision-induced dissociation. For example, if one was aiming to detect the metabolite lactic acid, a common metabolic byproduct and indicator of the glycolysis pathway, the instrument workflow would be as follows. First, the sample is separated by the LC system and continually ionized by the MS instrument ion-source as it enters the system. As lactate leaves the column, is ionized, and enters the MS it enters the first quadrupole (Q1), which is directed to let ions with a mass of 89 daltons (mass units) pass through and filter out the remainder. The second quadrupole (Q2) then emits a collision energy at the ion to fragment it into multiple pieces, which are then passed into the third quadrupole (Q3) which finally selects the desired fragment mass of 43.3 to be passed onto the detector to quantify the abundance of lactic acid. Through this workflow the instrument can increase sensitivity by pre-filtering for only the desired metabolite mass in Q1, and then reliably confirm metabolite identify by fragmentation patterns based on bond energies and structure in Q2 and Q3[30,33,37,38].

In these targeted QqQ experiments the instrument parameters for the acquisition method must be pre-defined, which usually involves purchasing commercially available metabolite standards to be run through the LC/MS system. This is necessary in determining the RT that the metabolite will come off the column and enter the MS at, and the Q1 and Q3 values to be filtered. Building a library of standards can be costly, but once achieved the method is capable of being quite robust, with LC separation and MS filtering allowing hundreds of metabolites to be detected in a single sample[30].

Untargeted experiments are commonly carried out by quadrupole time-of-flight (QTOF) instruments that differ from QqQ instruments by having the third quadrupole replaced with a time-of-flight tube[37]. This distinction offers greater mass accuracy due to the physical separation of ions within the flight tube, but with a concession to speed, generally leaning these experiments toward qualitative analysis rather than quantitative. Additionally, due to the lack of Q3 filtration

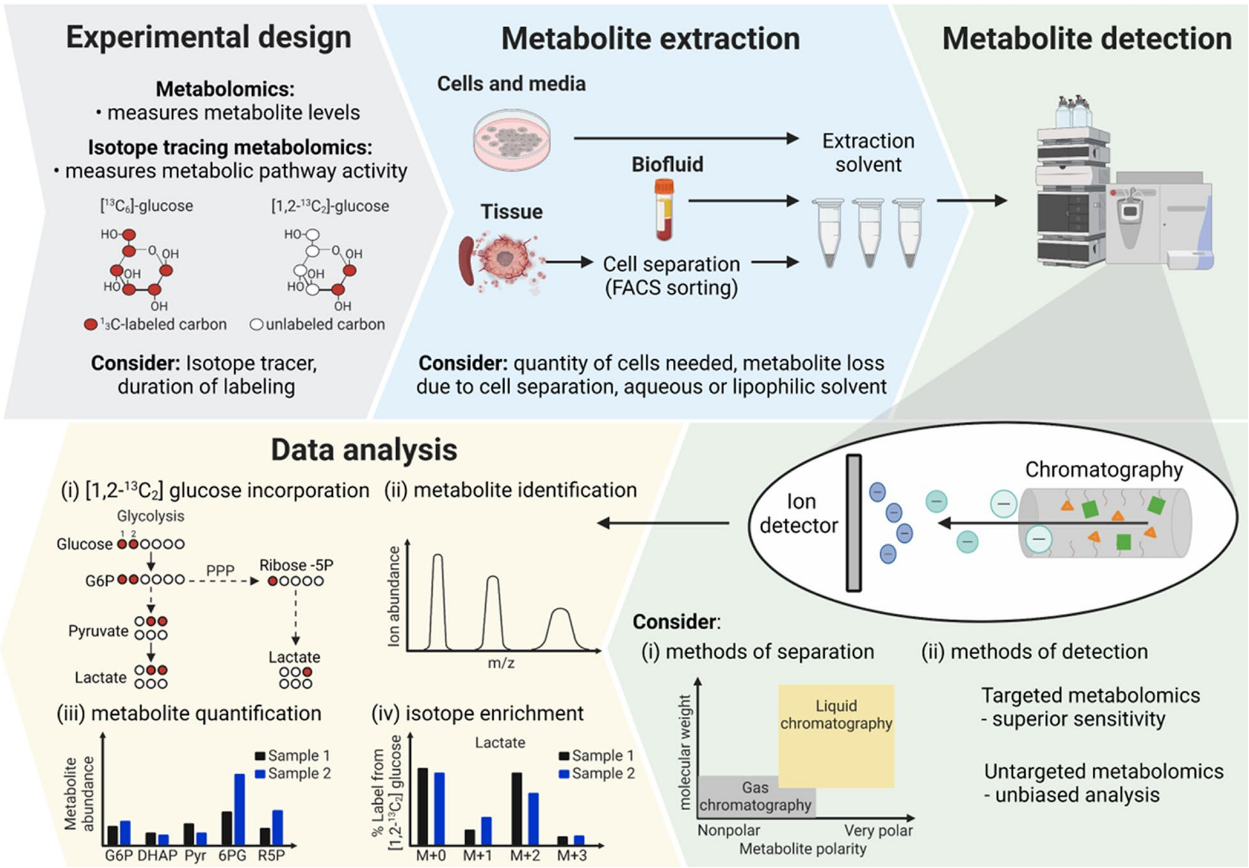

Figure 1-1. Workflow for metabolomics methods.

Experimental design consists of targeted or isotope tracing platforms. Metabolite extraction can be performed on *in vitro* or *in vivo* samples. Samples are analyzed via LC/MS tandem system, and data is processed for targeted metabolite lists or isotopologue distribution analysis.

all ions in the system will be passed to the detector, resulting in very large datasets with unnamed features, creating a bottleneck in data analysis[35].

1.6 Optimized Metabolomics Platforms in Cancer Research

Through metabolomics profiling, the Lyssiotis lab at the University of Michigan has come to see many metabolic phenotypes within different cancer cell types. There are many different classes of metabolites that contribute to central carbon metabolism and are each best extracted and detected under different ideal conditions. The Lyssiotis lab has established a robust method that is capable of simultaneously detecting a majority of the metabolic pathways in central carbon metabolism, including glycolysis, the tri-carboxylic acid (TCA) cycle, pentose phosphate, nucleotides, and amino acids[39] (**Fig. 1-1**). The single-solvent extraction protocol used in multiple studies[40–44]. This platform garners a "snapshot" of central carbon metabolism. This approach has identified alterations in essential bioenergetic pathways in various cancer studies.

In a study led by Dr. Daniel Kremer, it was found that the major PDA oncogene KRAS* upregulates the enzyme glutamate-oxaloacetate transferase 1 (GOT1) in a non-canonical pathway of the malate-aspartate shuttle (MAS) to support cancer cell redox balance. Inhibition of this pathway lead to redox imbalance, and primed PDA to be more susceptible to ferroptosis, an iron-dependent form of cell death[45]. This synergistic effect served to sensitize PDA to new therapeutic opportunities and was uncovered through the extensive use of metabolomics. First, glycolysis was identified to be increased following KRAS* induction. Metabolic pathways were then profiled upon GOT1 knockdown in cells, observing altered levels in redox intermediates. Finally, the snapshot metabolomics platform was used to quantify ferroptosis pathway intermediates to verify ferroptosis induction upon GOT1 knockdown. Through metabolomics and other orthogonal assays, a synergistic effect in GOT1 inhibition and ferroptosis efficacy in PDA was identified[45].

In addition to observing steady-state metabolite levels via targeted snapshot metabolomics, the Lyssiotis lab studies metabolic pathway flux and measures substrate-specific utilization to test hypotheses. This is achieved with stable isotope tracing, a method in which a substrate is modified by the addition of neutrons to create heavy isotopes, often ^{13}C carbon or ^{15}N nitrogen atoms. By incorporating these substrates into studies, it is possible to measure the given substrate's utilization into other metabolites in metabolic pathways by tracking the isotopic shifts in mass[46] (**Fig. 1-1**). This method is helpful in identifying dependency on a specific metabolic pathway. For example, in Chapter 2, the hypothesis proposes that uridine is catabolized by the enzyme uridine-phosphorylase-1 (UPP1) to be used as metabolic fuel in glycolysis. By using isotopically labeled ^{13}C-uridine, one can observe how the ^{13}C carbons from the substrate are incorporated into glycolysis with and without UPP1 active[47]. Additionally, stable isotope tracing can be used for metabolic flux profiling. In a study led by Dr. Nneka Mbah, diffuse intrinsic pontine glioma (DIPG) cells were profiled to identify metabolic changes based on their differentiated state, existing as stem-like glioma cells resembling oligodendrocyte precursors (OPC) or more differentiated astrocyte (AC)-like cells. By using ^{13}C-glucose OPC-like cells were shown to be more glycolytic than their AC-like counterparts, as well as demonstrating an upregulation in cholesterol metabolism[48]. Through these studies subtype-specific metabolic dependencies are identified and thus present new targeted therapy opportunities. The ability to measure metabolic flux as well as broad-scope steady-state metabolism highlights the versatility and utility in the metabolomics platforms developed in the Lyssiotis lab and their use in cancer metabolism studies.

1.7 Data Acquisition and Analysis Pipeline

Following data acquisition via LC/MS, extensive pre-processing, and quality control (QC) analysis of the raw data output is necessary before biological interpretations can be made from the data. To streamline reliability and reproducibility in our studies, a workflow has been created and optimized by using the programming language R to quickly clean and analyze targeted metabolomics data (**Fig. 1-2**)[39]. Metabolite abundance is quantified by measuring the area under the curve (AUC) of a peak, generally following a Bayesian distribution. Commonly, manual

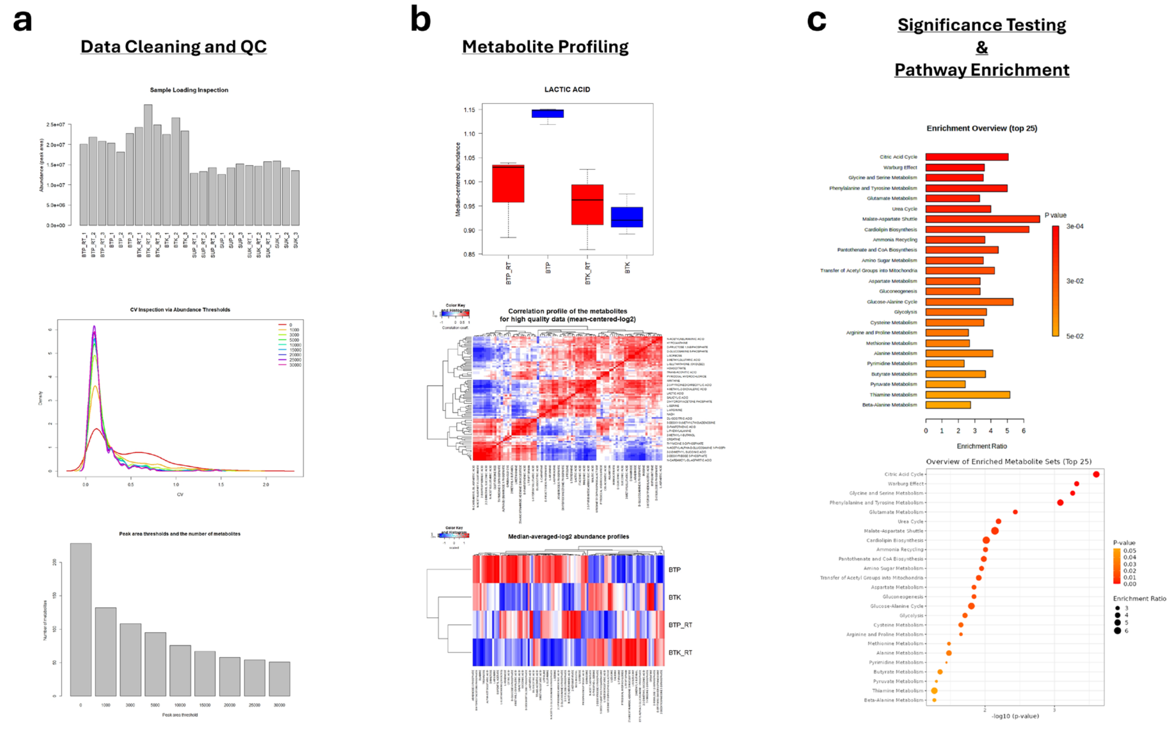

Figure 1-2. Metabolomics analysis pipeline.

Raw data is pre-processed and cleaned by inspecting CV distributions to determine an appropriate noise threshold. Samples loading is inspected and appropriately normalized. Metabolite abundance is individually plotted, as well as globally displayed on heatmaps. Significance tests are performed between sample classes and pathway enrichment analysis is performed via MetaboAnalyst.

inspection of peak integration within vendor software is required to verify that the peak shape is reliable and correctly integrated to avoid systematic errors in AUC calculations. After this inspection, a pivot table is commonly outputted from vendor software with AUCs representing metabolite ion abundance. These abundance counts represent relative values, and thus a standard curve must be applied to calculate absolute concentrations. From these values, one can determine the relative abundance difference for metabolites. To improve reliability and mitigate batch effects, concurrent runs are important to consider, as the instrument parameters may be altered from run-to-run, affecting the AUC values being reported. This consideration can reduce post-processing normalization needs and shorten analysis time.

To ensure reliably in biological analysis of samples, the data must be cleaned and QCed. First, samples are checked for missing values. If a metabolite value is missing in greater than 50% of samples in each experimental condition, that metabolite is discarded and deemed unreliable. For the remainder of missing values missingness is filled by calculating the median value of the metabolite from the technical replicates. Given that the MS is a quantitative system, we must check for equal sample loading. If a given sample is twice as concentrated as another, it will appear as a two-fold change in abundance, thus sample loading must be considered. Sample loading is inspected through both the total sum of metabolite abundance in each sample, and by plotting the log2 distribution of metabolites within a sample on a box plot to compare sample means. After sample loading checks, sample quality is further inspected through the coefficient of variance (CV) for each experimental condition. Given that experimental conditions in a study are comprised of technical replicates, the CV values are expected to be low, indicating metabolite stability and reproducibility. High CV values are also indicative of noisy, unreliable metabolites. Thus, we use a CV inspection to determine a noise threshold to reduce the dataset to quality metabolites (**Fig. 1-2a**).

From the remaining data, normalization techniques are applied by median centering the data and applying a log2 transformation. Z-scores are then calculated. The resulting output is a log2 fold-change value relative to the dataset population. From these results heatmaps are commonly employed to visualize the relative changes in metabolites between sample classes (**Fig. 1-2b**). Additionally, individual metabolites can be extracted and represented in box plots. Statistical tests (ANOVA, T-Test, Wilcoxon Test) are then performed for all permutations of experimental groups. Significantly altered metabolites are inputted into a pathway enrichment analysis via MetaboAnalyst to assess altered metabolic pathways between sample groups[49–51] (**Fig. 1-2c**).

1.8 Dissertation Summary

This work aims to characterize PDA metabolism by utilizing a variety of metabolomics techniques alongside a large-scale nutrient profiling assay to identify the nutrient inputs capable of fueling PDA growth. Here, by utilizing the Biolog assay and subsequent metabolomics experiments, we identified uridine as a novel nutrient source capable of fueling PDA metabolism via the enzyme uridine phosphorylase-1 (UPP1) **(Chapter 2)**. Additionally, we dove further into the Biolog phenotyping assay data to identify hypotheses on the role of nitrogen donor metabolites on PDA metabolism **(Chapter 3)**. While these studies present promising directions in targeted therapies in PDA metabolism there are significant follow-up studies to be performed **(Conclusions and Future Directions)**.

1.9 References

1. Nagai, H. & Kim, Y. H. Cancer prevention from the perspective of global cancer burden patterns. *J Thorac Dis* **9**, 448 (2017).

2. Rahib, L. *et al.* Projecting cancer incidence and deaths to 2030: The unexpected burden of thyroid, liver, and pancreas cancers in the united states. *Cancer Res* **74**, 2913–2921 (2014).

3. Rahib, L., Wehner, M. R., Matrisian, L. M. & Nead, K. T. Estimated Projection of US Cancer Incidence and Death to 2040. *JAMA Netw Open* **4**, e214708–e214708 (2021).

4. Kelgiorgi, D. & Dervenis, C. Pancreatic neuroendocrine tumors: the basics, the gray zone, and the target. *F1000Res* **6**, (2017).

5. Longo, D. L., Ryan, D. P., Hong, T. S. & Bardeesy, N. Pancreatic Adenocarcinoma. *https://doi.org/10.1056/NEJMra1404198* **371**, 1039–1049 (2014).

6. Halbrook, C. J., Lyssiotis, C. A., Pasca di Magliano, M. & Maitra, A. Pancreatic cancer: Advances and challenges. *Cell* **186**, 1729–1754 (2023).

7. Five-Year Pancreatic Cancer Survival Rate Increases to 12% - Pancreatic Cancer Action Network. https://pancan.org/news/five-year-pancreatic-cancer-survival-rate-increases-to-12/.

8. Kleeff, J. *et al.* Pancreatic cancer. *Nature Reviews Disease Primers 2016 2:1* **2**, 1–22 (2016).

9. Whipple Procedure (Pancreaticoduodenectomy) - Pancreatic Cancer Action Network. https://pancan.org/facing-pancreatic-cancer/treatment/treatment-types/surgery/whipple-procedure-pancreaticoduodenectomy/.

10. Tamburrino, D. *et al.* Selection criteria in resectable pancreatic cancer: A biological and morphological approach. *World Journal of Gastroenterology : WJG* **20**, 11210 (2014).

11. Zhang, Y. *et al.* PD-L1 and PD-L2 expression in pancreatic ductal adenocarcinoma and their correlation with immune infiltrates and DNA damage response molecules. *J Pathol Clin Res* **8**, 257–267 (2022).

12. Beutel, A. K. & Halbrook, C. J. Barriers and opportunities for gemcitabine in pancreatic cancer therapy. *Am J Physiol Cell Physiol* **324**, C540 (2023).

13. Ho, W. J., Jaffee, E. M. & Zheng, L. The tumour microenvironment in pancreatic cancer — clinical challenges and opportunities. *Nature Reviews Clinical Oncology 2020 17:9* **17**, 527–540 (2020).

14. Jacobetz, M. A. *et al.* Hyaluronan impairs vascular function and drug delivery in a mouse model of pancreatic cancer. *Gut* **62**, 112–120 (2013).

15. Halbrook, C. J. & Lyssiotis, C. A. Employing Metabolism to Improve the Diagnosis and Treatment of Pancreatic Cancer. *Cancer Cell* **31**, 5–19 (2017).

16. Yang, S. *et al.* Pancreatic cancers require autophagy for tumor growth. *Genes Dev* **25**, 717–729 (2011).

17. Lyssiotis, C. A., Kimmelman, A. C., Lyssiotis, C. A., Org, A. K. & Kimmelman, A. C. Metabolic Interactions in the Tumor Microenvironment. *Trends Cell Biol* **27**, 863–875 (2017).

18. Waters, A. M. & Der, C. J. KRAS: The Critical Driver and Therapeutic Target for Pancreatic Cancer. *Cold Spring Harb Perspect Med* **8**, (2018).

19. Huang, L., Guo, Z., Wang, F. & Fu, L. KRAS mutation: from undruggable to druggable in cancer. *Signal Transduction and Targeted Therapy 2021 6:1* **6**, 1–20 (2021).

20. Liu, J., Kang, R. & Tang, D. The KRAS-G12C inhibitor: activity and resistance. *Cancer Gene Therapy 2021 29:7* **29**, 875–878 (2021).

21. Kemp, S. B. *et al.* Efficacy of a Small-Molecule Inhibitor of KrasG12D in Immunocompetent Models of Pancreatic Cancer. *Cancer Discov* **13**, 298 (2023).

22. Ying, H. *et al.* Oncogenic Kras maintains pancreatic tumors through regulation of anabolic glucose metabolism. *Cell* **149**, 656–670 (2012).

23. Son, J. *et al.* Glutamine supports pancreatic cancer growth through a KRAS-regulated metabolic pathway. *Nature* **496**, 101–105 (2013).

24. Lyssiotis, C. A., Son, J., Cantley, L. C. & Kimmelman, A. C. Pancreatic cancers rely on a novel glutamine metabolism pathway to maintain redox balance. *Cell Cycle* **12**, 1987–1988 (2013). Biancur, D. E. *et al.* Compensatory metabolic networks in pancreatic cancers upon perturbation of glutamine metabolism. *Nature Communications* **8**, 15965 (2017).

25. Biancur, D. E. *et al.* Compensatory metabolic networks in pancreatic cancers upon perturbation of glutamine metabolism. *Nature Communications* **8**, 15965 (2017).

26. Yang, S. *et al.* Pancreatic cancers require autophagy for tumor growth. *Genes Dev.* **25**, 717–729 (2011).

27. Sousa, C. M. *et al.* Pancreatic stellate cells support tumour metabolism through autophagic alanine secretion. *Nature* **536**, 479–483 (2016).

28. Yang, A. *et al.* Autophagy Sustains Pancreatic Cancer Growth through Both Cell-Autonomous and Nonautonomous Mechanisms. *Cancer Discov* **8**, 276–287 (2018).

29. Bryant, K. L. *et al.* Combination of ERK and autophagy inhibition as a treatment approach for pancreatic cancer. *Nature Medicine* **25**, 628–640 (2019).

30. Patti, G. J., Yanes, O. & Siuzdak, G. Metabolomics: the apogee of the omics trilogy. *Nature Reviews Molecular Cell Biology 2012 13:4* **13**, 263–269 (2012).

31. Tan, S. Z., Begley, P., Mullard, G., Hollywood, K. A. & Bishop, P. N. Introduction to metabolomics and its applications in ophthalmology. *Eye 2016 30:6* **30**, 773–783 (2016).

32. Gika, H. G., Wilson, I. D. & Theodoridis, G. A. LC-MS-based holistic metabolic profiling. Problems, limitations, advantages, and future perspectives. *J Chromatogr B Analyt Technol Biomed Life Sci* **966**, 1–6 (2014).

33. Zhou, B., Xiao, J. F., Tuli, L. & Ressom, H. W. LC-MS-based metabolomics. *Mol Biosyst* **8**, 470–481 (2012).

34. Alpert, A. J. Hydrophilic-interaction chromatography for the separation of peptides, nucleic acids and other polar compounds. *J Chromatogr A* **499**, 177–196 (1990).

35. Schrimpe-Rutledge, A. C., Codreanu, S. G., Sherrod, S. D. & McLean, J. A. Untargeted metabolomics strategies – Challenges and Emerging Directions. *J Am Soc Mass Spectrom* **27**, 1897 (2016).

36. Kachman, M. *et al.* Deep annotation of untargeted LC-MS metabolomics data with Binner. *Bioinformatics* **36**, 1801–1806 (2020).

37. Dunn, W. B. Mass spectrometry in systems biology an introduction. *Methods Enzymol* **500**, 15–35 (2011).

38. Griffiths, J. A brief history of mass spectrometry. *Anal Chem* **80**, 5678–5683 (2008).

39. Lee, H. J., Kremer, D. M., Sajjakulnukit, P., Zhang, L. & Lyssiotis, C. A. A large-scale analysis of targeted metabolomics data from heterogeneous biological samples provides insights into metabolite dynamics. *Metabolomics* **15**, (2019).

40. Kim, P. K. *et al.* Hyaluronic acid fuels pancreatic cancer cell growth. *Elife* **10**, (2021).

41. Halbrook, C. J. *et al.* Macrophage-Released Pyrimidines Inhibit Gemcitabine Therapy in Pancreatic Cancer. *Cell Metab* **29**, 1390-1399.e6 (2019).

42. Venneti, S. *et al.* Clinical Efficacy of ONC201 in H3K27M-Mutant Diffuse Midline Gliomas Is Driven by Disruption of Integrated Metabolic and Epigenetic Pathways. *Cancer Discov* **13**, 2370–2393 (2023).

43. Peterson, E. R. *et al.* Adaptive rewiring of purine metabolism promotes treatment resistance in H3K27M-mutant diffuse midline glioma. *Res Sq* (2023) doi:10.21203/RS.3.RS-3317816/V1.

44. Ji, L. *et al.* Auditory metabolomics, an approach to identify acute molecular effects of noise trauma. *Scientific Reports 2019 9:1* **9**, 1–9 (2019).

45. Kremer, D. M. *et al.* GOT1 inhibition promotes pancreatic cancer cell death by ferroptosis. *Nature Communications 2021 12:1* **12**, 1–13 (2021).

46. Jang, C., Chen, L. & Rabinowitz, J. D. Metabolomics and isotope tracing. *Cell* **173**, 822 (2018).

47. Nwosu, Z. C. *et al.* Uridine-derived ribose fuels glucose-restricted pancreatic cancer. *Nature 2023 618:7963* **618**, 151–158 (2023).

48. Mbah, N. E. *et al.* Therapeutic targeting of differentiation state-dependent metabolic vulnerabilities in DIPG. *bioRxiv* 2022.03.01.482555 (2022) doi:10.1101/2022.03.01.482555.

49. Xia, J., Psychogios, N., Young, N. & Wishart, D. S. MetaboAnalyst: a web server for metabolomic data analysis and interpretation. *Nucleic Acids Res* **37**, W652–W660 (2009).

50. Lu, Y., Pang, Z. & Xia, J. Comprehensive investigation of pathway enrichment methods for functional interpretation of LC–MS global metabolomics data. *Brief Bioinform* **24**, (2023).

51. Xia, J. & Wishart, D. S. Web-based inference of biological patterns, functions and pathways from metabolomic data using MetaboAnalyst. *Nature Protocols 2011 6:6* **6**, 743–760 (2011).

Chapter 2 Uridine-Derived Ribose Fuels Glucose-Restricted Pancreatic Cancer[†]

2.1 Abstract

Pancreatic ductal adenocarcinoma (PDA) is a lethal disease notoriously resistant to therapy[1,2]. This is mediated in part by a complex tumor microenvironment (TME)[3], low vascularity[4], and metabolic aberrations[5,6]. Although altered metabolism drives tumor progression, the spectrum of metabolites used as nutrients by PDA remains largely unknown. Here, we identified uridine as a fuel for PDA in glucose-deprived conditions by assessing how >175 metabolites impacted metabolic activity in 21 pancreatic cell lines under nutrient restriction. Uridine utilization strongly correlated with expression of uridine phosphorylase 1 (UPP1), which we demonstrate liberates uridine-derived ribose to fuel central carbon metabolism and thereby support redox balance, survival, and proliferation in glucose-restricted PDA cells. In PDA, *UPP1* is regulated by KRAS-MAPK signaling and augmented by nutrient availability. Consistently, tumors express high *UPP1* compared to non-tumoral tissues, and *UPP1* expression correlated with poor survival in patient cohorts. Uridine is available in the TME, and we demonstrate that uridine-derived ribose is actively catabolized in tumors. Finally, UPP1 deletion restricted the ability of PDA cells to use uridine and blunted tumor growth in immunocompetent

---

[†] This chapter consists of a published primary article: Nwosu, Z. C.*, Ward, M. H.*, **Sajjakulnukit, P.***, Poudel, P.*, Ragulan, C., Kasperek, S., Radyk, M., Sutton, D., Menjivar, R. E., Andren, A., Apiz-Saab, J. J., Tolstyka, Z., Brown, K., Lee, H. J., Dzierozynski, L. N., He, X., Ps, H., Ugras, J., Nyamundanda, G., Zhang, L., Halbrook, C. J., Carpenter, E. S., Shi, J., Shriver, L. P., Patti, G. J., Muir, A., Pasca di Magliano, M., Sadanandam, A. & Lyssiotis, C. A. Uridine-derived ribose fuels glucose-restricted pancreatic cancer. ***Nature*** 2023 618:7963 618, 151–158 (2023).
*these authors contributed equally

mouse models. Our data identifies uridine utilization as an important compensatory metabolic process in nutrient-deprived PDA cells, suggesting a novel metabolic axis for PDA therapy.

2.2 Introduction

Pancreatic ductal adenocarcinoma (PDA) remains one of the deadliest cancers[1,2]. The PDA tumor microenvironment (TME) is a major contributor to this lethality and is characterized by abundant immune cell infiltration, expansion of stromal fibroblasts and the associated deposition of extracellular matrix. This leads to an increase in interstitial fluid pressure and collapse of arterioles and capillaries[3,4,7]. These phenomena collectively contribute to low oxygen saturation, therapeutic resistance, metabolic alterations, and heterogeneity within the tumor at the cellular level[5,8,9]. PDA cells surviving in such nutrient and oxygen deregulated TME exhibit metabolic adaptations that increase their scavenging and catabolic capabilities[10–13]. In addition, recent studies have defined tumor-extrinsic nutrient sources for PDA, including extracellular matrix, immune, and stromal-derived metabolites[14–16]. While these studies uncovered discrete nutrient inputs, comprehensive screens with the power to identify many such nutrient drivers and mechanisms have not been performed previously.

2.3 Results

Nutrient-deprived PDA consumes uridine

To screen for metabolites that fuel metabolism in nutrient-deprived PDA cells, we applied the Biolog phenotypic screening platform on 19 human PDA cell lines and two immortalized, non-malignant pancreas cell lines (hPSC and HPNE cells; **Fig. 2-1a**). We purposed the screen to assess cellular ability to capture and metabolize >175 nutrients in a 96-well arrayed format under nutrient limiting conditions (0 mM glucose, 0.3 mM glutamine, 5%

dialyzed fetal bovine serum). The nutrient panel included carbon energy and nitrogen substrates. Metabolic activity was assessed by monitoring the reduction of a tetrazolium-based dye, a readout of cellular reducing potential, every 15 minutes for ~3 days (**Fig. 2-1a**, **Fig. 2-5a**). Analyses of nutrient consumption profiles revealed several metabolites that, in the absence of glucose, were utilized at comparable levels as the glucose positive control (**Fig. 2-5b**). For example, adenosine, uridine and several sugars were utilized by most of the cell lines.

Uridine consumption correlates with UPP1

To select lead metabolites for investigation, we correlated metabolite utilization patterns to the expression of metabolism-associated genes using a public dataset[17,18]. From the top metabolite and gene correlation pairs (**Fig. 2-5c**), we pursued uridine and uridine phosphorylase 1 (*UPP1*) ($r = 0.82$, $P = 0.0002$, **Fig. 2-1b**) for the following reasons. First, *UPP1* expression correlated positively with the metabolic activity from its known substrate, uridine. Second, our *in vitro* validation showed that all tested PDA cells utilized uridine, though to varying degrees (**Fig. 2-1c; Fig. 2-5b**), suggesting it is a broadly used metabolic fuel. Third, contrary to our expectation that nutrients used in the absence of glucose would be carbohydrates, uridine was unusual in that it is a nucleoside. And, finally, UPP1-mediated uridine metabolism is unexplored in PDA.

We further confirmed the correlation of uridine catabolism and UPP1 expression by mRNA and protein analyses (**Fig. 2-1d-f**). To determine the specificity of this association, we assessed the correlation of *UPP1* expression to other nucleosides in the Biolog screen. While both inosine and adenosine were readily catabolized, their utilization was not correlated with *UPP1* expression. Thymidine was neither actively metabolized nor correlated, when compared to negative controls. (**Fig. 2-5d**). These results indicate that the association between *UPP1* expression and uridine catabolism is robust and specific.

Next, we rank-sorted the PDA cell lines into high and low uridine metabolizers based on the Biolog data, and identified >700 differentially expressed genes (P<0.05) between these groups using the Cancer Cell Line Encyclopedia (CCLE) data[19] (**Supplementary Table 2**). Consistent with our prior correlation analysis in a different dataset (**Fig. 2-5c**), *UPP1* was the topmost gene in uridine-high metabolizers in the CCLE dataset (**Fig. 2-1g**). Pathway analysis of the upregulated genes in the uridine-high metabolizers (i.e., *UPP1*-high cell lines) showed upregulation of endocytosis and several inflammation/immune-related pathways, notably NFκB signaling (**Supplementary Table 3**). We also observed that *UPP1*-high tumors exhibit higher expression of glycolysis genes (**Fig. 2-5e**), indicating a potential link between the UPP1-uridine axis and energy metabolism. In contrast, *UPP1*-high cell lines and UPP1-high patient tumors displayed a profound downregulation of other metabolic pathways (**Fig. 2-5f-g**), notably amino acid-, fatty acid- and glutathione metabolism, altogether indicating metabolic vulnerability.

Uridine-derived ribose fuels metabolism

Our screen (**Fig. 2-1a**) was performed in glucose-free media to reveal both metabolites whose use would otherwise be overshadowed by glucose and carbon sources that could act in place of glucose. Thus, we next directly assessed the metabolic activity of equimolar glucose and uridine. Across four PDA cell lines, uridine and glucose fueled metabolism to a similar degree (**Fig. 2-2a**). Previous reports have also documented that uridine can substitute for glucose, by supporting nucleotide metabolism[20–26]. However, our screening data illustrate that uridine supplementation increases cellular reducing potential. Together with the observed connection with UPP1, which catalyzes the cleavage of ribose 1-phosphate from uracil, we hypothesized that the UPP1-liberated ribose is recycled into central carbon metabolism to support cellular reducing potential. To test this hypothesis, we supplemented glucose-deprived cells with ribose, a cell-permeable substitute for ribose-1-phosphate. Indeed, like exogenous uridine, ribose supplementation fueled reducing potential (**Fig. 2-2a**).

In our initial screen, glutamine concentration was also intentionally low (0.3 mM), as it is an important anaplerotic substrate that fuels tricarboxylic acid (TCA) cycle and proliferation in PDA[27]. Uridine potentiated reducing potential with or without glutamine and had a greater impact when glutamine was present (**Fig. 2-6a**). Together, these data suggest that uridine and glucose similarly fuel central carbon metabolism distinctly from glutamine.

Next, we provided uridine to the UPP1-low, PATU8988S and the UPP1-high, DANG cell lines under glucose deprivation and applied liquid chromatography mass spectrometry (LC-MS)-based metabolomics[28]. In both cell lines, uridine supplementation led to the elevation of glycolytic intermediates and lactate secretion (suggesting glycolytic flux); uridine derivatives (suggesting overflow metabolism); amino acids (indicative of increased anabolism); and TCA cycle intermediates (suggesting more mitochondrial activity) (**Fig. 2-6b-e**). Moreover, supplementation with uridine led to marked accumulation of intracellular uridine and ~100-fold increase in media uracil content (**Fig. 2-2b,c, Fig. 2-6f-g**), consistent with uridine capture, ribose extraction, and uracil release. Notably, intracellular uracil increased by a fold comparable to uridine, reflective of direct substrate to product conversion (**Fig. 2-2b, Fig. 2-6f**). Collectively, these profiling efforts support the model that uridine is catabolized to broadly fuel PDA cell metabolism.

To precisely delineate how uridine is metabolized, we traced the metabolic fate of isotopically labelled uridine ($^{13}C_5$-uridine with labeled ribose carbon) using LC-MS[29] in PATU8988S (UPP1-low) and ASPC1 (UPP1-high) lines. Both lines demonstrated high uridine, UMP and UTP labeling (over 90%), as indicated by M+5 from ribose (**Fig. 2-2d**). Other nucleotides, such as ATP, ADP, AMP (all M+5) as well as NAD+ (M+5, M+10) were also labeled (**Fig. 2-2e, Fig. 2-6h**), demonstrating the use of uridine-derived ribose for ribosylation of the adenine base. Also labeled were glycolytic- (PEP, pyruvate, lactate), pentose phosphate pathway (PPP; xylulose 5-phosphate, ribose 5-phosphate), hexosamine biosynthetic pathway (UDP-GlcNAc), and TCA cycle intermediates (malate and citrate), as well as non-essential amino acids (aspartate, glutamate, serine), and oxidized glutathione (**Fig. 2-2f**, **Fig. 2-6h**).

To determine the relevance of uridine metabolism for pancreatic tumors *in vivo*, we implanted murine syngeneic pancreatic cancer cells into the pancreas of immunocompetent hosts to establish tumors. Then, we injected these animals with $^{13}C_5$-uridine or phosphate buffered saline vehicle and collected tumor tissues after one hour for LC-MS analysis. Consistently, we observed robust uptake of uridine by the tumor, with >30% of the pool labeled. We observed the M+5 label in pyrimidine and purine species (i.e., ribose salvage) as well as in glycolytic and TCA cycle intermediates (**Fig. 2-2g, Fig. 2-7a**). ^{13}C incorporation into the TCA cycle was low *in vivo*, presumably due to the short duration of labeling. Nearly identical results to those from orthotopic studies were similarly observed in subcutaneous tumors from immune competent animals. These results confirm that PDAs catabolize uridine *in vivo*.

In parallel, we collected tumor interstitial fluid (TIF) from independent orthotopic allograft tumors and quantified bulk uridine and glucose concentrations by LC-MS. Uridine and glucose were present in the low and high micromolar concentration range, respectively (**Fig. 2-**

2h-i), similar to previous findings[30]. To determine how physiological concentrations of glucose and uridine impacted uridine metabolism, we grew two PDA lines in 5 or 0.1 mM glucose and 0.1 or 1 mM $^{13}C_5$-uridine and analyzed labeling patterns. First, the labeling of uridine was near 100% (**Fig. 2-2j**). At equimolar concentrations, uridine carbon contributed to ~50% of several metabolites in the PPP, phosphoribosyl pyrophosphate (PRPP, in nucleotide biosynthesis), NAD+, upstream glycolysis, with enrichment exceeding 10% in some TCA cycle metabolites (**Fig. 2-2k, Fig. 2-7b**). With higher uridine (10:1), uridine carbon dominated, and with higher glucose (1:50), uridine carbon contributed at a much lower level, consistent with competition for these two carbon sources into the same pathways. Further isotope tracing using the exact TIF concentrations of uridine and glucose showed that both human (ASPC1) and murine (MT3-2D) cells incorporate uridine into central carbon metabolism (**Fig. 2-7c-d**). We confirmed these results in four human PDA lines with the tetrazolium assay: uridine supported bioenergetics at physiological (**Fig. 2-8a,b**) but not at elevated glucose levels (**Fig. 2-8c**).

Our data suggest that uridine yields ribose-1-phosphate via UPP1 to fuel both catabolic and biosynthetic metabolism. Ribose-1-phosphate can be converted into the PPP product ribose-5-phosphate by phosphoglucomutase 2 (PGM2) to enter nucleotide biosynthesis. Alternately, cells can convert uridine to uridine monophosphate (UMP) via uridine-cytidine kinase (UCK1/2) in the pyrimidine salvage pathway (**Fig. 2-8d**). We found that *PGM2* and *UCK2* are high in PDA and *UCK1* is low, but these genes were largely uncorrelated with *UPP1* mRNA expression (**Fig. 2-8e-h**). Being the most upregulated, we tested PGM2 by western blot and found it to be expressed in most PDA cells, and its expression was nor related to UPP1 (**Fig. 2-8i**). Inhibition of the three genes by siRNA showed that only PGM2 knockdown suppressed the uridine-mediated rescue of metabolic activity following glucose deprivation (**Fig. 2-8j-l**). Taken together, these data support our model that uridine catabolism converges with central carbon metabolism, and they also reveal that exogenous uridine fuels PDA metabolism akin to glucose, supplying carbon for redox-, nucleotide-, amino acid-, and glycosylation metabolite biosynthesis (**Fig. 2-2l**).

UPP1 provides uridine-derived ribose

To confirm the role of UPP1 in uridine catabolism, we knocked out UPP1 (UPP1-KO) using CRISPR/Cas9 in the PATU8988S (UPP1-low) and ASPC1 (UPP1-high) human PDA cell lines and validated two independent clones per cell line (**Fig. 2-3a**). In these knockouts, the ability of uridine to rescue NADH production in the absence of glucose (**Fig. 2-3b**) or cellular bioenergetics read out by ATP-based viability (**Fig. 2-3c**) was abolished. Consistent with the blockade of uridine catabolism, metabolomics showed that UPP1-KO cell lines displayed an increase in intracellular and extracellular uridine (**Fig. 2-9a,b**) accompanied by a marked drop in intracellular and extracellular uracil (**Fig. 2-3d, Fig. 2-9b**). Further, UPP1 knockout broadly altered the intracellular metabolome of both cell lines (**Fig. 2-9c**). Noteworthy, ASPC1 cells are highly sensitive to glucose deprivation in combination with UPP1-KO, thus metabolomics in this cell was performed after 6 hours when assessing the KO effect.

We next utilized our isotope tracing metabolomics platform to determine the impact of UPP1-KO on uridine catabolism in PATU8988S and ASPC1 cells (**Fig. 2-3e**, **Fig. 2-9d-k**). The ribose-labeled $^{13}C_5$-uridine tracing showed similar fractional enrichment of the intracellular uridine pool in the UPP1-KO and control cells (**Fig. 2-9d,e**), indicative of unchanged, steady-state uridine uptake. In contrast, and consistent with our model, flux of uridine ribose-derived carbon into glycolysis (**Fig. 2-3e, Fig. 2-9f**), TCA cycle-associated metabolites (**Fig. 2-3e, Fig.**

2-9g), non-essential amino acids (**Fig. 2-9h,i**), oxidized glutathione, and UDP-GlcNAc (in glycosylation), was holistically blocked or suppressed. Recycling of uridine-derived ribose was also completely blocked in the UPP1-KO cells, as evidenced by the absence of carbon labeling in NAD+ and bioenergetic metabolites AMP, ADP, and ATP (**Fig. 2-9j,k**). Together, these results reveal that the UPP1-mediated catabolism of uridine is indispensable for the utilization of uridine to support reducing potential, bioenergetics, and cell proliferation, and provide a detailed molecular confirmation that UPP1 directly controls the utilization of uridine-derived ribose in PDA cells.

High UPP1 in PDA predicts poor survival

To further assess the relevance of UPP1 in PDA tumors, we next analyzed its expression in publicly available human PDA datasets. Using The Cancer Genome Atlas (TCGA) data, we find that *UPP1* is highly expressed in PDA tumors compared to non-tumoral samples, and also in liver metastasis compared to primary tumors (**Fig. 2-3f**). Its paralog, *UPP2*, is not expressed in this tumor type (**Fig. 2-10a**). We also observed from the Human Protein Atlas public database that *UPP1* gene expression is extremely low in normal pancreas and *UPP1* protein is high in PDA (**Fig. 2-10b,c**). Consistently, *UPP1* is also high in several other non-PDA cancers from TCGA, with colon and prostate cancers being the notable contrast (**Fig. 2-10d**). Finally, as in PDA, high *UPP1* also predicted poor survival outcome in lung, stomach, liver and renal cancers (**Fig. 2-10e**). Indeed, we tested uridine utilization in several non-PDA cancer cell lines and observed a modest uridine-driven increase in metabolic activity (**Fig. 2-10f**), supporting the potential relevance of this metabolite in other cancers.

To independently validate UPP1 expression in human PDA, we utilized patient samples from the University of Michigan to assay tumoral *UPP1* expression by RNAscope (**Fig. 2-3g,h, Fig. 2-11a**), the cellular distribution of *UPP1* expression by single cell RNA sequencing (**Fig. 2-11b,c**), and UPP1 expression by immunohistochemistry (**Fig. 2-11d**). Collectively, these data were consistent with public databases, illustrating UPP1 upregulation in human PDA relative to normal pancreas tissue. In addition, our histological assessment of injured acinar cells indicated that UPP1 is upregulated upon pancreatic injury (**Fig. 2-11d**), suggesting a potential role in PDA formation. Finally, stratification of tumor datasets also showed that the high expression of *UPP1* predicted poor overall survival outcome in three of the four PDA patient cohorts we analyzed (**Fig. 2-3i, Fig. 2-11e**). Taken together, these data support that UPP1 is important in PDA.

Kras-MAPK pathway regulates UPP1

Kras mutations are the signature transforming event observed in the vast majority of PDA[31]. Using TCGA data, we determined that PDA with *KRAS* G12D express higher *UPP1* than those with no *KRAS* alterations (**Fig. 2-3j**). We also analyzed the CCLE protein expression data of *KRAS* wildtype vs. mutant cell lines across cancers and from lung or colorectal cancer. A targeted analysis of PDA lines was not performed because *KRAS* mutations are observed in all but one line in the CCLE. From the pan-analysis (n=374), we observed a borderline association between *KRAS* status and *UPP1* expression ($P = 0.09$) (**Fig. 2-12a**), but lung cancer cell lines (n=79) showed a strong association ($P = 0.003$). Colorectal cancer lines (n=30) showed no difference or slightly reduced *UPP1* in mutant *KRAS* lines (**Fig. 2-12a**), consistent with the data in **Fig. 2-10d**. The colon cancer results may be due to the timing of *KRAS* mutation in tumor evolution and differences in its tissue-specific function, relative to that of lung and PDA[32].

To experimentally test the role of mutant *Kras* on UPP1 expression, we first queried published microarray data from our doxycycline-inducible Kras (iKras) mouse model of PDA[33,34]. Mutant Kras promoted *Upp1* expression in a subcutaneous xenograft model *in vivo* and iKras PDA cell lines *in vitro* (**Fig. 2-12b**). Consistently, *in vitro* validation experiments in two additional, independent iKras cell lines confirmed doxycycline (Kras) induction of *Upp1* (**Fig. 2-3k-l**).

We previously showed that KRAS-mediated regulation of anabolic glucose metabolism in PDA occurs via mitogen-activated protein kinase (MAPK) signaling and MYC-dependent transcription[34]. In human and murine cell lines, the pharmacological inhibition of MAPK reduced UPP1 transcript and protein, concurrent with the suppression of pERK (**Fig. 2-3m,n**, **Fig. 2-12c-j**). MAPK inhibition also blocked the catabolism of uridine, reflected by intracellular uridine accumulation, a spectrum of other metabolite profile changes (**Fig. 2-12k**), and suppressed uridine-fueled proliferation (**Fig. 2-3o, Fig. 2-12l**). In contrast to our previous KRAS mechanism[34], MYC inhibition did not alter UPP1 expression nor appear among the transcription factors binding to the UPP1 promoter (**Fig. 2-13a-c**), suggesting that MYC does not mediate Kras regulation of UPP1 in PDA.

Nutrient availability modulates UPP1

Given that glucose availability influences the use of uridine-derived ribose, we hypothesized that a glucose-depleted microenvironment triggers PDA to upregulate UPP1 as a compensatory response. Indeed, the removal or reduction of media glucose induced a strong increase in UPP1 expression (**Fig. 2-3m-o, Fig. 2-12c-e, 8h-j, 9d**), which was attenuated in uridine-supplemented media. Consistently, we found that *Upp1* was strongly induced in a murine tumor-derived cell line from the KPC model (p48-Cre; LSL-Kras^{G12D}; LSL-P53^{R172H}) when cultured with tumor interstitial fluid media (TIFM)[30] or implanted as orthotopic allografts, relative to cells cultured in routine media with high glucose (**Fig. 2-13e**). Thus, KRAS-MAPK signaling and a nutrient-deprived TME may both be responsible for high UPP1 expression.

UPP1 knockout blunts PDA tumor growth

Uridine concentration is reported to be ~2-fold higher in TIF than plasma[30]. In looking for a cellular source of supplying uridine to tumors, we observed from our previously generated dataset[14] that macrophages release uridine and uracil *in vitro* when differentiated and polarized to a tumor-educated fate with PDA conditioned media (**Fig. 2-14a**). Thus, we tested the role of tumor associated macrophages (TAMs) in supplying intratumoral uridine by depleting macrophages from murine allograft tumors with colony stimulating factor 1 (CSF1) antibody and clodronate (liposome) combination (**Fig. 2-4a**), which depletes TAMs and suppressed orthotopic tumor growth[35,36] (**Fig. 2-4a,b**). We observed a reduction in the plasma uridine level by ~8 fold upon macrophage depletion, concomitant with an elevation in plasma uracil. However, TIF and tumor uridine and uracil were not altered (**Fig. 2-4c**, **Fig. 2-14b**). This marked impact on plasma uridine levels following macrophage depletion indicates that macrophages may be important mediators of uridine production/release.

To determine if UPP1 supports tumor growth *in vivo*, we generated two independent models of UPP1-KO in the syngeneic pancreatic cancer lines MT3-2D and KPC 7940b. Two sgUPP1 constructs (sg1, sg3) were compared to a vector control (sgVector). We confirmed that UPP1-KO cells were not rescued from glucose deprivation by uridine *in vitro* (**Fig. 2-4d**). Further, metabolomics profiling confirmed intracellular uridine accumulation and reduced intracellular and extracellular uracil (**Fig. 2-4e**), consistent with blocked uridine catabolism. These were accompanied by changes in a spectrum of other metabolites which were mirrored by the human UPP1-KO cell lines (**Fig. 2-4f**). Finally, isotope tracing of uridine ribose-derived carbon illustrated conclusively that UPP1-KO in the murine lines restricted the use of uridine to fuel central carbon metabolism (**Fig. 2-4g,h**). This battery of metabolic assays confirms successful UPP1 knockout in lieu of a murine UPP1 antibody. Notably, UPP1-KO cells did not differ from controls in terms of proliferation (**Fig. 2-14d**).

We implanted these two mouse lines and their KOs into the pancreas of syngeneic hosts and assessed tumor weight at endpoint (**Fig. 2-4i**). In both lines, contrary to the lack of a proliferative defect *in vitro*, we observed a marked reduction in tumor growth following UPP1-KO (**Fig. 2-4j, Fig. 2-14e**). Similar results were also reproduced in an immunocompetent subcutaneous model with the MT3-2D cell lines (**Fig. 2-4k**). Metabolomic profiling of the orthotopic tumors revealed an increase in tumoral uridine and a drop in uracil in all UPP1-KO tumors as well as a profound change in the metabolome relative to vector controls (**Fig. 2-4l-n**). In addition, compared to *in vitro* data, we observed the accumulation of a similar suite of metabolites (**Fig. 2-4m**) and a strong depletion of uracil, components of PPP, glycolysis and nucleotide metabolism (**Fig. 2-4n**).

The marked anti-tumor effect of UPP1-KO prompted us to look for changes in the *in vivo* microenvironment. Histological analysis of F4/80 staining revealed no differences in macrophage content between UPP1-KO and vector control tumors. However, the UPP1-KO tumors had lower vessel density (CD31) and more anti-tumor T cell infiltration (CD8 T cells) (**Fig. 2-14h**). Taken together, our data indicate that UPP1 and uridine are important in PDA growth. The contrast between *in vitro* and *in vivo* growth phenotype further highlights the role of nutrient availability, as well as potential involvement of the tumor microenvironment and immune cell subsets in influencing the necessity of UPP1 *in vivo*.

2.4 Discussion

The metabolic features of PDA drive disease aggressiveness and therapeutic resistance and present new opportunities for therapy[2,6]. Despite this, the range of nutrients used by PDA cells is poorly understood. We addressed this by applying a high-throughput *in vitro* nutrient screening and found that under glucose-restricted condition and KRAS-MAPK signaling activation, uridine serves as a nutrient source in PDA cells. This aligns with previous studies, where uridine rescued glucose deprivation-induced stress in astrocytes and neurons[20,21,23]. Indeed, others have shown that the uridine-mediated rescue is UPP1-dependent and induced by glucose availability, and it was proposed that UPP1 functions in this capacity to support bioenergetics by providing nucleotides[20]. We show that the uridine ribose ring fuels both energetic and anabolic metabolism in PDA cells. We also found that, in addition to KRAS-MAPK, the uridine utilization axis is regulated by a yet unknown rheostat sensing the upstream availability of glucose and/or uridine. These are newly identified regulators of UPP1, adding to p53 regulation[37]. Exploration of these regulatory pathways in PDA and other cancers may hold translational promise.

Nutrients in the TME can be derived from serum or the various cell types that make up the bulk tumor. While discovery methods involving conditioned media and metabolomics are high-throughput, they tend not to capture the complex metabolic interactions of the TME. Biolog assays provide an unbiased approach to assess metabolic fuel utilization. We utilize this system to first obtain source-agnostic information about the nutrients utilized by PDA cells, before conducting a targeted analysis of potential sources providing exogenous uridine to tumors. We observed evidence of uridine enrichment in the TIF of murine pancreatic tumors, tumor consumption of plasma-derived uridine by *in vivo* isotope tracing, reduction of this same plasma uridine pool upon whole-body macrophage depletion, and *in vitro* micromolar release of uridine from naïve macrophages and TAMs. Together, this evidence illustrates the complexity of nutrient availability in the TME and suggests a model where cells inside and outside PDA tumors fuel cancer metabolism with uridine.

There is growing appreciation for the importance of nucleosides in cancer, including inosine, thymidine, and deoxycytidine[6,14,38,39]. Inosine is consumed in melanomas by both cancer and $CD8^+$ effector T cells[40]. The upregulation of nucleoside usage under nutrient deprivation[40–42], especially in immune and PDA cells, supports the idea that metabolic competition contributes to immunosuppression and tumor progression. Along these lines, we show that UPP1-KO in an orthotopic syngeneic model of PDA severely blunts tumor growth, thus the UPP1-uridine scavenging axis is important for PDA cells. RNA is another important source of uridine for glucose-starved cells[47] and may be relevant for PDA cells, which readily scavenge intracellular- (i.e., autophagy) and extracellular biomolecules to fuel metabolism[8]. There are also several healthy cell types that utilize uridine for various purposes[20,21,23,43], and this complexity is a provocative area for future study. Collectively, our data identify the uridine-UPP1 axis as a driver of compensatory metabolism and support that nucleoside metabolism is therapeutically tractable in solid tumors.

2.5 Methods

Cell Culture.

The panel of PDA cell lines, HPNE, A549, HT1080, HCT116, and U2OS, were purchased from the American Type Culture Collection (ATCC) or the German Collection of Microorganisms

(DSMZ). The hPSC cell line and the mouse cell lines KPC 7940b and MT3-2D were generously provided under MTA by Rosa Hwang (MD Anderson Cancer Center), Gregory Beatty (University of Pennsylvania), and David Tuveson (Cold Spring Harbor Labs), respectively. iKras cell lines A9993 and iKRAS 9805 were derived as previously described[44]. The confirmation of the identity of cell lines was established with STR profiling, and lines were routinely tested for mycoplasma using MycoAlert (Lonza, # LT07-318). For routine propagation, unless otherwise indicated, all cell lines were cultured in high-glucose Dulbecco's Modified Eagle Medium (DMEM, Gibco, # 11965092) supplemented with 10% fetal bovine serum (FBS, Corning, 35-010-CV) at 37°C and 5% CO_2. Phosphate buffered saline (PBS, Gibco, # 10010023) was used for cell washing steps unless otherwise indicated. For treatments, the following inhibitors were used: MYC: Fedratinib (MedChemExpress, # HY-10409) and 10058-F4 (Cayman Chemical, # 15929); MEK1: trametinib (Selleckchem, # S2673).

Biolog Metabolic Assay.

In the initial phenotypic screen, the 22 cell lines were grown in 96-well PM-M1 and PM-M2 plates (Biolog, # 13101 and 13102). The assay was set up such that one well was used per test metabolite substrate, accompanied by three replicates of positive (glucose) and negative (blank) controls wells. The relative metabolic activity (RMA) from substrate catabolism in the cells was measured using Biolog Redox Dye Mix MB. Briefly, the cell lines were counted, and their viability assessed using Trypan Blue Dye (Invitrogen, # T10282). The cells were then washed 2x with Biolog Inoculating fluid IF-M1 (Biolog, # 72301) to remove residual culture media. Then, a cell suspension containing 20,000 cells per 50 µL was prepared in Biolog IF-M1 containing 0.3 mM glutamine and 5% dialyzed FBS (dFBS) (Hyclone GE Life Sciences, # SH30079.01) and plated into PM-M1 and PM-M2 96-well plates at 50 µL per well. Plates were incubated for 24 hours at 37°C and 5% CO_2, after which 10 µL Biolog Redox Dye Mix MB (Biolog, # 74352) was added to each well. Plates were sealed to prevent the leakage of CO_2. The reduction of the dye over time was measured as absorbance (A590-A750) using the OmniLog PM-M instrument (Biolog, # 93171) for 74.5 hours at 15 minutes interval. To account for proliferation/cell number in the Biolog screening assay, CyQUANT was used for normalization.

The data were processed and normalized using *opm* package[45] version 1.3.77 in R statistical programming tool. After removing CFPAC1 (atypically high signal across the plate), the maximum metabolic activity per cell line was taken as its main readout for substrate avidity (**Fig. 2-5a**) and normalized by subtracting the mean negative control signal for a given cell line from all other values for that cell line. Heatmap visualization of the data was plotted using *heatmap2* and *ComplexHeatmap* packages in R.

Correlation of Biolog Metabolites to Gene Expression of Enzymes.

High-confidence metabolites (HCMs) from the Biolog screening assay were correlated (Spearman Correlation) to gene expression data for enzymes associated with metabolite usage. Genes with high correlation co-efficient to a given metabolite were chosen for further analysis.

NADH Assay.

Cells were seeded in 96-well plates at 10,000 cells per well directly into the indicated media conditions. Following the incubation period at 37°C and 5% CO_2 (i.e., 24, 48, or 72 hours), MTT (Thermo Scientific, # L1193903) was added directly to the wells containing media. Cells were incubated at 37°C and 5% CO_2 for 1 hour, after which the media and MTT reagent were carefully removed. Next, to each well, 50 µL of DMSO (Sigma-Aldrich, # D2650) was added followed by 5 minutes incubation at room temperature before measuring absorbance at 570 nm.

CyQUANT Proliferation Assay.

Cells were seeded at 20,000 cells per well for the screening study or 2,000 cells per well for proliferation assays in growth media in 96-well plates (Corning, # 3603). For proliferation assays, the culture media was removed the next day, followed by a gentle 1x wash with PBS. Treatment media was then applied, and the cells incubated at 37°C and 5% CO_2 until they reached ~70% confluence. Media was then carefully aspirated, and the plate with cells attached was moved to -80°C for at least 24 hours to ensure complete cell lysis. To prepare the lysis buffer and DNA dye, CyQUANT Cell Lysis Buffer and CyQUANT GR dye (Invitrogen, # C7026) were diluted in water at 1:20 and 1:400, respectively. The frozen cells were then thawed and 100 µL of the lysis buffer was added to each well. Thereafter the plate was covered to prevent light from inactivating the GR dye and was placed on an orbital shaker for 5 minutes before measurement. Fluorescence from each well, indicating GR dye binding to DNA, was then measured utilizing a SpectraMax M3 Microplate Reader with SoftMax Pro 5.4.2 software at an excitation wavelength of 480 nm and an emission wavelength of 520 nm.

ATP-based Viability Assay.

Cells were seeded in quadruplicate at a density of 2,500 – 5000 cells in 100 µL DMEM per well of the white walled 96-well plates (Corning/Costar, # 3917). Next day, the media was aspirated, each well was washed with 200 µL PBS after which treatment media was introduced. At the end of the experiment duration (48 or 72 hours), relative proliferation was determined with CellTiter-Glo 2.0 Cell Viability Assay Kit (Promega, # G9243) and the luminescence quantified using a SpectraMax M3 Microplate Reader.

Live Cell Proliferation Assay.

Cells were seeded in 96-well plates at 1,000 cells per well in 100 µL of growth media and incubated overnight at 37°C, 5% CO2. After 24 hours, media was changed, and the cells were incubated for a further 72 hours during which cell proliferation was determined by live cell imaging on a BioSpa Cytation.

UPP1 CRISPR/Cas9 knockout.

The expression vector pspCas9(BB)-2A-Puro (PX459) used to generate the UPP1 CRISPR/Cas9 constructs was obtained from Addgene (Plasmid # 48139). The plasmid was cut using the restriction enzyme *BbsI* followed by the insertion of human or mouse uridine phosphorylase 1 sgRNA sequences (**Supplementary Table 4**), as previously described[46]. The human and mouse sequences were obtained from the Genome-Scale CRISPR Knock-Out (GeCKO) library. For transfection, the human or mouse PDA cells were seeded at 1.5 x 10^5 cells per well in a 6-well plate one day prior. The cells were transfected with 1 µg of plasmid pSpCas9-UPP1 using Lipofectamine 3000 Reagent (Invitrogen, # L3000001) according to manufacturer's instruction. After 24 hours, the selection of successfully transfected cells was commenced by culturing the cells with 0.3 mg/mL puromycin in DMEM. The puromycin-containing media was replaced every two days until selection was complete, as indicated by the death and detachment of all non-transfected cells. Thereafter, the successfully transfected cell lines were expanded and clonally selected after serial dilution.

siRNA Experiments.

5 x 10^5 ASPC1 cells were seeded per 6-cm dish for 24 hours in the growth media. On Day 2 media was changed and the respective SMARTpool siRNA containing media was added. siRNA transfection was prepared with Lipofectamine RNAiMAX (ThermoFischer Scientific, # 13778075) according to the manufacturer's instructions. For the transfection, Opti-MEM^{TM} Reduced Serum Medium (# 31985-062) was used and siRNAs were added at a concentration of 20 nM. Cells were transfected for 48 hours after which the cells were trypsinized, counted, and plated for MTT assay. The remaining cells were pelleted, and RNA was extracted for qPCR. The siRNAs used were as follows: non-targeting control (Cat #D-001810-01-05), SMARTpool ON-TARGETplus Human PGM2 (55276) (# L-020785-01-0005), ON-TARGETplus Human UCK1 (83549) (# L-004062-00-0005), and ON-TARGETplus Human UCK2 (7371) (# L-005077-00-0005).

Quantitative Reverse-Transcriptase Polymerase Chain Reaction.

Cells were seeded at a density of 5-8 x 10^5 cells/well, allowed to attach overnight, and scraped were and pelleted 24 h after treatment (where applicable). RNA samples were isolated using the RNEasy Plus Mini Kit (QIAGEN, # 74134) according to the manufacturer's instructions. RNA purity was assessed using a NanoDrop One (ThermoFisher Scientific, ND-ONE-W). Thereafter, 1 µg of the RNA samples were reverse transcribed to cDNA using the iScript cDNA Synthesis Kit (Bio-Rad, 1708890) according to the accompanying instructions. qPCR was performed on the QuantStudio 3 Real-Time PCR System (ThermoFisher Scientific, # A28131) using Power SYBR Green PCR Master Mix (ThermoFisher Scientific, # 4367659). Alternatively, qPCR was run on an Applied Biosystems StepOne Plus instrument (software version 2.3) with Power SYBR Green Master Mix (Applied Biosystems, # 4367659) at 10 µL total volume [consisting of 5 µL SYBR, 2 µL nuclease free water, 2 µL of cDNA after diluting 1:4 in water, 0.5 µL of 10 µM forward (F) primer, and 0.5 µL 10 µM reverse (R) primer]. Primer sequences are listed in **Supplementary Table 5**. The gene expression was calculated as delta CT and *RPS21* or *ACTB* was used as a housekeeping gene.

Western Blotting.

Following culture, media was aspirated, and the wells washed 1x with PBS. Thereafter, 100 µL of radioimmunoprecipitation assay buffer (Sigma-Aldrich, # R0278) to which phosphatase and protease inhibitors was added, as transferred to each well to lyse the cells. Lysis and the collection of the lysates were completed on ice. Following a 5-10-minute incubation on ice, lysates were collected into 1.5 mL Eppendorf tubes and centrifuged at 4°C for 10 minutes at 18,000 g to extract the sample supernatant. Protein concentration of the samples for western blot analysis were measured using Pierce^{TM} BCA Protein Assay Kit (Thermo Fisher, # 23227) according to manufacturer's instructions. For the running step, samples were loaded at 20-25 µg protein per lane along with the SeeBlue Plus2 protein ladder (# Invitrogen) and run at 120 V on an Invitrogen NuPAGE 4-12% Bis-Tris gel (Thermo Fisher, # NP0336BOX). Thereafter, the separated proteins were transferred to methanol-activated PVDF membranes (Millipore) at 25 V for 60 minutes. Following this, membranes were immersed in blocking buffer [5% blotting-grade blocker (Bio-Rad, # 1706404) in TBS-T solution: tris-buffered saline (Bio-Rad, # 1706435) with

0.1% Tween® 20 (Sigma-Aldrich, # 9005-64-5)] for ~ 1 hour on a plate rocker at room temperature. Next, membranes were washed 3x with TBS-T at 10 minutes per wash, immersed in the indicated primary antibodies, and incubated overnight at 4°C on a plate rocker. The antibodies used were diluted in blocking buffer at dilutions recommended by the manufacturer. The following day, the primary antibody was removed, and the membrane was washed 3x with TBS-T and on a plate rocker for 5 minutes per wash. Immediately after, the membrane was incubated for 60 minutes and with gentle rocking at room temperature in the appropriate secondary antibody diluted 1:10,000 in TBS-T. Lastly, the membrane was washed 3x in TBS-T at 10 minutes per wash and incubated in chemiluminescence reagent (Clarity Max Western ECL Substrate, Cat. #1705062) according to the manufacturer's instructions. Subsequently, blot images were acquired on a Bio-Rad ChemiDoc Imaging System (Image Lab^{TM} Touch Software version 2.4.0.03). The following primary antibodies were used in this study and at 1:1000 dilution: anti-UPP1 (Sigma-Aldrich, # HPA055394), anti-c-MYC (Cell Signaling, # 5605S), anti-pERK (Cell Signaling, # 9106L), anti-ERK (Cell Signaling, # 9102S), anti-PGM2 (Invitrogen, # PA5-31378), and anti-Vinculin (Cell Signaling, # 13901S). The following secondary antibodies were used: anti-rabbit-HRP (Cell Signaling, # 7074S), and anti-mouse-HRP (Cell Signaling, # 7076P2). The uncropped, unprocessed images of the western blots are presented in Figures 2-5 – 2-13.

Murine Tumor Studies

Animal studies were performed at the University of Michigan (UM), the Institute of Cancer Research (ICR), and the University of Chicago (UChicago) according to approved protocols. Specifically, for studies at UM, the Institutional Animal Care and Use Committee (IACUC)

PRO00010606 was followed; ICR studies conformed to UK Home Office Regulations under the Animals Scientific Procedures Act 1986 and national guidelines (Project licence-P0A54750A protocol 5); UChicago IACUC Protocol #72587 was followed. Mice were housed in a pathogen-free animal facility at a maximum of five animals per cage with a 12-hour light/12-hour dark cycle, 30–70% humidity and 20–23°C temperatures maintained and were provided water and fed *ad libitum* with chow (5L0D – PicoLab Laboratory Rodent Diet).

Pancreatic Tumor Models.

For mouse studies at UM, male and female 6–8 weeks old C57BL/6J mice were obtained from The Jackson Laboratory (Strain # 000664) and maintained in the facilities of the Unit for Laboratory Animal Medicine (ULAM) under specific pathogen-free conditions. Prior to tumor cell injection, wild type or Upp1 knockout murine cell lines (either derived from MT3-2D or KPC 7940b) were harvested from culture plates according to standard cell culture procedures. The cells were counted, washed 1x with PBS and resuspended in 1:1 solution of serum free DMEM and Matrigel (Corning, # 354234). For orthotopic surgical procedure, mice were anaesthetized using inhalation anesthesia. The surgical site was sterilized by swapping with iodine (Povidine-Iodine Prep Pad, PDI, # B40600). This was followed by incision on the left flank using sterilized instruments. Thereafter, the cell lines were injected into the pancreas and the incision sutured. Cell injection was as follows: 50,000 or 100,000 cells in 50 μL final volume for orthotopic implantation or ~1 x 10^6 cells in 100 μL final volume for subcutaneous implantation. Animals were monitored regularly and all orthotopic experiments were concluded ~3-4 weeks after injection.

For the studies at ICR, female ~6 weeks old C57BL/6NCrl mice were purchased from Charles River Laboratories (Strain # 027). Prior to tumor cell injection, MT3-2D sgVector (sgV) and the Upp1 knockout cells (sg1 and sg3) were trypsinized according to standard cell culture protocol. Cells were washed with PBS and resuspended in 1:1 Hank's balanced salt solution (HBSS; Gibco, # 14025092) and Matrigel (Corning, # 354234). Following surgical incision, 50,000 cells in 20 μL final volume were injected into the pancreas. Tumor growth was monitored by palpating three times per week. Studies were terminated when the animals injected with the vector reached a high tumor burden based on palpation.

For the studies at UChicago, C57BL/6J mice 8-12 weeks of age were purchased from Jackson Laboratories (Strain # 000664). 2.5 x 10^5 cells per tumor were resuspended in 20 μL of 5.6 mg/mL Cultrex Reduced Growth Factor Basement Membrane Extract (RGF BME; R&D Biosystems, # 3433-010-01) and serum-free RPMI (SF-RPMI) solution. The BME:cellular mixture was injected into the splenic lobe of the pancreas of the mice, as previously described[47]. After implantation, end point was determined by abdominal palpation and daily monitoring of body weight.

Macrophage Depletion.

The KPC 7940b cell line was orthotopically implanted into ~8 weeks old male and female C57BL/6J mice, as above. Two weeks after injection, mice were randomized into two groups, namely, control and macrophage depletion (i.e., clodronate + anti-mouse CSF1 antibody). Thereafter, the control group mice were treated on Day 1 with 1 mg IgG (*InVivo*MAb rat IgG1 Isotype control, anti-trinitrophenol, # BE020, Bio X Cell, USA) and on Day 2 with 200 μL

Control Liposome (PBS) (# CP-005-005, Liposoma BV, The Netherlands). The macrophage depletion mice were treated on Day 1 with *InVivo*MAb anti-mouse CSF1 (anti-CSF1, # BE0204, Bio X Cell) and Day 2 with 200 μL Clodronate Liposomes (# CP-005-005, Liposoma BV). Two subsequent treatment sequences were administered at two-day intervals as follows: 0.5 mg IgG or anti-CSF1 followed next day by 200 μL Control Liposome or Clodronate Liposomes for the control and depletion groups, respectively. The experiment was terminated after 1 week. From each mouse, blood samples were collected into EDTA BD Vacutainer K2 EDTA 3.6mg (# 36784) and centrifuged at 200 *g* for 5 minutes for plasma collection. In addition, tumors were harvested, weighed, and used for the extraction of TIF, as below.

Tumor Interstitial Fluid Collection.

Tumor interstitial fluid (TIF) was isolated from tumors, as described before[30]. Briefly, tumors were rapidly dissected after euthanizing animals. Tumors were weighed and rinsed in blood bank saline solution (150 mM NaCl) and blotted on filter paper (VWR, # 28298–020) until dry. Tumor isolation occurred in less than 3 minutes to minimize the time the tumor is ischemic prior to TIF isolation. Tumors were cut in half and put onto 20 μm nylon mesh filters (Spectrum Labs, # 148134) on top of 50 mL conical tubes, and centrifuged for 10 minutes at 4°C at 400 *g*. TIF was then processed for metabolomics in a similar manner as plasma, as described below.

In vivo Delivery of Isotopically Labeled Uridine.

Uridine-derived ribose carbon was traced *in vivo* using $^{13}C_5$ (ribose) labeled uridine (Cambridge Isotope Laboratories, # CLM-3680-PK). Specifically, mice bearing orthotopic or subcutaneous tumors were generated, as described above, using KPC 7940b cell lines. For the orthotopic tumors, after the tumors became palpable, mice were either injected intraperitoneally with 200 μL PBS (control group) or same volume of 0.2 M $^{13}C_5$-uridine. For the subcutaneous models, 50 μL PBS or 0.2 M $^{13}C_5$-uridine were injected directly into the tumors. Tumors were harvested 1 hour after injection and processed for isotope tracing, as detailed below.

Mass Spectrometry-Based Metabolomics

Metabolomics Sample Preparation. For *in vitro* extracellular (media) and intracellular metabolomic profiling, PDA cells were seeded in triplicates in a 6-well plate at 4-6 x 10^6 cells per well in growth media. A parallel plate for protein estimation and sample normalization was also set up. After overnight incubation, the culture media was aspirated and replaced with media containing treatments or supplemented metabolites of interest. The cells were then cultured for a further 24 hours. Thereafter, for extracellular metabolites, 200 μL of media was collected from each well into a 1.5 mL Eppendorf tube and to that 800 μL ice-cold methanol was added. For intracellular metabolites, the remaining media was aspirated, and samples washed 1x with 1mL PBS before incubation with 1 mL ice cold 80% methanol on dry ice for 10 minutes. Thereafter, cell lysates were collected from each well and transferred into separate 1.5 mL Eppendorf tubes. The samples were then centrifuged at 12,000 *g*. For each experimental condition, the volume of supernatant to collect for drying with SpeedVac Vacuum Concentrator (model: SPD1030) was determined based on the protein concentration of the parallel plate.

For tumors, the samples were flash frozen in liquid nitrogen upon collection. Tumors of approximately equal weight (<100 mg) were collected per sample per experimental group. The tumors were then put into 2 mL Eppendorf tubes to which 1mL of ice-cold 80% methanol (diluted in 20% H_2O). Metallic beads were added to each tube and samples were shaken and homogenized on an Retsch TissueLyser II (# 129251128) in intervals of 30 seconds until fully homogenized. Samples were then centrifuged at 12,000 g and supernatant collected for further processing.

Targeted Metabolomics.

The collected supernatants were dried using SpeedVac Vacuum Concentrator, reconstituted with 50% v/v methanol in water, and analyzed by liquid chromatography-coupled mass spectrometry (LC-MS), as described in detail previously[48]. Data was analyzed with Agilent Masshunter Workstation Quantitative Analysis for QQQ version 10.1, build 10.1.733.0.

Stable Isotope Tracing.

For stable isotope tracing in cells, $^{13}C_5$ uridine (ribose labeled), hereafter called labeled- or ^{13}C-uridine (Cambridge Isotope Laboratories, # CLM-3680-PK) was supplemented at 0.1 mM or 1mM for in vitro assays. Briefly, wild type or UPP1 knockout cells were cultured overnight in regular media. Next day, cells were washed 1x followed by the introduction of media containing the indicated amounts of glucose, dialyzed FBS and supplemented with labelled uridine. In parallel, a similar experiment was set up for unlabeled uridine. The cell lines were then cultured in the uridine-supplemented media for 24 hours or as otherwise indicated, followed by sample collection, as detailed for unlabeled intracellular metabolomics above. Labeled tumors were similarly collected as detailed above. Samples for TOF MS, as described in detail previously[48], and analyzed with Agilent MassHunter Workstation Profinder Version 10.0, Build 10.0.10062.0.

For the experiments were glucose and uridine concentrations were varied (i.e., 5/0.1 mM and 1/0.1 mM, respectively) followed by stable isotope tracing, the cells were seeded at a density of 5 x 10^5 and treated with $^{13}C_5$-uridine or unlabeled uridine in DMEM supplemented with dialyzed FBS and the indicated concentration of glucose for 24 hours. Then cells were washed with 1 mL cold PBS followed by the addition of 1 mL -20°C 2:2:1 methanol:acetonitrile:water to the wells on dry ice for 10 min. Cells were scraped from the dish. Next, samples were subjected to 3 cycles of 30 second vortex, 1 minute liquid N_2, and 10 minutes 25°C bath sonicate. Samples were then stored at -20°C overnight and centrifuged at 14,000 RCF at 4°C for 10 minutes. 860 µL supernatant was transferred to a new tube and dried by SpeedVac Vacuum Concentrator. Protein pellets were also dried similarly to remove excess supernatant, resuspended in 400 µL 100 mM NaOH through repeated vortexing, 5 minutes incubation at 95°C, and protein quantified by BCA assay (ThermoFisher, # 23227). Dried supernatant pellets were resuspended in 2:1 Acetonitrile:Water at 1 µL per 2.5 µg protein and subjected to 2 cycles of: 5 minutes 25°C bath sonicate, 1 minute vortex. Samples were incubated at 4°C overnight, then centrifuged at 14,000 RCF at 4°C for 10 min and the supernatant transferred to LC vials and stored at -80°C until analysis. For sample analysis, 4 µL of metabolite extracts were run on an Agilent 6545 Q-TOF Mass Spectrometer and an Agilent 1290 Infinity II LC system using a iHILIC-(P) Classic 2.1 mm x 100 mm, 5 µm column (HILICON, 160.102.0520) with iHILIC-(P) Classic Guard column (HILICON, 160.122.0520) attached. A column temperature of 45°C and a flow rate of 250 µL/min was used. Mobile phases were A: 95% water, 5% acetonitrile, 20 mM ammonium bicarbonate, 0.1% ammonium hydroxide solution (25% in water), 2.5 µM medronic acid and B: 85% acetonitrile, 5% water, 2.5 µM medronic acid. Each sample was subjected to a linear gradient: 0-1 minute 90% B, 1-12 minutes 35% B, 12-12.5 minutes 25% B, 12.5-14.5 minutes

25% B, 14.5-15 minutes 90% B, which was then followed by 4 min at 400 µL/minute and 2 minute at 250 µL/min at 90% B for re-equilibration. Chromatograms for selected metabolites were extracted in Skyline Daily (software version 22.2.1.256) and manually integrated according to an in-house list of standard m/z and retention times. Natural isotope abundance correction was performed, and peak areas plotted.

Quantification of TIF Metabolite Levels.

For quantification of uridine and glucose in TIF, quantitative metabolite profiling of fluid samples was performed, as previously described[30]. Briefly, chemical standards were prepared and serially diluted in high-performance liquid chromatography grade water in a dilution series from 5 mM to 1 µM. Using the external standard library dilutions, we created a standard curve based on the linear relationship of the normalized peak area and the concentration of the metabolite. This standard curve was then used to interpolate the concentration of the metabolite in the TIF sample.

Clinical Samples.

Patients with pancreas resections for PDA from 2021 to 2022 at the University of Michigan Health System were included in the study. All hematoxylin and eosin (H&E) stained slides were reviewed, and diagnoses confirmed, and corresponding areas were carefully selected and marked. The collection of patient-derived tissues for histological analyses was approved by the Institutional Review Board at the University of Michigan (IRB number: HUM00098128). Tissues were fixed in 10% neutral buffered formalin and paraffin embedded using standard protocols before sectioning and staining.

Tissue microarrays (TMAs).

All specimens are from patients with pancreas resections for pancreatitis, cystic neoplasms, or PDA from 2002 to 2015 at the University of Michigan Health System. After fixation in 10% neutral buffered formalin (hours to a couple of days depending on the size of the tissue), samples were embedded in paraffin. All tissues were H&E stained, reviewed, and diagnoses confirmed. Corresponding areas were carefully selected and marked. Duplicate 1 mm diameter tissue cores from a total of 213 patient tissue samples were selectively punched and transferred to recipient tissue array blocks. Five TMAs were set up and H&E and immunohistochemistry staining was performed on each TMA block using standard protocols. The TMA was previously published[49].

RNAscope. RNAscope was performed as previously described[50], and according to the manufacturer's protocol (ACD: 323100-USM). Briefly, paraffin wax was removed with xylene and slides were rehydrated. Samples underwent antigen retrieval for 15 minutes. Samples were blocked for 30 minutes at room temperature with CoDetection Antibody Diluent and then incubated overnight at 4°C with a primary antibody for panCK (Mouse anti-cytokeratin, pan reactive; 1:100; BioLegend; # 628602) diluted in CoDetection Antibody Diluent. Protease digestion was performed for 13 minutes at room temperature. Human *UPP1* RNAscope probe (ACD; # 509279; Lot: 21272A) was added to slides for 2 hours at 40°C. Samples were incubated with TSA-Cy3 fluorophore (1:2,000; Akoya Biosciences; # NEL704A001KT) diluted in CoDetection Antibody Diluent. Following HRP blocking, slides were rinsed in PBS + 0.1% Tween-20 (PBST). Slides were stained with DAPI (1:30,000; Millipore Sigma; # 10236276001) diluted in PBS for 15 minutes at room temperature. After rinsing in PBST, slides were incubated for 45 minutes at room temperature with secondary antibodies diluted 1:500 in CoDetection Antibody Diluent. Slides were rinsed with PBST and mounted in ProLong Gold Antifade Mountant (Invitrogen, # P36930). Sections were visualized on a Leica SP5X upright confocal. For quantitation, 20x fields of view were imaged and analyzed using FIJI/Image J (version 1.53c). For analysis, images were converted to 16-bit, the threshold was adjusted, and the area of *UPP1* expression was measured per 20x image.

Immunohistochemistry.

Patients tissue slides were deparaffinized and rehydrated with graded Histo-Clear (National Diagnostics), ethanol, and water. Slides were quenched for 15 minutes in a methanol solution containing 1.5% hydrogen peroxide before antigen retrieval. Samples underwent antigen retrieval with sodium citrate buffer (2.94 g/L sodium citrate, 0.05% Tween 20, pH 6). Samples were blocked using blocking buffer (5% bovine serum albumin, 0.2% Triton-X 100, in PBS) for 1 hour at room temperature. After blocking, slides were incubated overnight at 4°C with primary antibody (Rabbit anti-UPP1; 1:200; Sigma-Aldrich, # HPA055394) diluted in blocking buffer. Slides were rinsed in PBS and incubated for 1 hour at room temperature with a biotinylated secondary antibody (Horse anti-Rabbit; 1:500; Vector Labs, # BA-1100). After rinsing, slides were prepared for a color reaction by incubating with Vectastain Elite ABC Reagent (Vectastain Elite ABC-HRP Kit; Vector Labs, # PK-6100) for 30 minutes at room temperature. Sections were developed with DAB (DAB Substrate Kit; Vector Labs, # SK-4100) for 2 minutes, rinsed, and counterstained with hematoxylin. Slides were mounted in Permount Mounting Medium (Fisher). After drying, slides were imaged using an Olympus BX53F microscope, Olympus CP80 digital camera, and CellSens standard software.

Mouse tumors were fixed in 10% neutral buffered formalin for 48 hours and embedded in paraffin as formalin-fixed paraffin-embedded (FFPE) blocks. Serial sections of 4 µm thickness were cut from FFPE blocks, deparaffinized in xylene, processed in graded alcohol, and rehydrated in water. One section was stained with H&E for histological analysis. The Dako Autostainer Link 48 automated immunostaining platform was used for all the below immunostainings. Anti-Cd31 monoclonal antibody (SZ31, # DIA-310, Dianova) was used at a 1:75 dilution, followed by heat-induced epitope retrieval for 20 mins at 97°C using a PT Link module (Agilent). Anti-Cd8 monoclonal antibody (clone - 4SM15, # 14-0808, eBioscience) was used at a 1:200 dilution, and anti-F4/80 monoclonal antibody (Clone-A3-1, # MCA497G, Bio-Rad) was used at a 1:100 dilution. For these antibodies, EnVision FLEX Target Retrieval Solution (high pH; # K800421-2, Agilent) and Nichirei anti-rat Histofine polymer reagent (# 41491F, Nichirei Biosciences Inc) primary antibody detection kits were used. For Cd3, polyclonal antibody (# ab5690, Abcam) was used at a 1:400 dilution with EnVision FLEX Target Retrieval Solution (low pH of 6) for 20mins in PT link module and detected with Vector Rabbit ImmPRESS HRP Horse anti-rabbit IgG polymer kit (Vector Laboratories, # MP-7401-50). Appropriate positive and negative controls were used in all runs. The Nanozoomer-XR C12000 (Hamamatsu) was used to scan whole stained sections. Antigen expression was scored using Definiens Test Studio Software (Definiens). F4/80 was quantified using Image J.

Immunohistochemistry of UPP1 expression in human normal and PDA tissues was also accessed from the Human Protein Atlas portal[51].

PDA Dataset Analysis.

The human PDA microarray datasets with accession numbers GSE71729 (n=46 normal pancreas vs 145 tumor tissues) and GSE62452 (n=61 non-tumoral vs 69 tumor tissues) were obtained from NCBI GEO[52]. Differential gene expression between PDA and non-tumors were performed in R using *limma* package (version 3.38.3). Kaplan Meier (KM) overall survival (log-rank test) was performed after splitting the tumor samples per dataset into UPP1 high and low subsets. For KM, human PDA tumor datasets and the accompanying clinical data from the following sources were used: GSE71729 (n=145), The Cancer Genome Atlas (TCGA) data (n=146), International Cancer Genome Consortium (ICGC, n=267), and Puleo et al. (n=288)[53]. The iKras mice data was obtained from NCBI GEO under the accession number GSE32277. TCGA expression data of tumors with KRAS wild type (n=43) and KRAS G12D mutation (n=42) were used to determine the relative expression of UPP1 in KRAS G12D mutated tumors.

Pan-cancer Dataset Analysis.

TCGA pan-cancer datasets, including bladder-, colon-, esophageal-, lung-, head and neck-, prostate cancer, and glioblastoma, were downloaded from Xena Platform from University of California Santa Cruz[54]. An additional colorectal (GSE44076) was also used. For the comparisons, the normal or adjacent matched/unmatched normal samples were used. In total, 2,828 cancer tissue samples and 379 non-tumoral control tissue samples were analyzed. These datasets were used to compare *UPP1* expression between cancer and non-cancer tissues.

CCLE Gene Analysis and PDA Tumor Data Stratification.

Gene expression data for uridine high and uridine low metabolizers were extracted from the cancer cell line encyclopedia (CCLE, GSE36133). The subsets were then compared using *limma* package in R to determine the differentially expressed genes in uridine-high metabolizers/consumers relative to the lower metabolizers/consumers. For the tumor stratification, samples in the dataset GSE71729 (n=145) were ranked into UPP1-high and low groups and compared as above to determine the genes differentially expressed in UPP1 high tumors. UPP1 protein expression was performed in *KRAS* mutant and wildtype cell lines using data from DepMap[55].

Pathway Analyses.

Pathway analyses were performed using DAVID functional annotation platform (https://david.ncifcrf.gov/, version 6.8) or the gene set enrichment analysis (GSEA, version 4.0.3) with GSEAPreranked option. Ranking of genes was based on the product of the logFC and -log(p-value). GSEA was run with default parameters, except gene set size filter set at min=10. Gene ontology analyses were performed with DAVID.

Promoter Analysis of UPP1.

CiiDER[56] was used for predicting UPP1 gene transcription factor sites. DNA sequence flanking UPP1 transcription start site (1500 bases upstream, 500 bases downstream) was used to compare to JASPAR2020_CORE_vertibrates Position Frequency Matrix (PFM) model to generate a score of similarity. As transcription factor binding sites are variable and binding sites rarely match the model perfectly, a default deficit score of 0.15 was used, where deficit score of 0 represents prefect match. Top 10 transcription factors were obtained using the predicted UPP1 binding sites with respect to sequences from the human genome (GRCh38.94) and mouse genome (GRCm38.94).

Statistical Analysis.

Statistics were performed either with GraphPad Prism 8 (GraphPad Software Inc.) or using R version 3.5.2. Data from experimental groups were compared using the two-tailed t-test or analysis of variance (ANOVA) with post hoc corrections where applicable, and between biological (or in vitro) replicates. The error bars in all graphs represent the mean ± standard deviation (s.d). Statistical significance was accepted if $P < 0.05$. For data analysis and visualization in R, packages (with versions) used include *dplyr* (0.8.3), *ggplot2* (3.3.5), *gplots* (3.0.1, heatmap.2 function), *ComplexHeatmap* (2.3.5), *tidyverse* (1.3.0) and *VennDiagram* (1.6.20).

2.6 References

1. Singhi, A. D., Koay, E. J., Chari, S. T. & Maitra, A. Early Detection of Pancreatic Cancer: Opportunities and Challenges. *Gastroenterology* **156**, 2024–2040 (2019).
2. Wood, L. D., Canto, M. I., Jaffee, E. M. & Simeone, D. M. Pancreatic Cancer: Pathogenesis, Screening, Diagnosis, and Treatment. *Gastroenterology* **163**, 386-402.e1 (2022).
3. Ho, W. J., Jaffee, E. M. & Zheng, L. The tumour microenvironment in pancreatic cancer — clinical challenges and opportunities. *Nat. Rev. Clin. Oncol.* **17**, 527–540 (2020).
4. DuFort, C. C., DelGiorno, K. E. & Hingorani, S. R. Mounting Pressure in the Microenvironment: Fluids, Solids, and Cells in Pancreatic Ductal Adenocarcinoma. *Gastroenterology* **150**, 1545-1557.e2 (2016).
5. Encarnación-Rosado, J. & Kimmelman, A. C. Harnessing metabolic dependencies in pancreatic cancers. *Nat. Rev. Gastroenterol. Hepatol.* **18**, 482–492 (2021).
6. Halbrook, C. J. & Lyssiotis, C. A. Employing Metabolism to Improve the Diagnosis and Treatment of Pancreatic Cancer. *Cancer Cell* **31**, 5–19 (2017).

7. Helms, E., Onate, M. K. & Sherman, M. H. Fibroblast Heterogeneity in the Pancreatic Tumor Microenvironment. *Cancer Discov.* **10**, 648–656 (2020).

8. Koong, A. C. *et al.* Pancreatic tumors show high levels of hypoxia. *Int. J. Radiat. Oncol.* **48**, 919–922 (2000).

9. Beatty, G. L., Werba, G., Lyssiotis, C. A. & Simeone, D. M. The biological underpinnings of therapeutic resistance in pancreatic cancer. *Genes Dev.* (2021) doi:10.1101/gad.348523.121.

10. Kamphorst, J. J. *et al.* Human Pancreatic Cancer Tumors Are Nutrient Poor and Tumor Cells Actively Scavenge Extracellular Protein. *Cancer Res.* **75**, 544–553 (2015).

11. Commisso, C. *et al.* Macropinocytosis of protein is an amino acid supply route in Ras-transformed cells. *Nature* **497**, 633–637 (2013).

12. Yang, S. *et al.* Pancreatic cancers require autophagy for tumor growth. *Genes Dev.* **25**, 717–729 (2011).

13. Zhao, H. *et al.* Tumor microenvironment derived exosomes pleiotropically modulate cancer cell metabolism. *eLife* **5**, e10250 (2016).

14. Halbrook, C. J. *et al.* Macrophage-Released Pyrimidines Inhibit Gemcitabine Therapy in Pancreatic Cancer. *Cell Metab.* **29**, 1390-1399.e6 (2019).

15. Sousa, C. M. *et al.* Pancreatic stellate cells support tumour metabolism through autophagic alanine secretion. *Nature* **536**, 479–483 (2016).

16. Kim, P. K. *et al.* Hyaluronic acid fuels pancreatic cancer cell growth. *eLife* **10**, e62645 (2021).

17. Klijn, C. *et al.* A comprehensive transcriptional portrait of human cancer cell lines. *Nat. Biotechnol.* **33**, 306–312 (2015).

18. Possemato, R. *et al.* Functional genomics reveal that the serine synthesis pathway is essential in breast cancer. *Nature* **476**, 346–350 (2011).

19. Barretina, J. *et al.* The Cancer Cell Line Encyclopedia enables predictive modelling of anticancer drug sensitivity. *Nature* **483**, 603–607 (2012).

20. Choi, J. W. *et al.* Uridine protects cortical neurons from glucose deprivation-induced death: possible role of uridine phosphorylase. *J. Neurotrauma* **25**, 695–707 (2008).

21. Choi, J. W. *et al.* Uridine prevents the glucose deprivation-induced death of immunostimulated astrocytes via the action of uridine phosphorylase. *Neurosci. Res.* **56**, 111–118 (2006).

22. Wice, B. M., Reitzer, L. J. & Kennell, D. The continuous growth of vertebrate cells in the absence of sugar. *J. Biol. Chem.* **256**, 7812–7819 (1981).

23. Geiger, A. & Yamasaki, S. Cytidine and Uridine Requirement of the Brain*†. *J. Neurochem.* **1**, 93–100 (1956).

24. Löffler, M., Wenzel, A. & Schneider, F. Cytokinetic studies on the switch from glucose to uridine metabolism, and vice versa, of Ehrlich ascites tumour cells in vitro. *Cell Prolif.* **20**, 181–190 (1987).

25. Linker, W., Löffler, M. & Schneider, F. Uridine, but not cytidine can sustain growth of Ehrlich ascites tumor cells in glucose-deprived medium with altered proliferation kinetics. *Eur. J. Cell Biol.* **36**, 176–181 (1985).

26. King, M. P. & Attardi, G. Human cells lacking mtDNA: repopulation with exogenous mitochondria by complementation. *Science* **246**, 500–503 (1989).

27. Son, J. *et al.* Glutamine supports pancreatic cancer growth through a KRAS-regulated metabolic pathway. *Nature* **496**, 101–105 (2013).

28. Lee, H.-J., Kremer, D. M., Sajjakulnukit, P., Zhang, L. & Lyssiotis, C. A. A large-scale analysis of targeted metabolomics data from heterogeneous biological samples provides insights into metabolite dynamics. *Metabolomics Off. J. Metabolomic Soc.* **15**, 103 (2019).

29. Yuan, M. *et al.* Ex vivo and in vivo stable isotope labelling of central carbon metabolism and related pathways with analysis by LC–MS/MS. *Nat. Protoc.* **14**, 313–330 (2019).

30. Sullivan, M. R. *et al.* Quantification of microenvironmental metabolites in murine cancers reveals determinants of tumor nutrient availability. *eLife* **8**, e44235 (2019).

31. Hezel, A. F., Kimmelman, A. C., Stanger, B. Z., Bardeesy, N. & DePinho, R. A. Genetics and biology of pancreatic ductal adenocarcinoma. *Genes Dev.* **20**, 1218–1249 (2006).

32. Kerk, S. A., Papagiannakopoulos, T., Shah, Y. M. & Lyssiotis, C. A. Metabolic networks in mutant KRAS-driven tumours: tissue specificities and the microenvironment. *Nat. Rev. Cancer* **21**, 510–525 (2021).

33. Collins, M. A. *et al.* Oncogenic Kras is required for both the initiation and maintenance of pancreatic cancer in mice. *J. Clin. Invest.* **122**, 639–653 (2012).

34. Ying, H. *et al.* Oncogenic Kras maintains pancreatic tumors through regulation of anabolic glucose metabolism. *Cell* **149**, 656–670 (2012).

35. Candido, J. B. *et al.* CSF1R+ Macrophages Sustain Pancreatic Tumor Growth through T Cell Suppression and Maintenance of Key Gene Programs that Define the Squamous Subtype. *Cell Rep.* **23**, 1448–1460 (2018).

36. Zhang, Y. *et al.* Myeloid cells are required for PD-1/PD-L1 checkpoint activation and the establishment of an immunosuppressive environment in pancreatic cancer. *Gut* **66**, 124–136 (2017).

37. Zhang, D., Cao, D., Russell, R. & Pizzorno, G. p53-dependent Suppression of Uridine Phosphorylase Gene Expression through Direct Promoter Interaction. *Cancer Res.* **61**, 6899–6905 (2001).

38. Dalin, S. *et al.* Deoxycytidine Release from Pancreatic Stellate Cells Promotes Gemcitabine Resistance. *Cancer Res.* **79**, 5723–5733 (2019).

39. Tabata, S. *et al.* Thymidine Catabolism as a Metabolic Strategy for Cancer Survival. *Cell Rep.* **19**, 1313–1321 (2017).

40. Wang, T. *et al.* Inosine is an alternative carbon source for CD8 + -T-cell function under glucose restriction. *Nat. Metab.* 1–13 (2020) doi:10.1038/s42255-020-0219-4.

41. Jurkowitz, M. S., Litsky, M. L., Browning, M. J. & Hohl, C. M. Adenosine, inosine, and guanosine protect glial cells during glucose deprivation and mitochondrial inhibition: Correlation between protection and ATP preservation. *J. Neurochem.* **71**, 535–548 (1998).

42. Litsky, M. L., Hohl, C. M., Lucas, J. H. & Jurkowitz, M. S. Inosine and guanosine preserve neuronal and glial cell viability in mouse spinal cord cultures during chemical hypoxia. *Brain Res.* **821**, 426–432 (1999).

43. Skinner. O.S. *et al.* Salvage of Ribose from Uridine or RNA Supports Glycolysis when Glucose is Limiting. *Nat. Metab.* In press (2023) doi:10.1038/s42255-023-00774-2.

44. Collins, M. A. *et al.* Oncogenic Kras is required for both the initiation and maintenance of pancreatic cancer in mice. *J. Clin. Invest.* **122**, 639–653 (2012).

45. Vaas, L. A. I. *et al.* opm: an R package for analysing OmniLog(R) phenotype microarray data. *Bioinforma. Oxf. Engl.* **29**, 1823–1824 (2013).

46. Ran, F. A. *et al.* Genome engineering using the CRISPR-Cas9 system. *Nat. Protoc.* **8**, 2281–2308 (2013).

47. Erstad, D. J. *et al.* Orthotopic and heterotopic murine models of pancreatic cancer and their different responses to FOLFIRINOX chemotherapy. *Dis. Model. Mech.* **11**, dmm034793 (2018).

48. Kerk, S. A. *et al.* Metabolic requirement for GOT2 in pancreatic cancer depends on environmental context. *eLife* **11**, e73245 (2022).

49. Yi, Z. *et al.* KDM6A Regulates Cell Plasticity and Pancreatic Cancer Progression by Noncanonical Activin Pathway. *Cell. Mol. Gastroenterol. Hepatol.* **13**, 643–667 (2022).

50. Scales, M. K. *et al.* Combinatorial Gli activity directs immune infiltration and tumor growth in pancreatic cancer. *PLOS Genet.* **18**, e1010315 (2022).

51. Uhlén, M. *et al.* Tissue-based map of the human proteome. *Science* **347**, 1260419 (2015).

52. Barrett, T. *et al.* NCBI GEO: archive for functional genomics data sets—update. *Nucleic Acids Res.* **41**, D991–D995 (2013).

53. Puleo, F. *et al.* Stratification of Pancreatic Ductal Adenocarcinomas Based on Tumor and Microenvironment Features. *Gastroenterology* **155**, 1999-2013.e3 (2018).

54. Goldman, M. J. *et al.* Visualizing and interpreting cancer genomics data via the Xena platform. *Nat. Biotechnol.* **38**, 675–678 (2020).

55. Tsherniak, A. *et al.* Defining a Cancer Dependency Map. *Cell* **170**, 564-576.e16 (2017).

56. Gearing, L. J. *et al.* CiiiDER: A tool for predicting and analysing transcription factor binding sites. *PLOS ONE* **14**, e0215495 (2019).

57. Steele, N. G. *et al.* Multimodal Mapping of the Tumor and Peripheral Blood Immune Landscape in Human Pancreatic Cancer. *Nat. Cancer* **1**, 1097–1112 (2020).

2.7 Figures

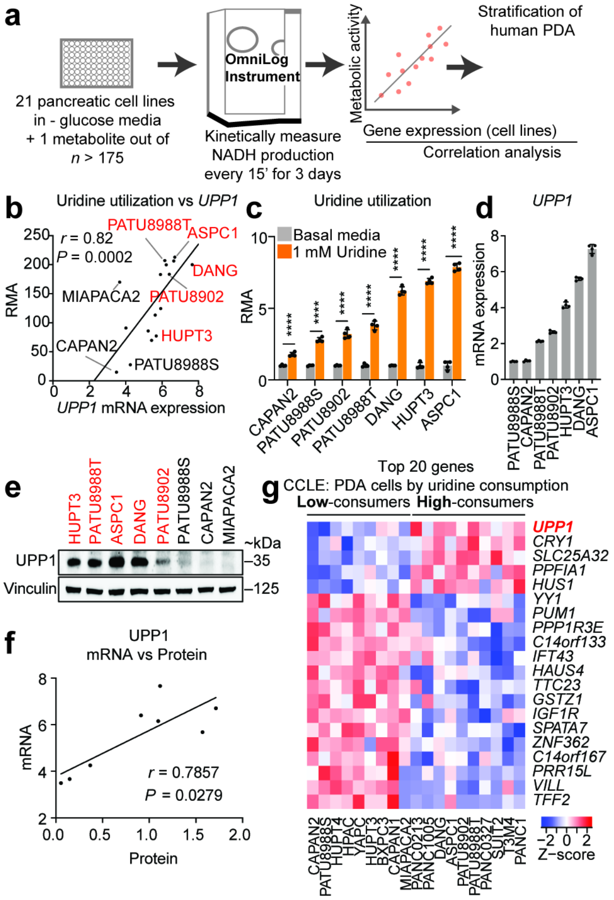

Figure 2-1 Profiling of metabolite utilization in PDA cells identifies uridine

a. Scheme of the nutrient metabolism screening assay and the correlation with gene expression in PDA cell lines and tumors.

b. Spearman correlation, r, between the normalized relative metabolic activity (RMA) for uridine catabolism in the screening data and UPP1 mRNA expression from CCLE in 16 PDA cell lines. The highlighted cell lines were used for further analyses. In red are UPP1-high cell lines.

c. RMA in a subset of PDA cell lines following supplementation with 1 mM uridine for 3 days.

d. qPCR validation of UPP1 mRNA expression in a subset of PDA cell lines.

e. Immunoblot showing basal UPP1 expression in PDA cell lines. Blots are representative of

three technical replicates with similar results. kDa, molecular weight unit.

f. Spearman correlation, r, between protein densitometry analysis of blot shown in Fig. 1e and mRNA expression of UPP1 in 8 corresponding PDA cells shown in Fig. 1b.

g. Topmost 20 genes differentially expressed by the PDA cell lines (in the CCLE) that were identified as uridine high consumers compared to low consumers from the nutrient metabolism screen. CCLE, cancer cell line encyclopedia. Data (c, d) are shown as mean ± s.d.

See “Statistics and reproducibility” (Methods) for additional information.

Statistics and Reproducibility

a. The use of >175 metabolites by 19 PDA cell lines and 2 non-PDA pancreatic cell lines was measured every 15 minutes for ~ 3 days (74.5 h) using the Biolog OmniLog device. The assay readout, relative metabolic activity (RMA), was correlated with the expression level of metabolic genes in cell lines; human PDA data were used for subsequent analyses. Nutrient-deficient media = no glucose, 0.3 mM glutamine and 5% dialyzed fetal bovine serum (dFBS).

c. n = 4 biologically independent samples per group. Statistical significance was measured by multiple unpaired two-tailed t-tests (two-stage step-up method) comparing RMA from cells in basal media vs 1mM uridine media, $****P < 0.0001$. The experiments were performed twice with similar results.

d. n = 4 biologically independent samples per cell line. The experiment was performed once.

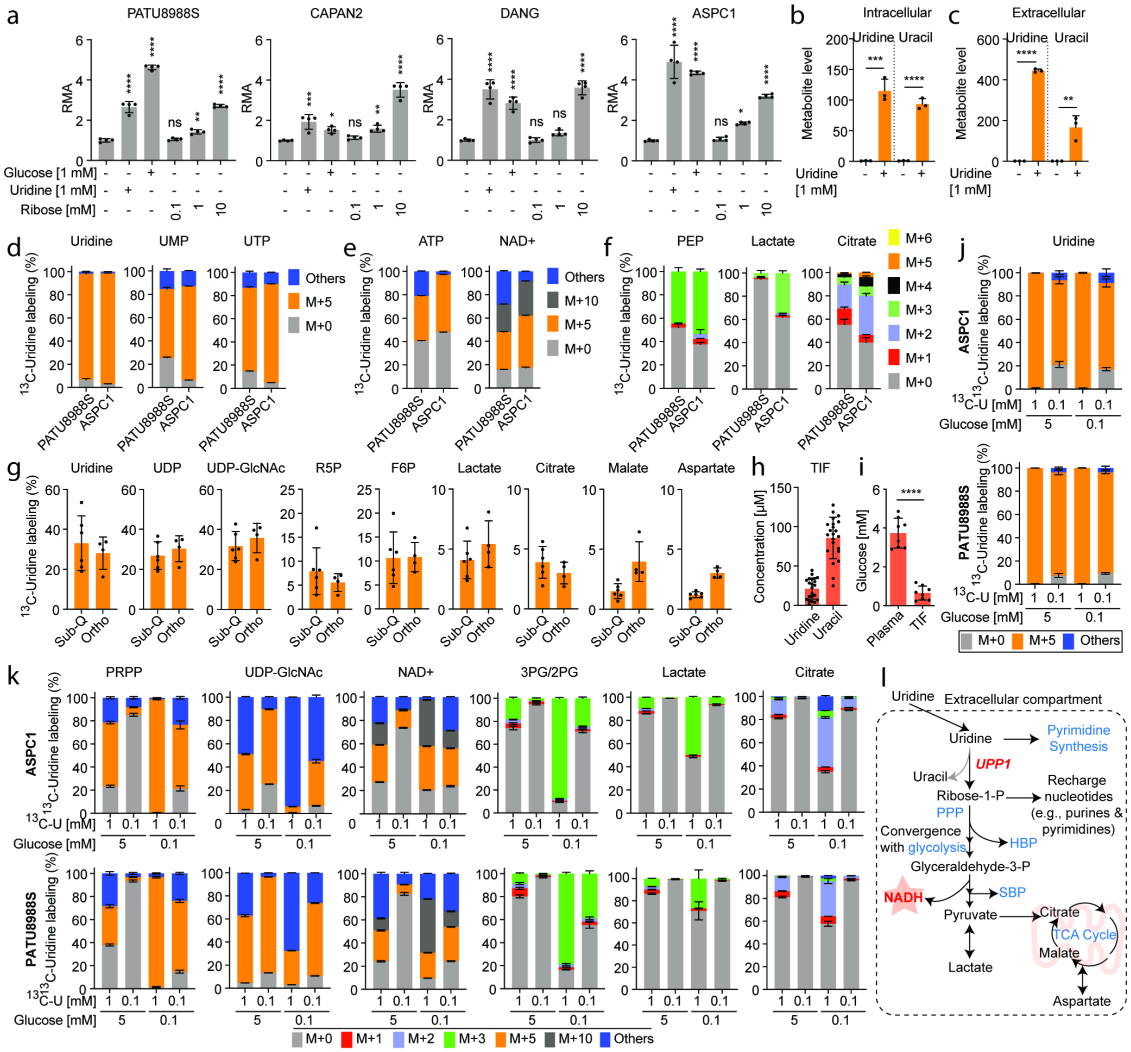

Figure 2-2 Uridine-derived ribose supports nutrient-restricted PDA

a. RMA of four PDA cell lines supplemented with glucose, uridine or ribose under nutrient-limited culture conditions (i.e., no glucose and glutamine, 5% dFBS).

b-c. Intracellular and extracellular uridine and uracil after 24 h culture of PATU8988S cells in media with no glucose and 10% dialyzed FBS with or without 1 mM uridine as measured by LC-MS.

d-f. Mass isotopologue distribution of $^{13}C_5$-uridine ribose-derived carbon in the indicated metabolites and cell lines after 24 h culture with 1mM uridine.

g. Isotope tracing showing $^{13}C_5$-uridine ribose-derived carbon labeling in subcutaneous (Sub-Q) or orthotopically (Ortho) implanted KPC 7940b tumors collected 1 h after injecting the mice with 0.2 M $^{13}C_5$-uridine.

h. Absolute quantitation via metabolomics of uridine and uracil concentration in the pancreatic tumor interstitial fluid (TIF) of mice orthotopically implanted with KPC 7490b syngeneic tumors.

i. Absolute quantitation via metabolomics of glucose concentration in the pancreatic TIF and plasma of mice orthotopically implanted with KPC 7490b syngeneic tumors.

j-k. Mass isotopologue distribution of $^{13}C_5$-uridine ribose-derived carbon after 24 h culture of ASPC1 and PATU8988S cells in media supplemented with 1 mM or 0.1 mM uridine and each with 5 mM or 0.1 mM glucose. $^{13}C_5$-U, $^{13}C_5$-uridine.

l. Schematic depicting the fate of uridine-derived ribose carbon in PDA cells actively catabolizing uridine. 3PG/2PG, 3-/2-phosphoglycerate; ATP, adenosine triphosphate; F6P, fructose-6-phosphate; HBP, hexosamine biosynthetic pathway; NAD+, nicotinamide adenine dinucleotide; PEP, phosphoenolpyruvate; PPP, pentose phosphate pathway; PRPP, phosphoribosyl pyrophosphate; R5P, ribose-5-phosphate; SBP, serine biosynthesis pathway; TCA cycle, tricarboxylic acid cycle; UDP-GlcNAc, uridine diphosphate N-acetylglucosamine; UMP, uridine monophosphate; UTP, uridine triphosphate. See "Statistics and reproducibility" (Methods) for additional information.

Statistics and Reproducibility

a. n = 4 biologically independent samples per group per cell line. Statistical significance was measured using one-way ANOVA with Dunnett's multiple comparisons test. CAPAN2 (comparison between no glucose/uridine and no glucose + 1 mM uridine, ***P = 0.0001; no glucose/uridine and 1 mM glucose/no uridine, *P = 0.021; no glucose/uridine and 0.1 mM ribose, P = ns (0.86); no glucose/uridine and 1 mM ribose, **P = 0.0093; no glucose/uridine and 10 mM ribose, ****P < 0.0001). PATU8988S (comparison between no glucose/uridine and no glucose + 1 mM uridine, ****P < 0.0001; no glucose/uridine and 1 mM glucose/no uridine, ****P < 0.0001; no glucose/uridine and 0.1 mM ribose, P = ns (0.9817); no glucose/uridine and 1 mM ribose, **P = 0.0019; no glucose/uridine and 10 mM ribose, ****P < 0.0001). DANG (comparison between no glucose/uridine and no glucose + 1 mM uridine, ****P < 0.0001; no glucose/uridine and 1 mM glucose/no uridine, ****P < 0.0001; no glucose/uridine and 0.1 mM ribose, P = ns (> 0.9999); no glucose/uridine and 1 mM ribose, P = ns (0.3025); no glucose/uridine and 10 mM ribose, ****P < 0.0001). ASPC1 (comparison between no glucose/uridine and no glucose + 1 mM uridine, ****P < 0.0001; no glucose/uridine and 1 mM glucose/no uridine, ****P < 0.0001; no glucose/uridine and 0.1 mM ribose, P = ns (0.9974); no glucose/uridine and 1 mM ribose, *P = 0.0103; no glucose/uridine and 10 mM ribose, ****P < 0.0001). The experiment was performed once.

b,c. n = 3 biologically independent samples. Statistical significance was measured using two-tailed unpaired t-test. Intracellular – comparison between no uridine and 1 mM uridine: ***P = 0.0005 (uridine), ****P < 0.0001 (uracil); Extracellular – comparison between no uridine and 1 mM uridine: ****P < 0.0001 (uridine), **P = 0.008 (uracil).

d-f. n = 3 biologically independent samples per cell line. M – mass; 'Others' – indicate M other than M+0 or M+5, where applicable. Bars shown for PATU8988S are same as the WT bars (where applicable) for that cell line in the Fig. 2-9. Tracing experiments were performed twice in these cells with similar results.

g. Number of samples: Sub-Q = 6 tumors from 3 mice injected on the left and right flanks; Ortho = 4 tumors from 4 mice. Mode of uridine injection is intratumoral for Sub-Q and intraperitoneal for Ortho.

h. Median concentration of uridine = 24.1 μM; median concentration of uracil = 90.2 μM; n = 22 biologically independent TIF samples.

i. Median concentration of glucose = 3.71 mM (plasma) and 0.63 mM (TIF). n = 8 biologically independent plasma samples and 8 TIF samples extracted from 8 tumors samples from same mice. These samples are from the control group of the study in Fig. 2.4a. Statistical significance was measured with two-tailed unpaired t test with Welch's correction, ****P < 0.0001.

j-k. j shows the measured isotopologue distribution in uridine and k shows in the indicated metabolites. n = 4 biologically independent samples per group per cell line. M – mass; 'Others' – indicate M other than M+0 or M+5, where applicable. Data (a-k) are shown as mean ± s.d. The metabolomics experiments (b-k) were performed once.

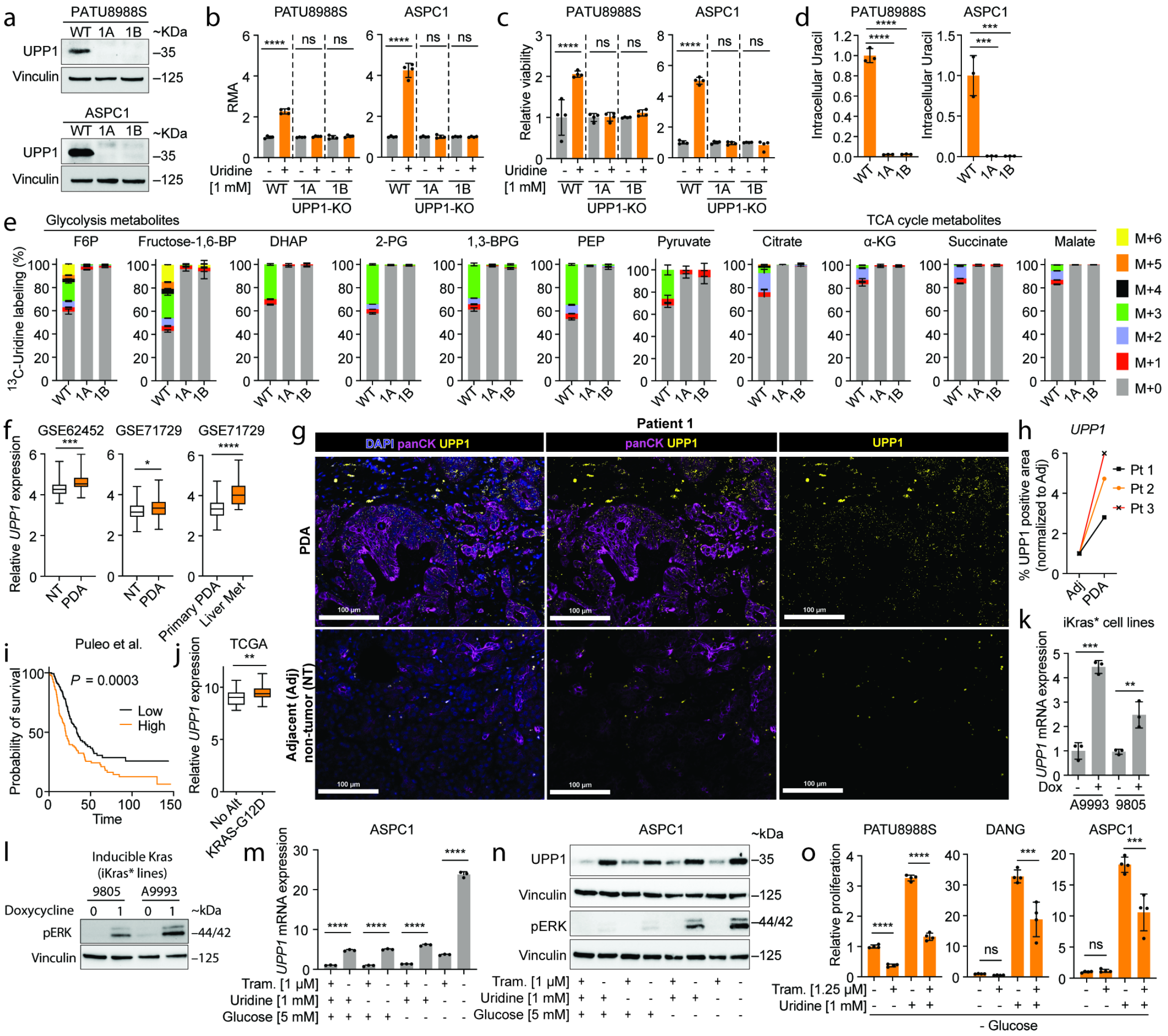

Figure 2-3 KRAS-driven *UPP1* liberates ribose and is elevated in PDA

a. Western blot validating UPP1 knockout in human PDA cell lines. kDa, molecular weight unit.

b-c. Biolog tetrazolium assay showing uridine-derived reducing potential (b) and CellTiter Glo showing ATP generation (c) in UPP1 knockout (UPP1-KO) versus WT PATU8988S and ASPC1 cells cultured with or without 1 mM uridine for 48 h.

d. Relative intracellular uracil determined with LC-MS in WT and UPP1-KO human PDA clones supplemented with 1 mM uridine for 24 h (PATU8988S) and 6 h (ASPC1).

e. Mass isotopologue distribution of 1 mM $^{13}C_5$-uridine ribose-derived carbon in glycolysis and TCA cycle metabolites in WT or UPP1-KO ASPC1 cells after 6 h.

f. *UPP1* mRNA expression in PDA tumors and non-tumoral pancreas in microarray datasets. NT – non-tumor tissue; Liver Met – liver metastasis.

g-h. RNAscope showing representative *UPP1* mRNA expression in tumor and adjacent normal tissue sections (g) and quantification from three patients (Pt1-3) (h).

i. Kaplan Meier overall survival analysis (log-rank test) by ranked *UPP1* expression from the Puleo et al. PDA dataset.

j. Comparison of *UPP1* mRNA expression in human PDA tumors annotated as KRAS G12D mutated or no alteration (No Alt) in KRAS from TCGA dataset.

k. qPCR data showing *UPP1* expression in murine cell lines (A9993 and 9805) with doxycycline-inducible oncogenic Kras (iKras*).

l. Western blot validation of MAPK pathway induction as indicated by phosphorylated ERK (pERK) in the iKras* cell lines.

m-n. qPCR for *UPP1* mRNA (m) and western blot for pERK and UPP1 (n) in ASPC1 cells with or without 5 mM glucose, 1 mM uridine, and 1 µM trametinib (tram.) for 48 h.

o. MTT assay showing relative proliferation without glucose of PDA cell lines with 1.25 µM trametinib and 1 mM uridine. See “Statistics and reproducibility” (Methods) for additional information.

Statistics and Reproducibility

a. WT, wild type. 1A, 1B denote UPP1 KO clonal cell lines. The experiment was performed once.

b. n = 4 biologically independent samples per group per cell line. Statistical significance was measured using one-way ANOVA with Tukey's multiple comparisons test. PATU8988S – comparison between no uridine (-) and 1 mM uridine (+): ****P < 0.0001, P = ns (0.9703) and P = ns (0.9089) for WT, 1A and 1B groups, respectively. ASPC1 – comparison between no uridine (-) and 1 mM uridine (+): ****P < 0.0001, P = ns (>0.9999) and P = ns (>0.9999) for WT, 1A and 1B groups, respectively. The experiments were performed three times with similar results.

c. n = 4 biologically independent samples per group per cell line. Statistical significance was measured using one-way ANOVA with Tukey's multiple comparisons test. PATU8988S – comparison between no uridine (-) and 1 mM uridine (+): ****P < 0.0001, P = ns (>0.9999) and P = ns (0.9599) for WT, 1A and 1B groups, respectively. ASPC1 – comparison between no uridine (-) and 1 mM uridine (+): ****P < 0.0001, P = ns (0.9977) and P = ns (0.6537) for WT, 1A and 1B groups, respectively. The experiments were performed twice with similar results.

d. n = 3 biologically independent samples per group. Statistical significance was measured using one-way ANOVA with Dunnett’s multiple comparisons test. Comparison between WT and clonal cells 1A or 1B: ****P < 0.0001 (PATU8988S) and ***P = 0.0003 (ASPC1). Data are part of the metabolomics experiments shown in Fig. 2-9a-c. The metabolomics experiment was performed once.

e. n = 3 biologically independent samples per group. M – mass; ‘Others’ – indicate M other than M+0 or M+5, where applicable. Data are part of the metabolomics experiments shown in Fig. 2-9 (e, h, j) for ASPC1. The metabolomics experiment was performed once.

f. Statistical significance was measured using two-tailed unpaired t test with Welch's correction. Number of samples and statistical comparison: GSE62452 (NT = 61 vs PDA = 69, ***P = 0001), GSE71729 (middle graph: NT = 46 vs PDA = 145, *P = 0.0466), GSE71729 (right graph: primary = 145 vs Liver met, PDA = 25, ****P < 0.0001). Box plot statistics – GSE42452 (NT: minima = 3.582, maxima = 5.633, 25th percentile = 4.036, 75th percentile = 4.504, median = 4.262; PDA: minima = 3.853, maxima = 5.989, 25th percentile = 4.37, 75th percentile = 4.843, median = 4.535), GSE71729 (NT: minima = 2.18, maxima = 4.402, 25th percentile = 2.901, 75th percentile = 3.469, median = 3.139; PDA: minima = 2.293, maxima = 4.725, 25th percentile = 3, 75th percentile = 3.657, median = 3.339), GSE71729 (primary: minima = 2.293, maxima = 4.725, 25th percentile = 3, 75th percentile = 3.657, median = 3.339; liver metastasis (met): minima = 3.306, maxima = 5.768, 25th percentile = 3.564, 75th percentile = 4.498, median = 4.023).

g. Representative images from Patient 1 of 3 tumor tissues. PanCK, pan-cytokeratin, stain indicates tumor cells. DAPI, nuclear stain. Adj = adjacent normal tissue. Scale bar indicates 100 µm.

i. Number of samples: UPP1 low = 144, UPP1 high = 144.

j. Number of samples: No Alt = 43, G12D = 42. Statistical significance was measured using two-tailed unpaired t test with Welch's correction, **P = 0.0029. Box plot statistics – No Alt: minima = 7.797, maxima = 10.66, median =

9.019, 25th percentile = 8.307, 75th percentile = 9.53; KRAS-G12D: minima = 8.154, maxima = 11.3, median = 9.385, 25th percentile = 9.019, 75th percentile = 9.905.

k. n = 3 biologically independent samples per cell line. Statistical significance was measured using two-tailed unpaired t test. Comparison between Dox (-) and (+) in iKras* cell A9993: ***P = 0.0002; in iKras cell 8905: **P = 0088. The experiment was performed once.

l. Vinculin is used as a loading control. The experiment was performed once.

m. Number of samples: 3 biologically independent samples per group. Statistical significance was measured using two-tailed unpaired t test. Comparison between cells cultured in uridine/glucose-containing media with and without trametinib treatment: ****P < 0.0001; comparison between cells treated with and without trametinib in the presence of glucose but no uridine: ****P < 0.0001; comparison between cells treated with and without trametinib in the presence of uridine and no glucose: **** P < 0.0001; comparison between cells cultured with no uridine/glucose with and without trametinib treatment: ****P < 0.0001. The experiment was performed once.

n. Vinculin is used as a loading control. The experiments were performed twice with similar results.

o. Statistical significance was measured using one-way ANOVA with Tukey's multiple comparisons test. n = 4 biologically independent samples per group per cell line. PATU8988S (comparison between cells cultured with and without trametinib in the absence of uridine: ****P < 0.0001, and with uridine supplementation: ****P < 0.0001), DANG (comparison between cells cultured with and without trametinib in the absence of uridine: P = ns (0.9967), and with uridine supplementation: ****P = 0.0001), ASPC1 (comparison between cells cultured with and without trametinib in the absence of uridine: P = ns (0.9987), and with uridine supplementation: ***P = 0.0001). The experiment was performed once.

ns = not significant. Data (b-e, k, m, o) are shown as mean ± s.d.

1,3-BPG, 1,3-bisphosphoglycerate; 2-PG, 2-phosphoglycerate; α-KG, alpha ketoglutarate; DHAP, dihydroxyacetone phosphate; Fructose-1,6-BP, fructose-1,6-bisphosphate; F6P, fructose-6-phosphate; PEP, phosphoenolpyruvate; TCA, tricarboxylic acid.

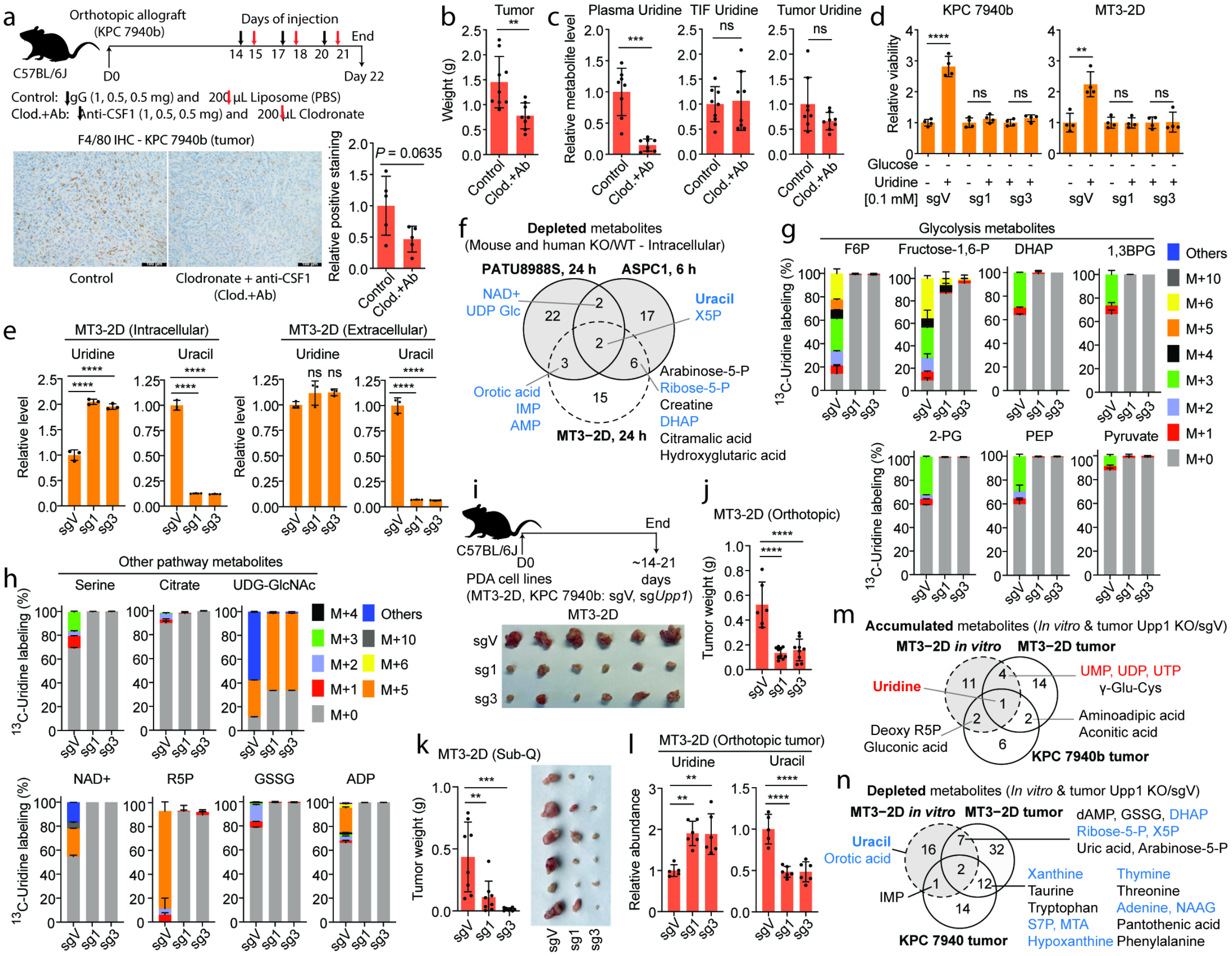

Figure 2-4 UPP1 knockout impairs growth of orthotopic pancreatic tumor allografts

a. Schematic and validation of macrophage depletion.

b. Tumor weight from control and macrophage-depleted mice at endpoint.

c. Relative plasma, tumor interstitial fluid (TIF), and bulk tumor uridine levels in samples from the control and macrophage-depleted groups, measured by LC-MS.

d. CellTiter Glo assay indicating relative viability (ATP) of *Upp1* knockout (sg1, sg3) and non-targeting control vector (sgV) murine PDA cells.

e. Relative intracellular and extracellular uridine and uracil levels in the control (sgV) versus *Upp1*-KO (sg1, sg3) MT3-2D mouse PDA cell lines, determined by LC-MS.

f. Venn diagram showing metabolites depleted in vitro upon UPP1 knockout in the human (PATU8988S and ASPC1) and mouse (MT3-2D) PDA cell lines, determined by LC-MS. Blue font: glycolysis, nucleotide biosynthesis, and pentose phosphate pathway.

g-h. Stable isotope tracing showing mass isotopologue distribution of 1 mM $^{13}C_5$-uridine ribose-derived carbon in glycolysis (g) and other pathway metabolites in the MT3-2D cells after 6 h culture.

i. Schematic of tumor studies. Below: representative photograph of tumors harvested from the mice orthotopically implanted with the control vector (sgV) or *Upp1*-KO (sg1, sg3) MT3-2D cell lines.

j. Tumor weight at endpoint in C57BL/6J mice orthotopically implanted with the MT3-2D cells.

k. Weight and photograph of tumors harvested at endpoint after subcutaneous implantation of MT3-2D cells into the C57BL/6J mice flanks (left and right).

l. Relative tumor uridine and uracil abundance in the orthotopic tumor samples described in (**i,j**), as determined by LC-MS.

m-n. Venn diagram showing metabolites commonly accumulated (m) and depleted (n) in UPP1 knockout tumors and cultured cells relative to the control murine cell lines. (m) red font: nucleotide biosynthesis; (n) blue font: glycolysis, nucleotide biosynthesis, and pentose phosphate pathway. See "Statistics and reproducibility" (Methods) for additional information.

Statistics and Reproducibility

a. The experiment involved a sequential treatment of mice with control IgG followed the next day by liposome PBS (control group) or anti-CSF1 followed the next day by clodronate (Clod.+Ab/macrophage depletion group), after the establishment of palpable pancreatic orthotopic tumors with the KPC 7940b cell line. Below: immunohistochemistry images showing macrophage marker, F4/80, staining in the tumor. Right: quantification of F4/80 positive cells normalized to the control group. Data shown represent the average of quantification from 3 histological slides obtained per tumor. Sample size used for histology, n = 5 tumors from same number of mice per group. Statistical significance was measured using two tailed unpaired t test with Welch's correction, P = 0.0635. CSF1, colony stimulating factor 1 (CSF1); PBS, phosphate buffered saline. The experiment was performed once.

b. Sample size: control = 9, Clod.+Ab = 8 tumors from the corresponding number of mice. Statistical significance was measured using two-tailed unpaired t test with Welch's correction, **P = 0.0046. Ab = anti-CSF1 antibody.

c. Plasma n=8; TIF, n=8 control and macrophage-depleted (n=8); tumors, n=8 control and n=8 macrophage-depleted. Statistical significance was measured using two-tailed unpaired t test with Welch's correction. Comparison between control and Clod.+Ab (plasma uridine): *** P = 0.0003; control and Clod.+Ab (TIF uridine): P = ns (0.7923); control and Clod.+Ab (tumor uridine): P = ns (0.1244). Ab = anti-CSF1 antibody.

d. The cells were cultured +/- 1 mM uridine in glucose-free media supplemented with 2.5% dFBS. Sample size = 4 biologically independent samples per group. Statistical significance was measured using two-tailed unpaired t-test. KPC 7940b – comparison of cell culture without and with 0.1 mM uridine: ****P < 0.0001, P = ns (0.2577) and P = ns (0.1118) for sgV, sg1 and sg3 groups, respectively; MT3-2D – comparison of cell culture without and with 0.1 mM uridine: **P = 0.0026, P = 0.9574 and P = 0.927 for sgV, sg1 and sg3 groups, respectively. The experiments were performed twice with similar results.

e. Statistical significance was measured using one-way ANOVA with Dunnett's multiple comparisons test, n = 3 biologically independent samples per group. Comparison between sgV and sg1 or sg3: ****P < 0.0001 (for both intracellular uridine and uracil). Extracellular uridine – comparison between sgV and sg1, P = ns (0.1758); comparison between sgV and sg3, P = ns (0.1503). Extracellular uracil – comparison between sgV and sg1 or sg3: ****P < 0.0001.

f. In blue font are components of glycolysis, nucleotide biosynthesis or pentose phosphate pathway.

g,h. n = 3 biologically independent samples per group. The metabolomics experiment was performed once.

i. Tumor weight data is shown in j.

j. Number of mice and tumor samples: sgV n = 6, sg1 n = 10, and sg3 n = 8. Statistical significance was measured using one-way ANOVA with Dunnett's multiple comparisons test. Comparison between sgV and sg1 or sg3: ****P < 0.0001. Experiment performed once.

k. Number of samples: sgV = 8, sg1 = 8, sg3 = 8 tumors, corresponding to four mice per group. Statistical significance was measured using one-way ANOVA with Dunnett's multiple comparisons test. Comparison between sgV and sg1: **P = 0.003, comparison between sgV and sg3: ***P = 0.0002. On the right is an accompanying representative image of the weighed tumors. Experiment performed once.

l. Samples used for metabolomics per group: sgV = 5, sg1 = 6, sg3 = 6. Statistical significance was measured using one-way ANOVA with Dunnett's multiple comparisons test. Uridine – comparison between sgV and sg1: **P = 0.0016, sgV and sg3: **P = 0.0019); uracil – comparison between sgV and sg1: ****P < 0.0001, sgV and sg3: ****P < 0.0001. Experiment performed once.

m. Venn diagram showing metabolites commonly accumulated upon UPP1 knockout in mouse cell line (in vitro) and tumors (in vivo), as determined by metabolomics profiling. In red font are components of nucleotide biosynthesis.

n. Venn diagram showing metabolites commonly depleted upon UPP1 knockout in mouse cell line (in vitro) and in tumors, as determined by metabolomics profiling. In blue are components of glycolysis, nucleotide biosynthesis or pentose phosphate pathway.

1,3BPG, 1,3-bisphosphoglcerate; 2-PG, 2-phosphoglycerate; AMP, adenosine monophosphate; dAMP, deoxy-adenosine monophosphate; DHAP, dihydroxyacetone-phosphate; F6P, fructose 6-phosphate; F1,6P, fructose 1,6-bisphosphate; GSSG, oxidized glutathione; IMP, inosine monophosphate; NAD+, nicotinamide adenine dinucleotide; PEP, phosphoenolpyruvate; R5P, ribose 5-phosphate; UDP-Glc, uridine diphosphate-glucose; UDP-GlcNAc, uridine diphosphate N-acetylglucosamine; X5P, xylulose 5-phosphate.

Data (a-e, g-h, j-k, l) are shown as mean ± s.d. Metabolites used for Venn diagram (f, m, n) are significantly changed ($P<0.05$) in the metabolomics profile of UPP1 KO compared to control per cell line and were derived from LC-MS experiments [Fig. 2.3d and c (PATU8988S and ASPC1 – intracellular); Fig. 2.4e/Fig. 2.14c (MT3-2D cell line, in vitro, intracellular); Fig. 2.4l/Fig. 2.14g (MT3-2D tumors, in vivo), and Fig. 2.14e/f (KPC 7940b tumors, in vivo)]. The statistical significance was determined using *limma* package version 3.38.3 in R. Mouse schematic (a, i) was drawn with Adobe Illustrator 2021 version 25.4.3.

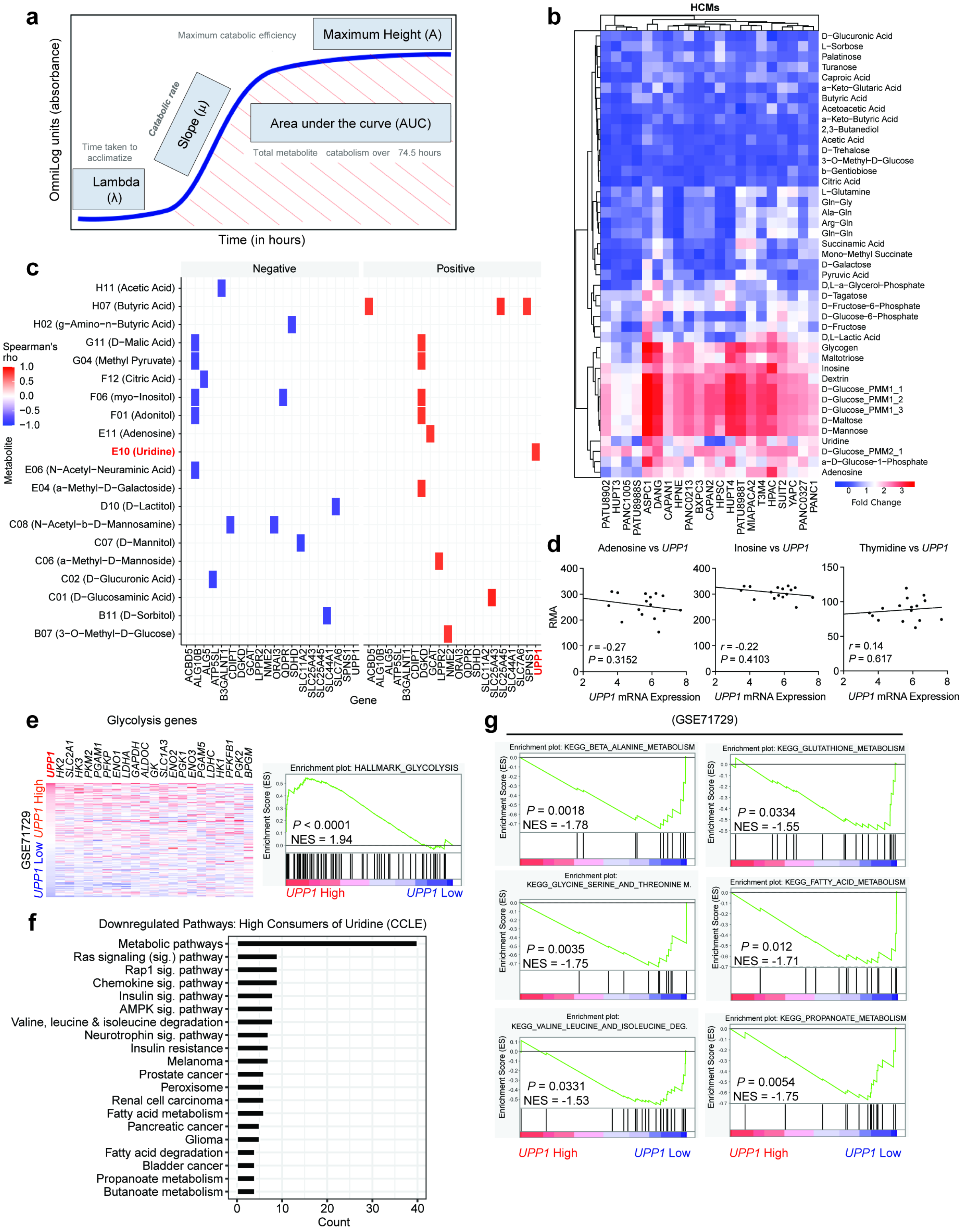

Figure 2-5 Correlation of nutrient utilization with gene expression identifies uridine and UPP1

a. Schematic overview of the parameters measured by the Biolog Phenotype Microarray.

b. Heatmap showing the high confidence metabolites (HCMs), namely, the metabolites that were the least utilized or the most utilized. Legend denotes relative usage, where red shows high utilization and blue shows low utilization.

c. Spearman correlation plot, indicating the genes that showed positive or negative correlation with metabolites' RMA in the Biolog screen.

d. Spearman correlations, r, between UPP1 expression from the CCLE and RMA of nucleosides that were included in the Biolog screen. n = 16 PDA cell lines.

e. Heatmap showing the expression of glycolysis genes in human PDA tumors ranked based on UPP1 expression (dataset: GSE71729, *UPP1* low, n=72; high, n=73). On the right: GSEA plot indicating the enrichment of glycolysis hallmark in the *UPP1* high relative to the low tumors. NES, normalized enrichment score.

f. Downregulated pathways in PDA cell lines that metabolize uridine at a high level, as revealed by gene ontology (GO) analysis of the differentially expressed genes ($P<0.05$). GO analysis was performed with DAVID (https://david.ncifcrf.gov/tools.jsp). Analysis was based on the differential genes derived from CCLE data and part of the data shown in Fig. 1g.

g. GSEA plots of significantly enriched KEGG pathways in UPP1-high PDA tumors relative to UPP1 low tumors. Plots are part of the data (e) from the analysis of GSE71729 human PDA dataset.

Statistics and reproducibility: a. The kinetic measurement evaluated several parameters, including the time taken for cells to adapt to and catabolize a nutrient (lambda), the rate of uptake and catabolism (mu or slope), the total metabolic activity (area under the curve; AUC), and the maximum metabolic activity. The values from the maximum catabolic efficiency (maximum height, A) of the respective metabolites were used to determine relative metabolic activity (RMA).

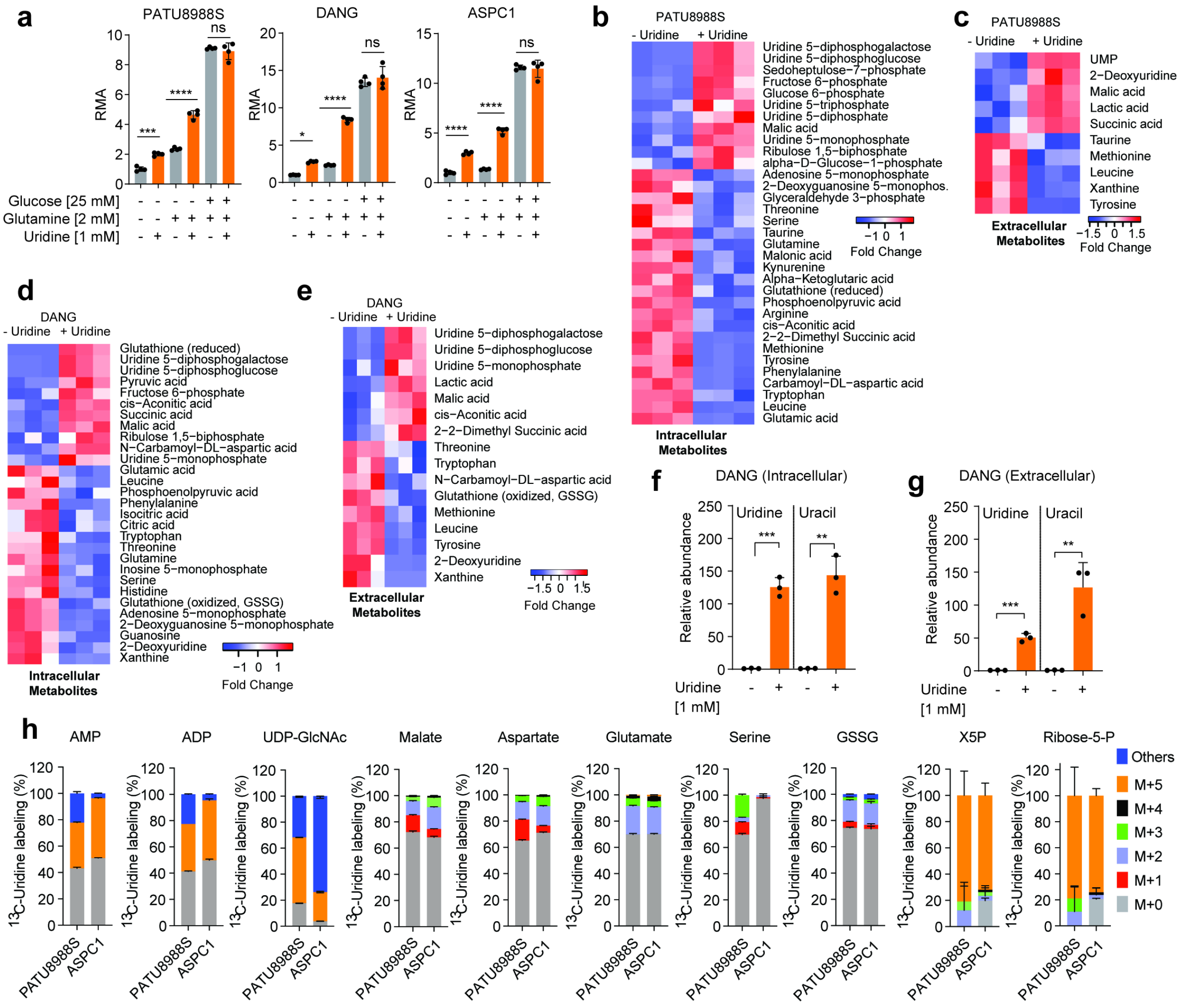

Figure 2-6 Nutrient-deprived PDA use uridine to support metabolism

a. Relative RMA upon uridine supplementation with or without glucose and glutamine. n = 4 biologically independent samples per group per cell line.

b-c. Differential changed (*P* < 0.05) intracellular (b) and extracellular (c) metabolites from PATU8988S cells supplemented with 1 mM uridine in glucose-free media for 24 h, as determined by LC-MS metabolomics. n = 3 biologically independent samples per group.

d-e. Differentially changed (*P* < 0.05) intracellular (d) and extracellular (e) metabolites from DANG cells supplemented with 1 mM uridine in glucose-free media for 24 h, as determined by LC-MS metabolomics. n = 3 biologically independent samples per group.

f. Intracellular and **g**) extracellular uridine and uracil from DANG cells supplemented with 1 mM uridine in glucose-free media for 24 h, as determined by LC-MS. Plots in f-g are from the same experiment as d-e. n = 3 biologically independent samples per group. Statistical significance was measured using two-tailed unpaired t-test. Intracellular – comparison between no uridine and 1 mM uridine: *** P = 0.0001 for uridine, ** P = 0.0011 for uracil. Extracellular – comparison between no uridine and 1 mM uridine: *** P = 0.0002 for uridine, ** P = 0.0044 for uracil.

h. Mass isotopologue distribution of $^{13}C_5$-uridine ribose-derived carbon in the displayed metabolites after 24 h culture in a glucose-free media supplemented with 1 mM $^{13}C_5$-uridine. n = 3 biologically independent samples per cell line. Tracing experiments were performed twice in these cells with similar results. Data (a, f, g, h) are shown as mean ± s.d. ADP, adenosine diphosphate; GSSG, oxidized glutathione; UDP-GlcNAc, uridine diphosphate N-acetylglucosamine; X5P, xylulose 5-phosphate.

Statistics and Reproducibility: a. n = 4 biologically independent samples per group per cell line. Statistical significance was measured using one-way ANOVA with Tukey's multiple comparisons test. PATU8988S (comparison between cells cultured in (-) glucose/glutamine/uridine and (-) glucose/glutamine/+uridine: *** P = 0.0007, comparison between (-) and (+) uridine in the presence of glutamine and without glucose: **** P < 0.00001, comparison between (-) and (+) uridine in the presence of glutamine and glucose: P = ns (0.8856)). DANG (comparison between cells cultured in (-) glucose/glutamine/uridine and (-) glucose/glutamine/+uridine: * P = 0.0165, comparison between (-) and (+) uridine in the presence of glutamine and without glucose: **** P < 0.0001, comparison between (-) and (+) uridine in the presence of glutamine and glucose: P = ns (0.7971)). ASPC1 (comparison between cells cultured in (-) glucose/glutamine/uridine and (-) glucose/glutamine/+uridine: **** P < 0.0001, comparison between (-) and (+) uridine in the presence of glutamine and without glucose: **** P < 0.00001, comparison between (-) and (+) uridine in the presence of glutamine and glucose: P = ns (0.9968)). Metabolomics (b-e) significance test was determined using the *limma* package version 3.38.3 in R. The experiments (a-e) were performed once.

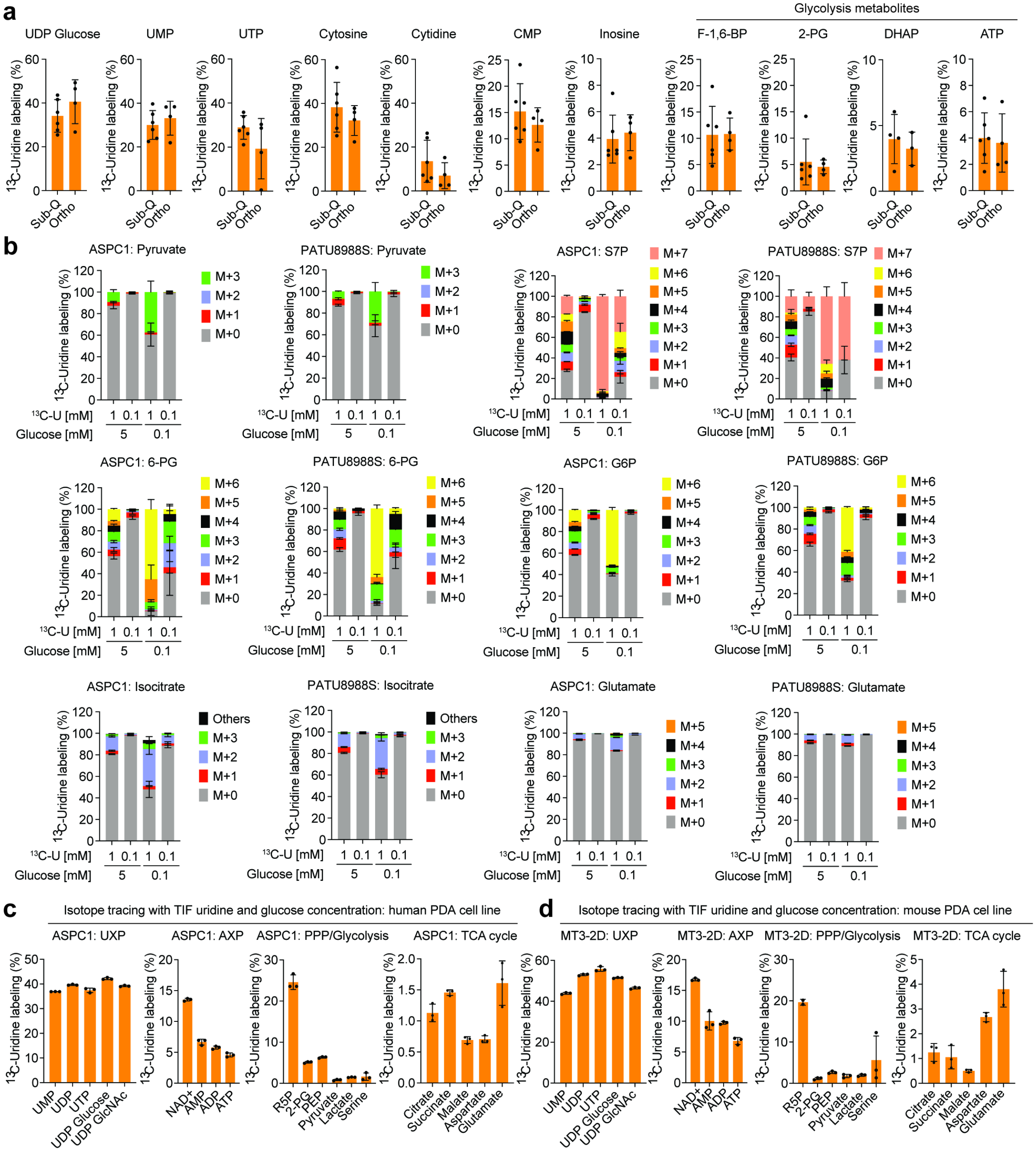

Figure 2-7 PDA metabolize uridine via central carbon metabolism *in vitro* and *in vivo*

a. Isotope tracing showing $^{13}C_5$-uridine ribose-derived carbon labeling in subcutaneous (Sub-Q) or orthotopically (Ortho) implanted KPC 7940b tumors collected 1 h after injecting the mice with 200 µL or 50 µL (Sub-Q) 0.2 M $^{13}C_5$-uridine. Number of samples: Sub-Q = 6 tumors from 3 mice injected on the left and right flanks; Ortho = 4 tumors from 4 mice. Mode of uridine injection is intratumoral for Sub-Q and intraperitoneal for Ortho.

b. Mass isotopologue distribution of $^{13}C_5$-uridine ribose-derived carbon after 24 h culture of ASPC1 and PATU8988S cells in media supplemented with 1 mM or 0.1 mM uridine, each with 5 mM or 0.1 mM glucose concentration. n = 4 biologically independent samples per group. M – mass; 'Others' – indicate M other than M+0 or M+5, where applicable.

c-d. Isotope tracing showing metabolite labeling upon supplementation with $^{13}C_5$-uridine at the TIF uridine and glucose concentrations shown in Figure 2h-i, after 12 hours of culturing **c**) human PDA cell line ASPC1 and **d**) murine PDA cell line MT3-2D. The cell lines were cultured in media supplemented with 25 µM $^{13}C_5$-uridine and 0.65 mM glucose. n = 3 biologically independent samples per cell line. AXP – AMP, ADP, ATP, and related metabolites; UXP – UMP, UDP, UTP and related metabolites. The experiments (a-d) were performed once. Data (a-d) are shown as mean ± s.d, where applicable.

$^{13}C_5$-U, $^{13}C_5$-uridine; 2-PG, 2-phosphoglycerate; 6-PG, 6-phosphogluconate; ADP, adenosine diphosphate; AMP, adenosine monophosphate; ATP, adenosine triphosphate; DHAP, dihydroxyacetone phosphate; F1,6-BP, fructose 1,6-bisphosphate; CMP, cytidine monophosphate; G6P, glucose 6-phosphate; NAD+, nicotinamide adenine dinucleotide; R5P, ribose 5-phosphate; PEP, phosphoenolpyruvate; PPP, pentose phosphate pathway; TCA, tricarboxylic acid; S7P, sedoheptulose 7-phosphate; UDP, uridine diphosphate; UMP, uridine monophosphate; UTP, uridine triphosphate; UDP-GlcNAc, uridine diphosphate N-acetylglucosamine.

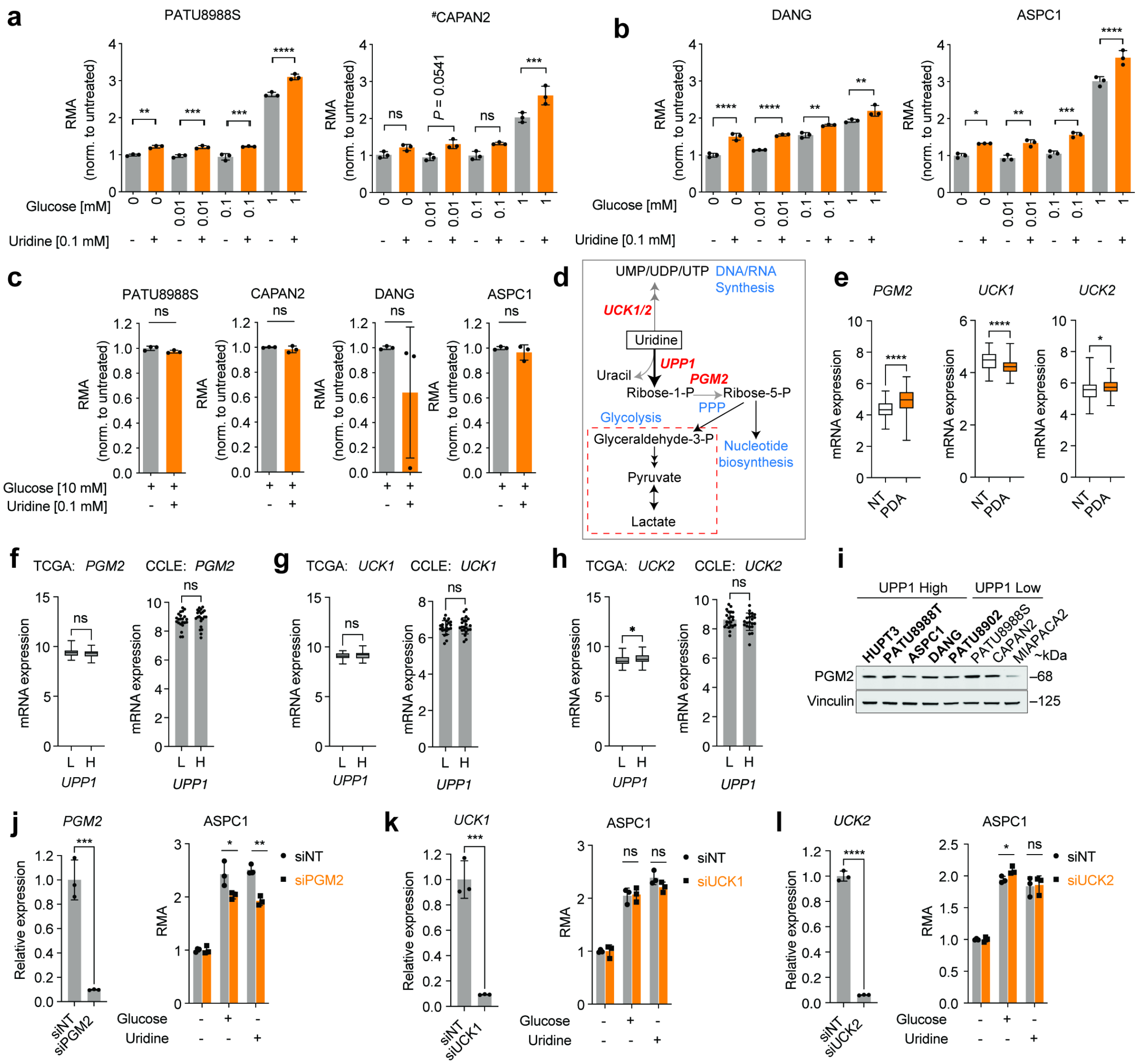

Figure 2-8 Cellular pathways for ribose salvage from uridine

a-c. Relative metabolic activity (RMA) of PDA cell lines depicting the preferential use of uridine at (**a,b**) low glucose concentration (0-1 mM) but not at **c**) the high glucose concentration (10 mM), over a 96 h culture.

d. Schematic depicting metabolic pathways for uridine utilization.

e. Expression of *PGM2*, *UCK1*, and *UCK2* in non-tumor (NT) and PDA tissue samples from the GSE71729 dataset. Number of samples: NT = 46, PDA = 145.

f-h. Expression of PGM2, UCK1 and UCK2 in TCGA (human PDA tumor) and CCLE (human cell line) data separated into UPP1 low (L) and high (H) subsets.

i. Western blot for PGM2 in PDA cell lines. Presented in red are cells that express high UPP1. These samples are the same batch as the data shown in **Fig. 1e** and the blot was generated during one of the technical replicates of that western blotting. kDa, molecular weight unit.

j. qPCR for PGM2 in ASPC1 cells transfected with siPGM2 compared to non-targeting (siNT) control. On the right: RMA in PGM2 knockdown cells +/- uridine (1 mM) or glucose (1 mM).

k. qPCR for UCK1 in ASPC1 cells transfected with siUCK1 compared to non-targeting (siNT) control. On the right: RMA in UCK1 knockdown cells +/- uridine (1 mM) or glucose (1 mM).

l. qPCR for UCK2 in ASPC1 cells transfected with siUCK2 compared to non-targeting (siNT) control. On the right: RMA in UCK2 knockdown cells +/- uridine (1 mM) or glucose (1 mM).

Statistics and Reproducibility: a-c. n = 3 biologically independent samples. Statistical significance for data in a-b was measured using one-way ANOVA with Tukey's multiple comparisons test. PATU8988S (comparison between no glucose and no glucose + uridine [0.1 mM]: **P = 0.0017; 0.01 mM glucose and 0.01 mM glucose + uridine: ***P = 0.0008; 0.1 mM glucose and 0.1 mM glucose + uridine: ***P = 0.0002; 1 mM glucose and 1 mM glucose + uridine: ****P < 0.0001). CAPAN2 (comparison between no glucose and no glucose + uridine: P = ns (0.5673); 0.01 mM glucose and 0.01 mM glucose + uridine: P = ns (0.0541); 0.1 mM glucose and 0.1 mM glucose + uridine: P = ns (0.092); 1 mM glucose and 1 mM glucose + uridine: ***P = 0.0007. $^{\#}$ All four group comparisons have significant P: 0.0468, 0.014, 0.0089, 0.0222, respectively, when directly compared using two-tailed unpaired t test). DANG (comparison between no glucose and no glucose + uridine: ****P < 0.0001; 0.01 mM glucose and 0.01 mM glucose + uridine: ****P < 0.0001; 0.1 mM glucose and 0.1 mM glucose + uridine: **P = 0.0051; 1 mM glucose and 1 mM glucose + uridine: **P = 0.0051). ASPC1 (comparison between no glucose and no glucose + uridine: *P = 0.0203; 0.01 mM glucose and 0.01 mM glucose + uridine: **P = 0.0031; 0.1 mM glucose and 0.1 mM glucose + uridine: ***P = 0.0003; 1 mM glucose and 1 mM glucose + uridine: ****P < 0.0001). Statistical significance for data in c was measured using two-tailed unpaired t test and P = ns (0.0852, 0.3509, 0.3021 and 0.3875 for PATU8988S, CAPAN2, DANG and ASPC1, respectively, in the comparison of no uridine vs 0.1 mM uridine groups in the presence of 10 mM glucose).

d. Uridine can be channeled into DNA or RNA synthesis by direct phosphorylation from UCK1/2. Uridine can also be catabolized via UPP1 to produce uracil and ribose 1-phosphate. Ribose 1-phosphate is converted to ribose-5-phosphate by PGM2 and fuel pentose phosphate pathway, nucleotide biosynthesis and glycolysis.

e. Statistical significance was measured using two-tailed unpaired t test with Welch's correction. Comparison between NT and PDA: *PGM2*, ****P < 0.0001; *UCK1*, ****P < 0.0001; *UCK2*, *P = 0.018. Box plot statistics – PGM2 (NT: minima =3.097, maxima = 5.527, median = 4.335, 25th percentile = 3.992, 75th percentile = 4.74; PDA: minima = 2.386, maxima = 6.433, 25th percentile = 4.424, median = 4.961, 75th percentile = 5.457), UCK1 (NT: minima = 3.7, maxima =5.1, median = 4.5, 25th percentile = 4.2, 75th percentile = 4.7; PDA: minima = 3.6, maxima = 5.1, median = 4.2, 25th percentile = 4, 75th percentile = 4.4), UCK2 (NT: minima = 4.034, maxima = 7.615, median = 5.577, 25th percentile = 5.095, 75th percentile = 5.9; PDA: minima = 4.556, maxima = 6.93, median = 5.727, 25th percentile = 5.458, 75th percentile = 6.059).

f-h. Number of samples: TCGA – UPP1 low = 75, high = 75; CCLE – UPP1 low = 22, high = 22. Statistical significance was measured using two-tailed unpaired t test with Welch's correction. Comparison between L and H groups in TCGA (PGM2: P = ns (0.1226), UCK1: P = ns (0.311); UCK2: *P = 0.0327). In the CCLE L versus H comparison, PGM2, UCK1 and UCK2 have P = ns (0.3486, 0.4645, 0.4381, respectively). TCGA – The Cancer Genome Atlas, CCLE – Cancer Cell Line Encyclopaedia.

i. Vinculin is used as a loading control.

j. Number of samples: qPCR = 3, RMA = 3 biologically independent samples per group. qPCR – statistical significance was measured using two-tailed unpaired t test; comparison between siNT and siPGM2: ***P = 0.0007. RMA – statistical significance was measured using multiple unpaired t tests with two-stage two-step method; comparison of siNT and siPGM2 in the presence of 1 mM glucose and no uridine: *P = 0.0452, and **P = 0.0014 in the presence of 1 mM uridine and no glucose.

k. Number of samples: qPCR = 3, RMA = 3 biologically independent samples per group. qPCR – statistical significance was measured using two-tailed unpaired t test; comparison between siNT and siUCK1: ***P = 0.0004. RMA – statistical significance was measured using multiple unpaired t tests with two-stage two-step method.

Comparison of siNT and siUCK1 knockdown samples in the presence of 1 mM glucose and no uridine: P = ns (0.8652), and P = ns (0.131) in the presence of 1 mM uridine and no glucose.

l. Number of samples: qPCR = 3, RMA = 3 biologically independent samples per group. qPCR – statistical significance was measured using two-tailed unpaired t test; comparison between siNT and siUCK2: ****P < 0.0001. RMA – statistical significance was measured using multiple unpaired t tests with two-stage two-step method; comparison of siNT and siUCK1 knockdown cells in the presence of 1 mM glucose and no uridine: *P = 0.035, and P = ns (0.8653) in the presence of 1 mM uridine and no glucose. Data (a-c, f-h, j-l) are shown as mean ± s.d. The experiments were performed once (a-c, k), and twice (j, l) with similar results.

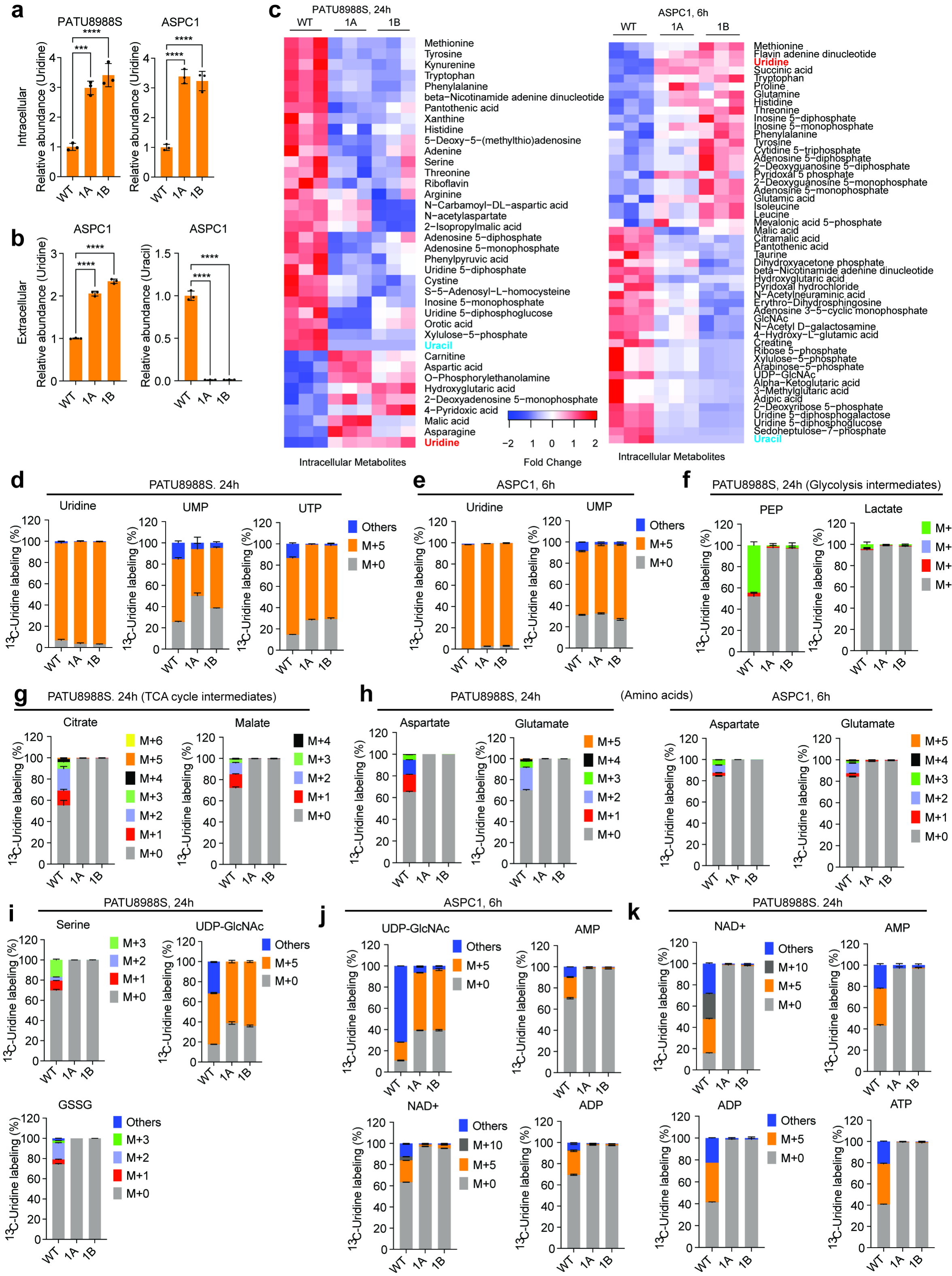

Figure 2-9 UPP1 mediates the liberation of uridine-derived ribose for central carbon metabolism

a. Relative intracellular uridine level in the UPP1 knockout PATU8988S cells (after 24 h) and ASPC1 cells (6 h) compared to the wild type supplemented with 1 mM uridine in media with 10% dFBS and no glucose. n = 3 biologically independent samples per group per cell line. Statistical significance was measured using one-way ANOVA with Dunnett's multiple comparisons test. PATU8988S (intracellular uridine) – comparison between WT and 1A, ***P = 0.0002; comparison between WT and 1B, ****P < 0.0001. ASPC1 (intracellular uridine) – comparison between WT and 1A or 1B, ****P < 0.0001.

b. Relative extracellular uridine and uracil in UPP1 knockout ASPC1 cells compared to the wild type supplemented with 1 mM uridine for 6 h in media with 10% dFBS and no glucose. n = 3 biologically independent samples per group. Statistical significance was measured using one-way ANOVA with Dunnett's multiple comparisons test. Extracellular uridine: comparison between WT and 1A or 1B, ****P < 0.0001; extracellular uracil: comparison between WT and 1A or 1B, ****P < 0.0001.

c. Heatmaps of significantly altered intracellular metabolites (P < 0.05) in PATU8988S cells after 24 h (left) and ASPC1 after 6 h (right), as measured by LC-MS metabolomics. Data used for the intracellular uridine/uracil plots (a-b) were extracted from this profiling study.

d-k. Mass isotopologue distribution of 1 mM $^{13}C_5$-uridine ribose-derived carbon into the indicated metabolic pathways in wildtype (WT) or UPP1-KO PATU8988S and ASPC1 cells. M – mass; 'Others' – indicate M other than M+0 or M+5, where applicable. 1A and 1B denote UPP1-KO sgRNA clones. Data (a-b, d-k) are shown as mean ± s.d. Metabolomics experiments were done once.

Statistics and Reproducibility: Abbreviations – ADP, adenosine diphosphate; ATP, adenosine triphosphate; AMP, adenosine monophosphate; GSSG, oxidized glutathione; NAD+ nicotinamide adenine dinucleotide; PEP, phosphoenolpyruvate; TCA cycle, tricarboxylic acid cycle; UDP-GlcNAc, uridine diphosphate N-acetylglucosamine; UMP, uridine monophosphate; UTP, uridine triphosphate.

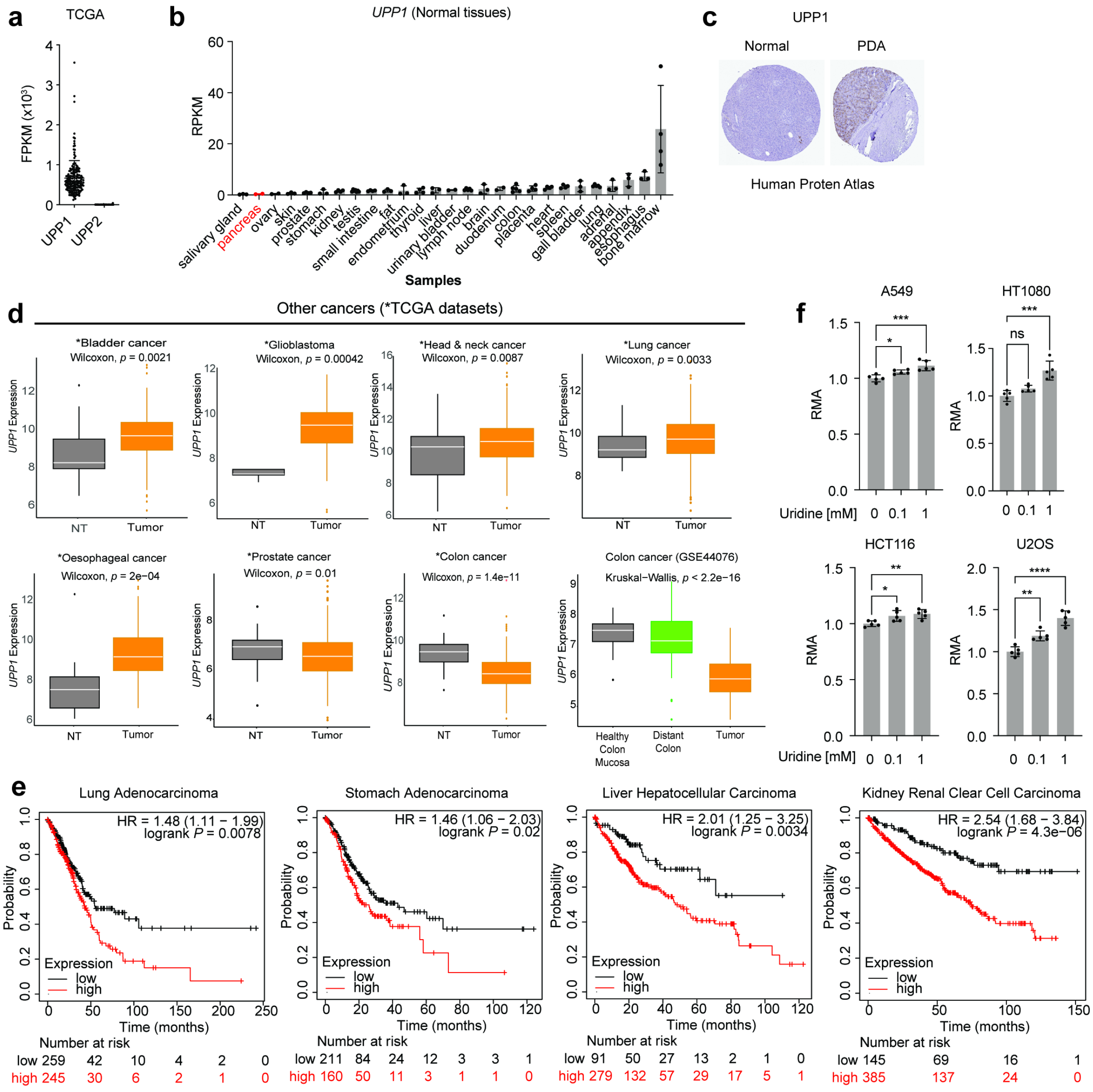

Figure 2-10 UPP1 expression is elevated in PDA and other cancer types

a. TCGA RNA seq data showing the expression of *UPP1* and its paralog *UPP2*. FPKM, fragments per kilobase of exon per million mapped fragments.

b. RNA seq showing UPP1 expression in various normal human tissues (Human Protein Atlas data), as obtained from the National Center for Biotechnology Information (NCBI) portal.

c. Histological data showing UPP1 protein expression in normal pancreatic tissue compared to PDA.

d. UPP1 expression in human non-PDA cancers accessed in publicly accessible datasets.

e. Kaplan-Meier plot of survival probability (log-rank test) as obtained from KM-plotter (https://kmplot.com/analysis/) using the default parameters.

f. Relative Metabolic Activity (RMA), reflecting NADH levels, in human non-PDA cancer cell lines supplemented with uridine (as indicated) in 1 mM glucose media. n=5 biologically independent samples per group per cell line. Statistical significance was measured using one-way ANOVA with Dunnett's multiple comparisons test. A549 (lung cancer cell line, comparison between no uridine and 0.1 mM uridine, *P = 0.0405 or 1 mM uridine, ***P = 0.0004); HT1080 (fibrosarcoma cell line, comparison between no uridine and 0.1 mM uridine, P = ns (0.1773) or 1 mM uridine, ***P = 0.0001); HCT116 (colon cancer cell line, comparison between no uridine and 0.1 mM uridine, *P = 0.0294 or 1 mM uridine, **P = 0.0081); U2OS (osteosarcoma cell line, comparison between no uridine and 0.1 mM uridine, **P = 0.002 or 1 mM uridine, ****P < 0.0001).

Statistics and Reproducibility: a, n=150 samples each.

b. Sample size, n: salivary gland = 3, pancreas = 2, ovary = 2, skin = 3, prostate = 4, stomach = 3, kidney = 4, testis = 7, small intestine = 4, fat = 3, endometrium = 3, thyroid = 4, liver = 3, urinary bladder = 2, lymph node = 5, brain = 3, duodenum = 2, colon = 5, placenta = 4, heart = 4, spleen = 4, gall bladder = 3, lung = 5, adrenal = 3, appendix = 3, esophagus = 3, bone marrow = 4. RPKM, reads per kilobase of exon per million reads mapped. *UPP1* expression in normal pancreas is extremely low (second lowest of the > 25 tissues compared).

c. Data obtained from the Human Protein Atlas (URL for 'Normal' - https://www.proteinatlas.org/ENSG00000183696-UPP1/tissue/pancreas; PDA – https://www.proteinatlas.org/ENSG00000183696-UPP1/pathology/pancreatic+cancer#img).

d. Sample size, n: NT = 19, tumor = 408 (bladder cancer, TCGA); NT = 5, tumor = 154 (glioblastoma, TCGA); NT = 44, tumor = 520 (head and neck cancer, TCGA); NT = 59, tumor = 551 (lung cancer, TCGA); NT = 11, tumor = 184 (oesophageal cancer, TCGA); NT = 52, tumor = 497 (prostate cancer, TCGA); NT = 41, tumor = 452 (colon cancer); health colon mucosa = 50, distant colon = 98, tumor = 98 (colon cancer, GSE44076). NT – non-tumor/adjacent normal tissue. Data (a-b, f) shown as mean ± s.d. The experiments were performed three times with similar results. Box plot statistics – TCGA, bladder carcinoma (primary: minima= 5.83, maxima = 13.5, median = 9.77, 25th percentile = 9.015, 75th percentile = 10.47; normal: minima = 6.61, maxima = 12.43, median = 8.35, 26th percentile = 8.03, 75th percentile = 9.59); glioblastoma multiforme (primary: minima = 5.71, maxima = 11.84, median = 9.585, 25th percentile = 8.79, 75th percentile = 10.143; normal: minima = 7.04, maxima = 7.63, median = 7.4, 25th percentile = 7.36, 75th percentile = 7.61); head and neck squamous cell carcinoma (primary: minima = 6.59, maxima = 15.64, median = 10.75, 25th percentile = 9.787, 75th percentile = 11.565; normal: minima = 6.38, maxima = 13.73, median = 10.42, 25th percentile = 8.672, 75th percentile = 11.065); lung adenocarcinoma (primary: minima = 6.45, maxima = 13.44, median = 9.8, 25th percentile = 9.13, 75th percentile = 10.49; normal: minima = 8.3, maxima = 11.39, median = 9.3, 25th percentile = 8.945, 75th percentile = 9.93); esophageal carcinoma (primary: minima = 6.7, maxima = 13.08, median = 9.26, 25th percentile = 8.578, 75th percentile = 10.21; normal: minima = 6.17, maxima = 12.39, median = 7.62, 25th percentile = 6.7, 75th percentile = 8.26); prostate adenocarcinoma (primary: minima = 3.96, maxima = 9.69, median = 6.58, 25th percentile = 5.98, 75th percentile = 7.14; normal: minima = 4.56, maxima = 8.62, median = 6.97, 25th percentile = 6.447, 75th percentile = 7.24); colon cancer (primary: minima = 6.41, maxima = 12.96, median = 8.535, 25th percentile = 8.068, 75th percentile = 9.07; normal: minima = 7.76, maxima = 11.29, median = 9.57, 25th percentile = 9.09, 75th percentile = 9.92). Colon cancer (GSE44076, primary: minima = 4.564, maxima = 7.608, median = 5.917, 25th percentile = 5.487, 75th percentile = 6.405; normal: minima = 4.568, maxima = 9.154, median = 7.18, 25th percentile = 6.781, 75th percentile = 7.824; healthy colon mucosal cells: minima = 5.884, maxima = 8.279, median = 7.529, 25th percentile = 7.153, 75th percentile = 7.74). Statistical significance was tested using two-sided Wilcoxon or Kruskal-Wallis tests.

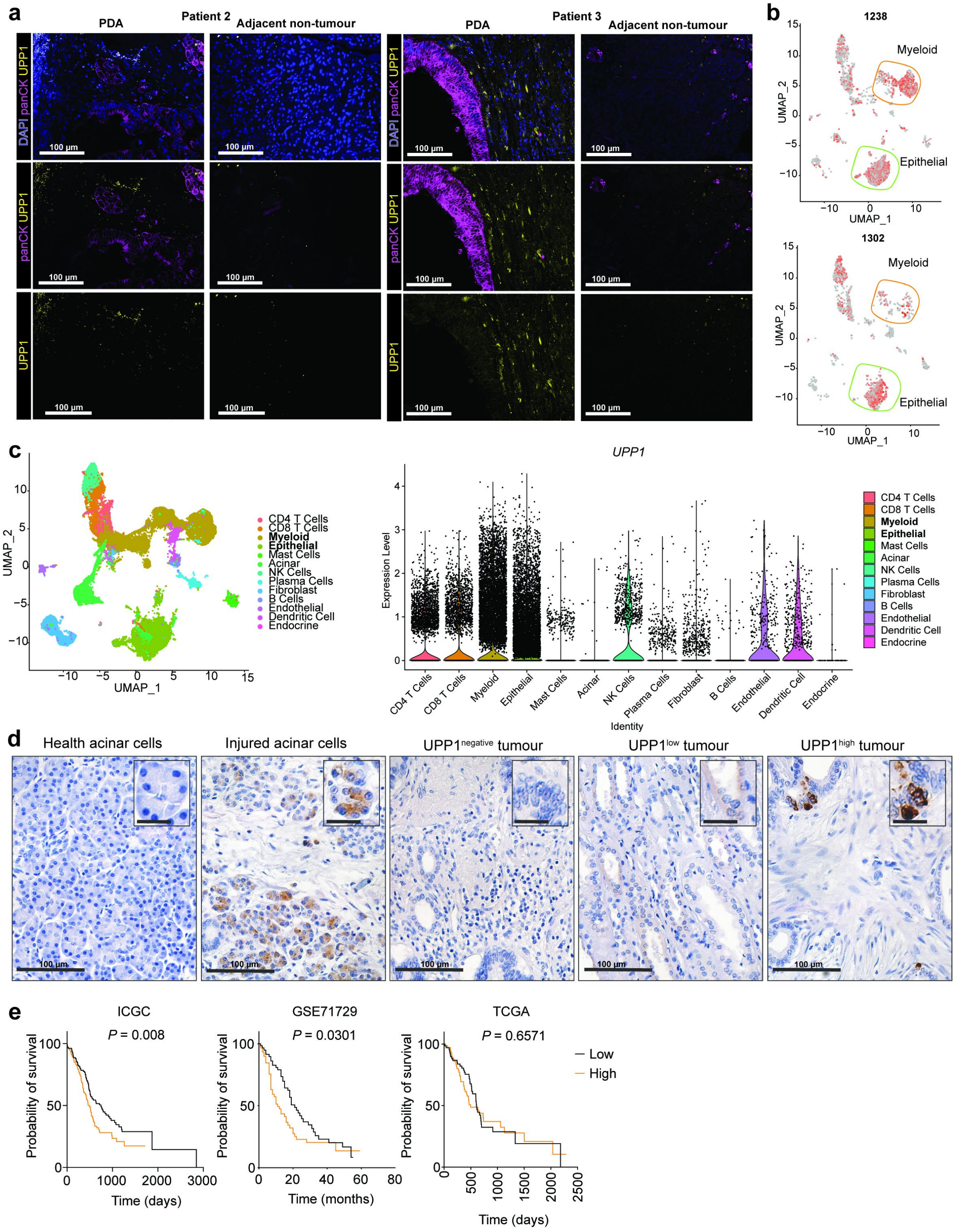

Figure 2-11 UPP1 is expressed in PDA and TME cells and predict survival outcome

a. RNAscope images showing UPP1 expression in tumor (PDA) compared to the adjacent non-tumor (Adj) in tissues. Pan-cytokeratin (PanCK) indicates the tumor cells; DAPI, nuclear stain. The images are representative of three 20x acquisitions per tissue slide, and of two independent experiments. Scale bar indicates 100 µm.

b. UMAP plot showing the expression of *UPP1* at the transcript level, as determined by single cell RNA seq of PDA tissues from two patients (#1238 and 1302).

c. Right, violin plots showing UPP1 expression in various tumor microenvironment cell types, including myeloid and epithelial cells where UPP1 is highest. Left, UMAP plot showing the specific cell compartments expressing UPP1 for all patients' samples combined (n=16). Data used in plots b-c are from a previously published dataset[57].

d. Immunohistochemistry of UPP1 in patient biopsy sections from previously published tissue microarray[53]. Micrographs are representative from 213 patient samples in the microarray and two independent experiments. Large scale bar indicates 100 µm; scale bar on insets indicates 25 µm.

e. Kaplan-Meier plot showing survival probability (log-rank test) based on *UPP1* expression in three separate datasets. Each dataset was split into two – UPP1 high and UPP1 low – based on the ranked UPP1 expression value. Sample size: low = 133, high = 134 (ICGC); low = 62, high = 63 (GSE71729), low = 73, high = 73 (TCGA). TME – tumor microenvironment.

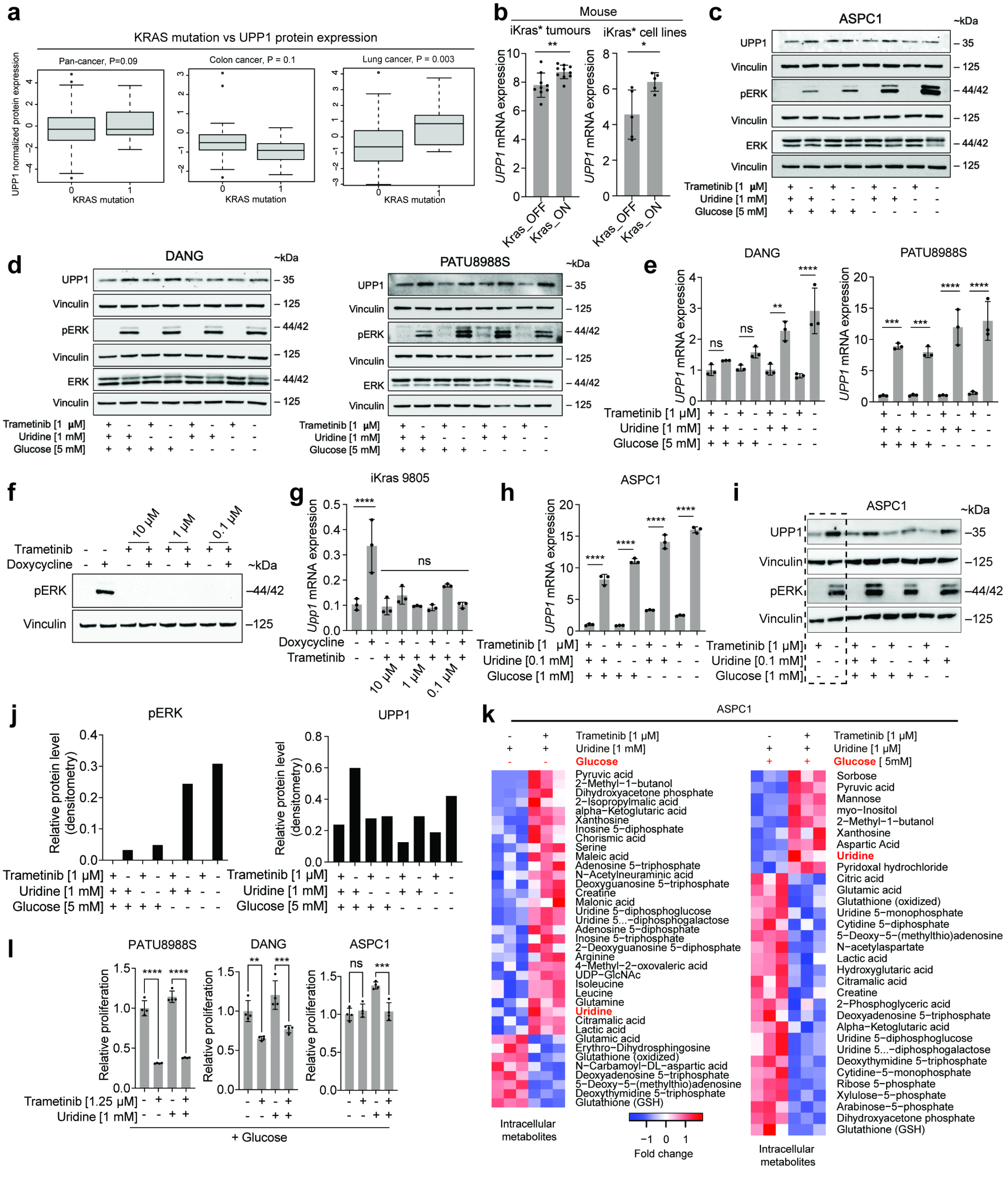

Figure 2-12 KRAS-MAPK pathway activation and nutrient availability drive UPP1 expression

a. Normalized UPP1 protein expression in Kras wildtype and mutant cell lines based on CCLE protein data accessed via the DepMap portal.

b. *Upp1* mRNA expression in iKras* orthotopic tumors and cell lines from dataset GSE32277.

c-d. Western blot showing UPP1 expression in human PDA cell lines **c**) ASPC1 cells and **d**) DANG and PATU8988S after 24 h culture +/- trametinib [MEK inhibitor], uridine, or glucose. kDa, molecular weight unit.

e. qPCR for *UPP1* in human PDA cell lines DANG and PATU8988S treated for 24 h with trametinib (1 μM), uridine (1 mM), or 5 mM glucose.

f. Western blot showing pERK upon treatment of murine iKras 9805 cells for 24 h with trametinib or doxycycline (1 μg/mL).

g. qPCR for *Upp1* in iKras* 9805 mouse PDA cells, 24 h after treatment with trametinib or doxycycline (1 μg/mL).

h. qPCR for *UPP1* in ASPC1 cells treated for 48 h with trametinib and at 0.1 mM uridine or 1 mM glucose concentrations.

i. Western blot for UPP1 and pERK treated for 48 h with trametinib and low glucose [1 mM] and near physiological uridine concentration [0.1 mM].

j. Densitometric quantification of pERK and UPP1 in the ASPC1 blots shown in **Fig. 2.3n**.

k. Metabolomics profiling showing the spectrum of metabolic changes induced in ASPC1 upon pERK inhibition with trametinib [1 μM], 24 h after culture.

l. MTT assay showing relative proliferation of PDA cell lines treated with 1.25 μM trametinib [MEK inhibitor] +/- 1 mM uridine in the presence of glucose [5 mM] at 96 h.

Statistics and Reproducibility: a. Sample size – wild type 0 and mutation 1: 304 and 69 (pan-cancer), 15 and 15 (colon cancer), 54 and 25 (lung cancer). Box plot statistics – pan-cancer (KRAS = 0: minima = -4.8237, maxima = 4.8004, median = -0.3029, 25th percentile = -1.3212, 75th percentile = 0.7687; minima = -2.1805, maxima = 3.7445, median = -0.3019, 25th percentile = -0.815, 75th percentile = 1.2867), colon (KRAS = 0: minima = -2.3253, maxima = 3.1201, median = -0.5127, 25th percentile = -0.8908, 75th percentile = -0.0958; KRAS = 1: minima = -2.1805, maxima = 0.2672, median = -0.9153, 25th percentile = -1.3926, 75th percentile = -0.5595), lung (KRAS = 0: minima = -2.7979, maxima = 4.0884, median = 0.4201, 25th percentile = -1.305, 75th percentile = 0.6032; KRAS = 1: minima = -0.9357, maxima = 3.7445, median = 0.8446, 25th percentile = -0.4923, 75th percentile = 1.3752)

b. Sample size: tumors (Kras_OFF = 9, Kras_ON = 10), cell lines (Kras_OFF = 5, Kras_ON = 5). Statistical significance was measured using two-tailed unpaired t test. Comparison of Kras_OFF to Kras_ON: **P = 0.0088 (tumors) and *P = 0.0244 (cell lines).

c-d. pERK is used as a read out for MAPK pathway induction/activity. ERK and Vinculin are used as loading controls. Blots are representative of two biological and technical replicates for ASPC1 and one biological replicate for PATU8988S and DANG with similar results.

e. n=3 biologically independent samples per group. Statistical significance was measured with one-way ANOVA with Tukey's multiple comparisons test. Comparisons between groups for DANG (from left to right): P = ns (0.9097), P = ns (0.5014), **P = 0.0025 and ****P < 0.0001. Comparisons between groups for PATU8988S (from left to right): ***P = 0.0002, ***P = 0.001, ****P < 0.0001 and ****P < 0.0001.

f. Vinculin is used as a loading control.

g. n= 3 biologically independent samples per group. Statistical significance was measured with one-way ANOVA with Dunnett's multiple comparisons test. Comparison between (-) and (+) doxycycline, ****P < 0.0001. Comparison between (-) doxycycline: vs 10 μM trametinib, P = ns (0.9997); 10 μM trametinib + doxycycline, P = ns (0.8226); 1 μM trametinib, P = ns (0.9997); 1 μM trametinib + doxycycline, P = ns (0.9994); 0.1 μM trametinib, P = ns (0.1904); 0.1 μM trametinib + doxycycline, P = ns (>0.9999).

h. n = 3 biologically independent samples per group. Statistical significance was measured with one-way ANOVA with Tukey's multiple comparisons test. Comparisons between groups (from left to right): ****P < 0.0001, ****P <

0.0001, ****P < 0.0001 and ****P < 0.0001. The experiments (e, g, h) were performed once with similar results on UPP1 displayed by the three cell lines.

i. n=3 biologically independent samples per group. This blot was run on the same gel as Fig. 2.3n hence the first two columns (separated by a box) overlap between the two blots.

j. Blots (c,i) are representative of two independent experiments; blot e experiment was done once.

k. n = 3 biologically independent samples per group. The statistical significance (P<0.05) was determined using *limma* package version 3.38.3 in R.

l. Statistical significance was measured using one-way ANOVA with Tukey's multiple comparisons test. n = 4 biologically independent samples per group. PATU8988S (comparison between cells cultured with and without trametinib in the absence of uridine: ****P < 0.0001, and with uridine supplementation: ****P < 0.0001); DANG (comparison between cells cultured with and without trametinib in the absence of uridine: **P = 0.0055, and with uridine supplementation: ***P = 0.0009); ASPC1 (comparison between cells cultured with and without trametinib in the absence of uridine: P = not significant, and with uridine supplementation: ****P = 0.0006). Data (b, e, g-h, l) shown as mean ± s.d.

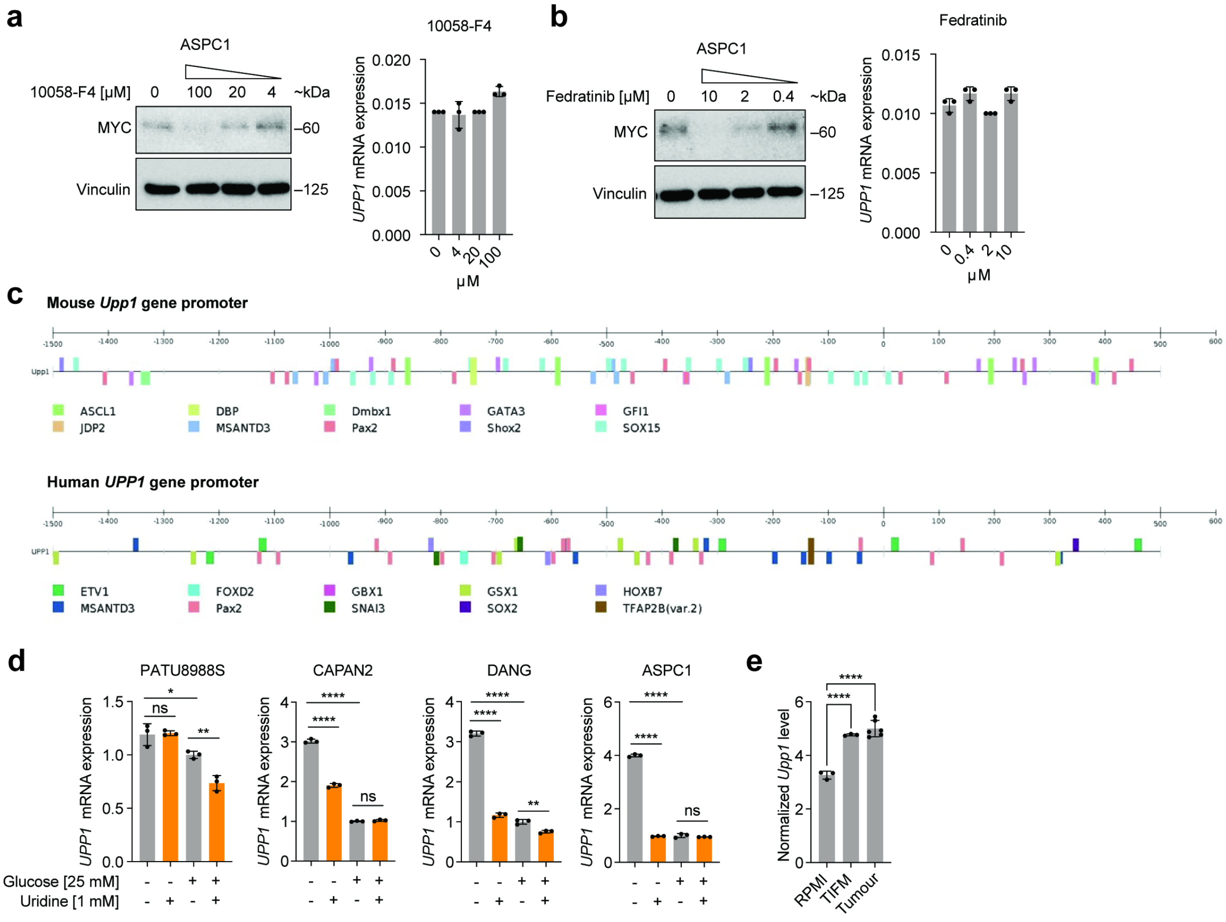

Figure 2-13 Regulation of *UPP1* expression is independent of c-MYC

a. Western blot showing Myc inhibition by 10058-F4 in ASPC1 cells after 24 h of culture. On the right: *UPP1* mRNA expression determined by qPCR. kDa, molecular weight unit.

b. Western blot of Myc inhibition by Fedratinib in ASPC1 cells after 24 h of culture. On the right: *UPP1* mRNA expression determined by qPCR.

c. CiiDER analysis of transcription factor binding sites in the promoters of mouse and human UPP1. Myc binding sites were not detected. Details of analysis is in the "Methods" section.

d. qPCR showing *UPP1* expression upon uridine supplementation with or without basal glucose concentration in culture media.

e. RNA seq data showing the expression of Upp1 in sorted tumor cells and in KPC cells cultured in vitro in regular RPMI culture media or tumor interstitial fluid media (TIFM). Sample sizes: Tumor, n = 6, RPMI, n = 3 biologically independent cell samples, TIFM, n = 3 biologically independent cell samples. Normalized by log transformation [log2 (count +1)]. Statistical significance was measured using one-way ANOVA with Dunnett's multiple comparisons test. Comparison between RPMI and TIFM group, ****P < 0.0001 or tumor group, ****P < 0.0001. **Statistics and Reproducibility: a,** qPCR, n = 3 biologically independent samples per group.

b. n = 3 biologically independent samples per group. Blots shown (a-b) are representative of two biological and technical replicate analyses with similar results.

d. n = 3 biologically independent samples per group per cell line. Statistical significance was measured using one-way ANOVA with Tukey's multiple comparisons test. PATU8988S (comparison between no glucose and no glucose + 1 mM uridine: P = ns (0.994); comparison between cells cultured in glucose-containing media with and without uridine: **P = 0.005; comparison between no glucose and glucose: *P = 0.0316; CAPAN2 (comparison between no glucose and no glucose + 1 mM uridine: ****P < 0.0001; comparison between cells cultured in glucose-containing media with and without uridine: P = ns (0.8688); DANG (comparison between no glucose and no glucose + 1 mM uridine: ****P < 0.0001; comparison between cells cultured in glucose-containing media with and without uridine: **P = 0.0021); ASPC1 (comparison between no glucose and no glucose + 1 mM uridine: ****P < 0.0001; comparison between cells cultured in glucose-containing media with and without uridine: P = ns (0.5339). Comparison between no glucose and glucose for CAPAN2, DANG and ASPC1: ****P < 0.0001. Data (a, b, d, e) shown as mean ± s.d.

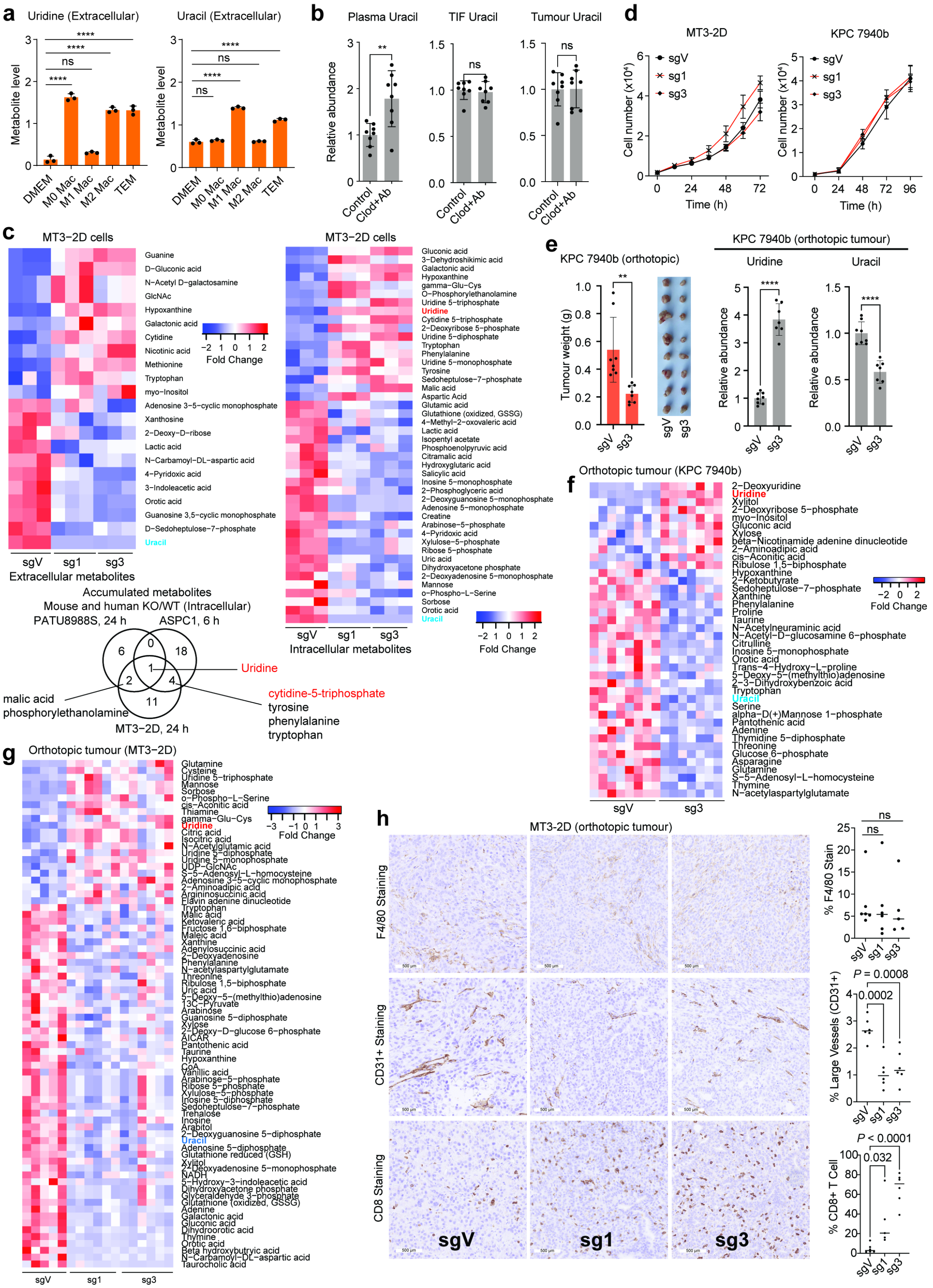

Figure 2-14. Knockout of UPP1 suppresses *in vivo* uridine catabolism and tumor growth

a. LC-MS analysis of extracellular uridine and uracil in unpolarized bone marrow-derived macrophages (M0; 10ng/mL M-CSF), those polarized toward an M1 fate (10 ng/mL LPS), an M2 fate (10 ng/mL murine IL-4), or a tumor-educated (TEM) phenotype with 75% PDA conditioned media and compared to growth media (DMEM). n = 3 biologically independent samples per group. Data was extracted from a previously published metabolomics[14].

b. Relative uracil abundance in plasma, tumor interstitial fluid (TIF), and bulk tumor from the experiment described in Fig. 2.4a, where Clod. + Ab indicates the macrophage-depleted group.

c. Extracellular (left) and intracellular (right) profiles of significantly changed ($P < 0.05$) metabolites from sgV and UPP1-KO (sg1, sg3) MT3-2D cells. The cells were cultured in media with 1 mM uridine and no glucose for 24 h, as determined by metabolomics.

d. Proliferation assay of sgVector (sgV) and UPP1-KO (sg1, sg3) MT3-2D and KPC 7940b mouse PDA cell lines cultured over 72h and 96h, respectively, in normal growth media with 10% dialyzed FBS.

e. Tumor weight and image, and bulk tumor uridine and uracil from the orthotopic implantation of sgV and UPP1 KO (sg3) KPC 7940b cell lines into C57BL/6J mice; see Fig 4i for experimental details.

f,g. Tumor metabolomics profile indicating statistically significant ($P < 0.05$) metabolites from sgV and UPP1 KO **f**) KPC 7940b and **g**) MT3-2D-derived tumors.

h. Immunohistochemistry (IHC) staining of macrophages (F4/80), large blood vessels (CD31+), and cytotoxic cells (CD8) using tissue sections of MT3-2D orthotopic tumors. Micrographs are representative of 10 fields per image obtained per experiment group. Scale bar 500 µm. On the right are the respective quantifications of the IHC stains.

Statistics and Reproducibility: a. Statistical significance was measured using one-way ANOVA and Dunnett's multiple comparisons test. Uridine – DMEM: comparison to M0 Mac group ****$P < 0.0001$; to M1 Mac group P = ns (0.0758); to M2 Mac group ****$P<0.0001$; to TEM group ****$P<0.0001$. Uracil – DMEM: comparison to M0 Mac P = ns (0.5476); to M1 Mac group ****$P < 0.0001$; to M2 Mac group P = ns (0.9894); to TEM group ****$P < 0.0001$.

b. Statistical significance was measured using a two-tailed unpaired t-test – Plasma uracil **$P = 0.0045$ with n = 8 biologically independent replicates in both groups, TIF uracil P = ns (0.6872) with n = 8 biologically independent replicates in both groups – and using Welch's t-test P=ns (0.9682) with n = 8 biologically independent replicates in both groups.

c. n = 3 biologically independent samples per group. Color scale denotes fold change. Below: Venn diagram showing overlapping metabolites that accumulated in both human (PATU8988S and ASPC1) and mouse (MT3-2D) cell lines upon UPP1 knockout.

d. MT3-2D, n = 4 and KPC 7940b, n = 3 biologically independent samples per group.

e. n = 8 biologically independent samples per group. Statistical significance measured using two-tailed unpaired t-test with Welch's correction, **$P = 0.0059$. On the right: bulk tumor uridine and uracil as measured using metabolomics. Sample size: sgV = 8, sg3 = 7. Uridine: ****$P < 0.0001$. Uracil: ****$P < 0.0001$.

f,g. Sample size: KPC 7940b sgV = 8 and sg3 = 7, MT3-2D sgV = 5 sg1 = 6 and sg3 = 6 biologically independent samples from mice with orthotopic pancreatic tumors.

h. Sample size: F4/80 sgV = 7, sg1 = 6, sg3 = 5; CD31 n = 6; CD8+ sgV = 6, sg1 = 5, sg3 = 6, all biologically independent samples per group. Statistical significance was measured using one-way ANOVA with Dunnett's multiple comparisons test. Comparison between % F4/80 sgV and sg1 P = ns (>0.9968), and sgV and sg3 P = ns (0.9583). Data (a, b, d, e) shown as mean ± s.d; horizontal bars in h represent mean value.

Chapter 3 Nitrogen Profiling in Pancreatic Cancer

3.1 Introduction

Pancreatic Ductal Adenocarcinoma (PDA) exists in a highly dense, fibrotic, and metabolically deregulated tumor microenvironment[1]. This heterogenous environment is composed of fibroblasts, extracellular matrix, and various immune cell populations. Due to the dense, fibrotic nature of the TME, there is inefficient vasculature, causing a hypoxic environment and lack of serum-derived nutrients[1,2]. Within this environment, PDA can alter its metabolism to survive in these harsh conditions[3,4]. In lieu of blood-derived nutrients, PDA relies on other carbon and nitrogen sources to fuel metabolism. These can be derived from the TME by cellular crosstalk mechanisms or nutrient scavenging mechanisms such as autophagy[1,3,5].

To comprehensively profile which nutrients are capable of rescuing PDA metabolism, we employed a large-scale phenotyping assay in which we screened 20 PDA cell lines in various media conditions[6-8]. The Biolog phenotyping utilizes a proprietary tetrazolium salt which is reduced by cellular reductases to create a purple formazan dye, which can be quantified to indicate mitochondrial NADH reduction. Cells are cultured in various media conditions and plated on a 96-well plate, with each well containing a single dried metabolite. By culturing cells in these individual metabolites and adding the Biolog reagents, we can observe the intensity of the purple dye produced across time to measure relative metabolic activity via the mitochondria[6,7]. Through this screen we profiled 20 PDA cell lines in 14 different metabolic assay plates which included carbon and nitrogen sources, a panel of ions, metabolic effectors, and chemotherapy drugs. Thus far, we have utilized the data from the carbon sourced assays to identify uridine as an alternative fuel source for PDA[8], as described in **Chapter 2**. This chapter dives back into the Biolog assay to assess the effect of nitrogen sources on PDA metabolism.

3.2 Results

To assess the effect of nitrogen containing metabolites on PDA metabolism three metabolic plates (PM-M2, PM-M3, PM-M4) were used (**Table 3-1 – 3-3**). These plates consisted of nitrogen-containing amino acids and dipeptides, along with positive (glucose) and negative controls. Cells were cultured in glucose and glutamine-free media supplemented with 2mM galactose, 0.3 mM glutamine, 5% dialyzed fetal bovine serum (dFBS), and 1x penicillin streptomycin solution. This depleted media maintains cell survival with low levels of glutamine and pushes cells to an oxidative state by supplementing the energetically unfavorable substrate galactose, allowing us to attribute metabolic rescue to the individual substrate provided[9]. Cells were plated at 20,000 cells per well onto phenotyping plates and incubated for 24 hours, allowing cells to consume any remaining carbon from the FBS and reduce background. After 24 hours 10 uL of 6-fold concentrated Redox Dye Mix MB was added to each well. Plates were further incubated for 72 hours and photographed at 15-minute intervals to assess redox dye as a metric of metabolic activity (**Fig. 3-1a**).

The absorbance data for each time point was recorded for each substrate (well) and exported to .csv files for each cell line. Using the statistical programming language R, each data was imported and collated into a single data frame with variables including cell line, assay plate, time, substrate, absorbance (MTT). From these data, for each substrate across 72 hours, a local polynomial regression line of fit was derived and used to calculate the first derivative of the metabolic activity based on absorbance values across time (**Fig. 3-1a,b**). Through this the slope or rate of consumption of a metabolite was derived. Additionally, the fitted model allowed for integration of the area under the curve (AUC) to calculate total consumption of a metabolite over the length of the assay. From these three important metrics of metabolic activity were generated: catabolic rate (slope), total metabolite catabolism (AUC), and maximum catabolic efficiency (maximum height) (**Fig. 3-1a**). Downstream analysis was based off catabolic rate, as this metric was the most dynamic of the three.

Due to the nature of the consumption assays being a logarithmic distribution, the maximum slope of a metabolite indicated quick and effective metabolic rescue. When plotting the maximum slopes for each substrate across all cell lines we can see a wide array of nitrogen-containing metabolites are capable of rescuing PDA metabolism (**Fig. 3-2a**). Across all three plates glutamine containing dipeptides rescued metabolic activity (**Fig. 3-2a,b**). This was expected, as glutamine provides an essential source of carbon and nitrogen in the cell[10]. In addition, PDA cells rely on glutamine to fuel the TCA cycle and generate mitochondrial ATP[10,11]. The data was subsetted to observe only glutamine-containing metabolites and maximum catabolic rates were plotted and ordered (**Fig. 3-3**). The fastest consumed dipeptides were isoleucine-glutamine and glutamine-glutamine, while the slowest were glutamine-glutamate and aspartate-glutamate.

3.3 Discussion

The PDA tumor microenvironment is a nutrient dysregulated environment in which cancer cells must adapt and utilize non-classical nutrients to survive[1,3]. Understanding the nutrient sources capable of fueling PDA cells is an important step in furthering our knowledge of this deadly disease and developing new targeted therapy opportunities. Through the Biolog phenotyping assay we profiled 20 different pancreatic cell lines and studied the ability for nitrogen sources to rescue metabolic activity under nutrient-deplete conditions. In these analyses

I utilized the maximum catabolic rate of a substrate as an indicator for the top metabolites able to be readily utilized by PDA cells. From these studies we determined glutamine to be an effective rescue of PDA metabolism.

Glutamine is well characterized to be utilized by PDA to support proliferation through the generation of mitochondrial ATP in the TCA cycle. Additionally, glutamine is an essential source of nitrogen within the cell for many biochemical processes including nucleotide and amino acids synthesis[10,11]. Given that glutamine is the most abundant non-essential amino acid in circulation in the body, it is not surprising that it is quickly and readily consumed by PDA cells to rescue metabolism in nutrient-deplete conditions. An observation of note from these studies is that while all glutamine dipeptides are highly catabolized by PDA, glutamine-glutamate is among the slowest (**Fig. 3-3**). This finding was surprising for a multitude of reasons. First, the cells are cultured in nutrient-depleted conditions and supplemented with galactose to sustain basal metabolism. Galactose is an energetically unfavorable substrate, as it must be converted into glucose 1-phosphate before entering glycolysis. Culturing cells in galactose results in an oxidative phenotype, forcing the cells to prefer mitochondrial respiration, or oxidative phosphorylation (OXPHOS)[9,12]. Second, for glutamine to be utilized in the TCA cycle it must first be deaminated to glutamate, and then further deaminated to alpha-ketoglutarate (aKG). Given that the screened cells are primed for OXPHOS via galactose culture, and are then provided glutamine dipeptides, it is reasonable to conclude that the glutamine-glutamate dipeptide should be more readily consumed than the glutamine-glutamine substrate, as glutamate is downstream of glutamine and needs only to be deaminated a single time.

These conclusions are predicated on the findings that PDA relies on glutamine-derived carbon to fuel OXPHOS. However, an area of further study would be the fate of the carbon and nitrogen within the glutamine-glutamate dipeptide. These findings indicate that while both dipeptides contain carbons capable of fueling OXPHOS, the role of nitrogen may be more important in rescuing PDA metabolism, as the glutamine-glutamine dipeptide contains more nitrogens and is more readily consumed. Additionally, the enzymatic expression and energies needed to catabolize the dipeptide bonds for the respective substrates may indicate the rate of catabolism by PDA cells, as well.

Overall, there exists a wide array of nitrogen-containing substrates that have been shown to be capable of rescuing PDA metabolism under nutrient-deplete conditions. Given PDA's profound ability to adapt to its TME and catabolize a wide range of substrates, these nitrogen sources present a unique potential therapeutic opportunity and warrant future study. From these studies we find that glutamine-containing dipeptides are most readily consumed by PDA cells. However, there is a broad spectrum of efficiency in catabolism depending on the composition of the dipeptides, which present exciting future directions in identifying the underlying mechanisms for PDA catabolism of dipeptides.

3.4 Methods

Biolog Metabolic Assay.

In the initial phenotypic screen, the 22 cell lines were grown in 96-well PM-M2, PM-M3, and PM-M4 plates. The assay was set up such that one well was used per test metabolite substrate, accompanied by three replicates of positive (glucose) and negative (blank) controls wells. The relative metabolic activity (RMA) from substrate catabolism in the cells was measured using Biolog Redox Dye Mix MB. Briefly, the cell lines were counted, and their viability assessed using Trypan Blue Dye (Invitrogen, # T10282). The cells were then washed 2x with Biolog Inoculating fluid IF-M1 (Biolog, # 72301) to remove residual culture media. Then, a cell suspension containing 20,000 cells per 50 µL was prepared in Biolog IF-M1 containing 0.3 mM glutamine and 5% dialyzed FBS (dFBS) (Hyclone GE Life Sciences, # SH30079.01) and plated into PM-M2, PM-M3 and PM-M4 96-well plates at 50 µL per well. Plates were incubated for 24 hours at 37°C and 5% CO_2, after which 10 µL Biolog Redox Dye Mix MB (Biolog, # 74352) was added to each well. Plates were sealed to prevent the leakage of CO_2. The reduction of the dye over time was measured as absorbance (A590-A750) using the OmniLog PM-M instrument (Biolog, # 93171) for 74.5 hours at 15 minutes interval. To account for proliferation/cell number in the Biolog screening assay, CyQUANT was used for normalization.

The data was processed using the R statistical programming tool utilizing packages *readr, tidyverse, dplyr, gplots* and *ggplot2*. Data was obtained from Biolog as .csv files for each individual cell line. Cell lines *Tu8988T* and *Panc1* were removed from analyses for missingness. Files were imported and stored in a data frame. Each substrate per cell line has absorbance values recorded across 72 hours. From these a predicted model was generated via loess(absorbance ~ time). From these an AUC was generated to measure total metabolite catabolism, first derivative slopes were generated to measure catabolic rate, and maximum height was generated to measure maximum catabolic efficiency.

Maximum slopes were plotted for each substrate across all cell lines on a heatmap via *gplots*. Data was then subsetted to combine all three plates and extract glutamine-containing substrates. Distribution of maximum slopes were plotted on a box plot and facet wrapped for cell line for glutamine-containing substrates via *ggplot2*.

3.5 References

1. Ho, W. J., Jaffee, E. M. & Zheng, L. The tumour microenvironment in pancreatic cancer — clinical challenges and opportunities. *Nature Reviews Clinical Oncology 2020 17:9* **17**, 527–540 (2020).

2. Halbrook, C. J., Lyssiotis, C. A., Pasca di Magliano, M. & Maitra, A. Pancreatic cancer: Advances and challenges. *Cell* **186**, 1729–1754 (2023).

3. Lyssiotis, C. A., Kimmelman, A. C., Lyssiotis, C. A., Org, A. K. & Kimmelman, A. C. Metabolic Interactions in the Tumor Microenvironment. *Trends Cell Biol* **27**, 863–875 (2017).

4. Halbrook, C. J. & Lyssiotis, C. A. Employing Metabolism to Improve the Diagnosis and Treatment of Pancreatic Cancer. *Cancer Cell* **31**, 5–19 (2017).

5. Yang, S. *et al.* Pancreatic cancers require autophagy for tumor growth. *Genes Dev* **25**, 717–729 (2011).

6. Bochner, B. R. *et al.* Assay of the Multiple Energy-Producing Pathways of Mammalian Cells. *PLoS One* **6**, e18147 (2011).

7. Bochner, B. R., Gadzinski, P. & Panomitros, E. Phenotype MicroArrays for High-Throughput Phenotypic Testing and Assay of Gene Function. *Genome Res* **11**, 1246 (2001).

8. Nwosu, Z. C. *et al.* Uridine-derived ribose fuels glucose-restricted pancreatic cancer. *Nature 2023 618:7963* **618**, 151–158 (2023).

9. Gohil, V. M. *et al.* Nutrient-sensitized screening for drugs that shift energy metabolism from mitochondrial respiration to glycolysis. *Nat Biotechnol* **28**, 249–255 (2010).

10. Son, J. *et al.* Glutamine supports pancreatic cancer growth through a KRAS-regulated metabolic pathway. *Nature* **496**, 101–105 (2013).

11. Lyssiotis, C. A., Son, J., Cantley, L. C. & Kimmelman, A. C. Pancreatic cancers rely on a novel glutamine metabolism pathway to maintain redox balance. *Cell Cycle* **12**, 1987–1988 (2013).

12. Orlicka-Płocka, M., Gurda-Wozna, D., Fedoruk-Wyszomirska, A. & Wyszko, E. Circumventing the Crabtree effect: forcing oxidative phosphorylation (OXPHOS) via galactose medium increases sensitivity of HepG2 cells to the purine derivative kinetin riboside. *Apoptosis* **25**, 835 (2020).

3.6 Figures

A01_Negative Control	C01_L-Methionine	E01_Ala-Pro	G01_Asp-Glu
A02_Negative Control	C02_L-Ornithine	E02_Ala-Ser	G02_Asp-Gln
A03_Negative Control	C03_L-Phenylalanine	E03_Ala-Thr	G03_Asp-Gly
A04_Tween 20	C04_L-Proline	E04_Ala-Trp	G04_Asp-Leu
A05_Tween 40	C05_L-Serine	E05_Ala-Tyr	G05_Asp-Lys
A06_Tween 80	C06_D-Serine	E06_Ala-Val	G06_Asp-Phe
A07_Gelatin	C07_L-Threonine	E07_Arg-Ala Acetate	G07_Asp-Trp
A08_L-Alaninamide	C08_D-Threonine	E08_Arg-Arg Acetate	G08_Asp-Val
A09_L-Alanine	C09_L-Tryptophan	E09_Arg-Asp	G09_Glu-Ala
A10_D-Alanine	C10_L-Tyrosine	E10_Arg-Gln	G10_Glu-Asp
A11_L-Arginine	C11_L-Valine	E11_Arg-Glu	G11_Glu-Glu
A12_L-Asparagine	C12_Ala-Ala	E12_Arg-Ile Acetate	G12_Glu-Gly
B01_L-Aspartic acid	D01_Ala-Arg	F01_Arg-Leu Acetate	H01_Glu-Ser
B02_D-Aspartic acid	D02_Ala-Asn	F02_Arg-Lys Acetate	H02_Glu-Trp
B03_L-Glutamic acid	D03_Ala-Asp	F03_Arg-Met Acetate	H03_Glu-Tyr
B04_D-Glutamic acid	D04_Ala-Glu	F04_Arg-Phe Acetate	H04_Glu-Val
B05_L-Glutamine	D05_Ala-Gln	F05_Arg-Ser Acetate	H05_Gln-Glu
B06_Glycine Hydrochloride	D06_Ala-Gly	F06_Arg-Trp	H06_Gln-Gln
B07_L-Histidine	D07_Ala-His	F07_Arg-Tyr Acetate	H07_Gln-Gly
B08_L-Homoserine	D08_Ala-Ile	F08_Arg-Val Acetate	H08_Gly-Ala
B09_trans-4-Hydroxy-L-Proline	D09_Ala-Leu	F09_Asn-Glu	H09_Gly-Arg
B10_L-Isoleucine	D10_Ala-Lys	F10_Asn-Val	H10_Gly-Asn
B11_L-Leucine	D11_Ala-Met	F11_Asp-Ala	H11_Gly-Asp
B12_L-Lysine	D12_Ala-Phe	F12_Asp-Asp	H12_a-D-Glucose

Table 3-1 Substrates included in the Biolog PM-M2 plate.

The substrates from a 96-well plate are listed, with each well being represented as a matrix with letters A through H and numbers 1 through 12. Substrates are listed by well position and are adhered to the well in amounts ranging from 1-12mM.

A01_Negative Control
A02_Negative Control
A03_Negative Control
A04_Gly-Gly
A05_Gly-His
A06_Gly-Ile
A07_Gly-Leu
A08_Gly-Lys
A09_Gly-Met
A10_Gly-Phe
A11_Gly-Pro
A12_Gly-Ser
B01_Gly-Thr
B02_Gly-Trp
B03_Gly-Tyr
B04_Gly-Val
B05_His-Ala
B06_His-Asp
B07_His-Glu
B08_His-Gly
B09_His-His Trifluoroacetate
B10_His-Leu
B11_His-Lys Bromide
B12_His-Met
C01_His-Pro
C02_His-Ser
C03_His-Trp
C04_His-Tyr
C05_His-Val
C06_Ile-Ala
C07_Ile-Arg Acetate
C08_Ile-Asn
C09_Ile-Gln
C10_Ile-Gly
C11_Ile-His
C12_Ile-Ile
D01_Ile-Leu
D02_Ile-Met
D03_Ile-Phe
D04_Ile-Pro
D05_Ile-Ser
D06_Ile-Trp
D07_Ile-Tyr
D08_Ile-Val
D09_Leu-Ala
D10_Leu-Arg Acetate
D11_Leu-Asn
D12_Leu-Asp
E01_Leu-Glu
E02_Leu-Gly
E03_Leu-His
E04_Leu-Ile
E05_Leu-Leu
E06_Leu-Met
E07_Leu-Phe
E08_Leu-Pro
E09_Leu-Ser
E10_Leu-Trp
E11_Leu-Tyr
E12_Leu-Val
F01_Lys-Ala Bromide
F02_Lys-Arg Acetate
F03_Lys-Asp
F04_Lys-Glu
F05_Lys-Gly
F06_Lys-Ile Acetate
F07_Lys-Leu Acetate
F08_Lys-Lys
F09_Lys-Met Formate
F10_Lys-Phe
F11_Lys-Pro
F12_Lys-Ser
G01_Lys-Thr
G02_Lys-Trp Acetate
G03_Lys-Tyr Acetate
G04_Lys-Val Bromide
G05_Met-Arg Acetate
G06_Met-Asp
G07_Met-Gln
G08_Met-Glu
G09_Met-Gly
G10_Met-His
G11_Met-Ile
G12_Met-Leu
H01_Met-Lys Formate
H02_Met-Met
H03_Met-Phe
H04_Met-Pro
H05_Met-Thr
H06_Met-Trp
H07_Met-Tyr
H08_Met-Val
H09_Phe-Ala
H10_Phe-Asp
H11_Phe-Glu
H12_a-D-Glucose

Table 3-2 Substrates included in the Biolog PM-M3 plate.

The substrates from a 96-well plate are listed, with each well being represented as a matrix with letters A through H and numbers 1 through 12. Substrates are listed by well position and are adhered to the well in amounts ranging from 1-12mM.

A01_Negative Control
A02_Negative Control
A03_Negative Control
A04_Phe-Gly
A05_Phe-Ile
A06_Phe-Met
A07_Phe-Phe
A08_Phe-Pro
A09_Phe-Ser
A10_Phe-Trp
A11_Phe-Tyr
A12_Phe-Val
B01_Pro-Ala
B02_Pro-Arg Acetate
B03_Pro-Asn
B04_Pro-Asp
B05_Pro-Glu
B06_Pro-Gln
B07_Pro-Gly
B08_Pro-Hyp
B09_Pro-Ile
B10_Pro-Leu
B11_Pro-Lys Acetate
B12_Pro-Phe
C01_Pro-Pro
C02_Pro-Ser
C03_Pro-Trp
C04_Pro-Tyr
C05_Pro-Val
C06_Ser-Ala
C07_Ser-Asn
C08_Ser-Asp
C09_Ser-Glu
C10_Ser-Gln
C11_Ser-Gly
C12_Ser-His Acetate
D01_Ser-Leu
D02_Ser-Met
D03_Ser-Phe
D04_Ser-Pro
D05_Ser-Ser
D06_Ser-Tyr
D07_Ser-Val
D08_Thr-Ala
D09_Thr-Arg Sulfate
D10_Thr-Asp
D11_Thr-Glu
D12_Thr-Gln
E01_Thr-Gly
E02_Thr-Leu
E03_Thr-Met
E04_Thr-Phe
E05_Thr-Pro
E06_Thr-Ser
E07_Trp-Ala
E08_Trp-Arg
E09_Trp-Asp
E10_Trp-Glu
E11_Trp-Gly
E12_Trp-Leu
F01_Trp-Lys Formate
F02_Trp-Phe
F03_Trp-Ser
F04_Trp-Trp
F05_Trp-Tyr
F06_Trp-Val
F07_Tyr-Ala
F08_Tyr-Gln
F09_Tyr-Glu
F10_Tyr-Gly
F11_Tyr-His
F12_Tyr-Ile
G01_Tyr-Leu
G02_Tyr-Lys
G03_Tyr-Phe
G04_Tyr-Trp
G05_Tyr-Tyr
G06_Tyr-Val
G07_Val-Ala
G08_Val-Arg
G09_Val-Asn
G10_Val-Asp
G11_Val-Glu
G12_Val-Gln
H01_Val-Gly
H02_Val-His
H03_Val-Ile
H04_Val-Leu
H05_Val-Lys
H06_Val-Met
H07_Val-Phe
H08_Val-Pro
H09_Val-Ser
H10_Val-Tyr
H11_Val-Val
H12_a-D-Glucose

Table 3-3 Substrates included in the Biolog PM-M4 plate.

The substrates from a 96-well plate are listed, with each well being represented as a matrix with letters A through H and numbers 1 through 12. Substrates are listed by well position and are adhered to the well in amounts ranging from 1-12mM.

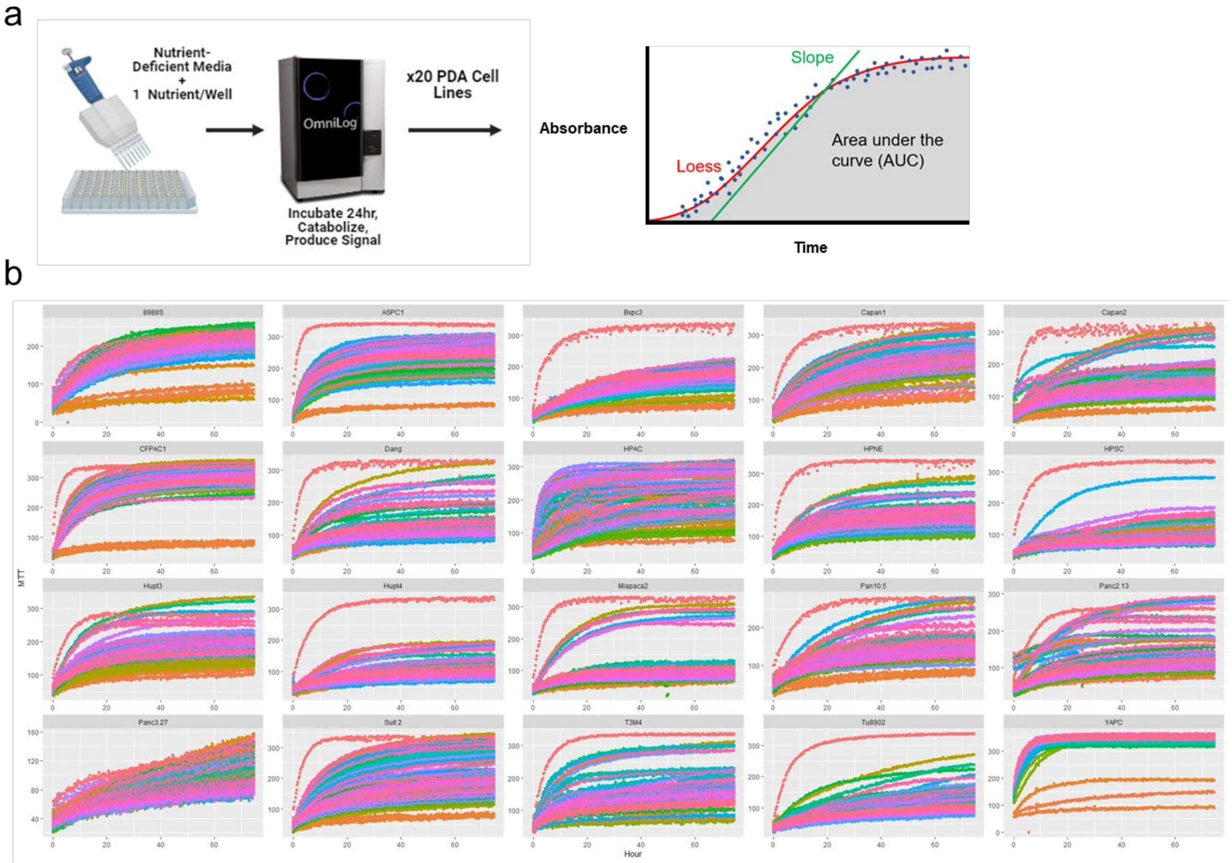

Figure 3-1 Nitrogen-containing substrates rescue metabolic activity in PDA cell lines

a. Schematic of Biolog phenotyping assay utilizing 20 different PDA cell lines in nutrient-deficient media. Nitrogen-containing metabolites are added to individual wells. Graph depicts parameters for data analysis, where absorbance is registered on the y-axis (blue dots), line of fit (loess), area under the curve (AUC), and slope are observed across time on the x-axis.

b. Representative absorbance plots for each cell line where absorbance is recorded as the y-axis and time is the x-axis. Each color represents a nitrogen-containing substrate from the Biolog assay plate. Each plot is a different PDA cell line. Plate 2 is depicted, while plates 3 and 4 are not shown.

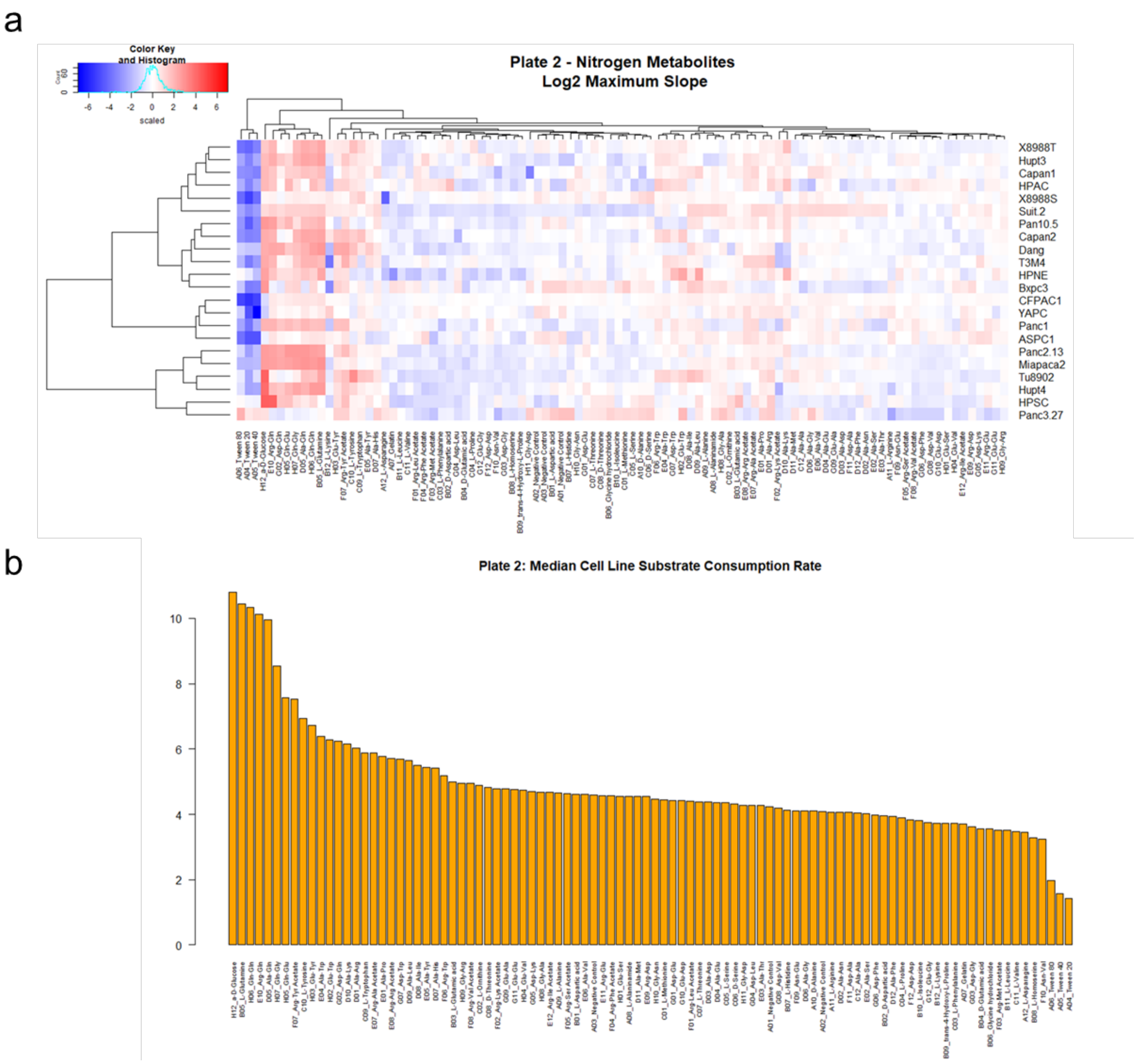

Figure 3-2 Maximum slopes indicate highly catabolic substrates in PDA.

a. Heatmap of maximum catabolic rate of each substrate from PM-M2. Rows represent cell lines, while columns represent substrates in the 96-well plate. Log2 maximum slope is plotted. Plate 2 is shown, while plates 3 and 4 are not shown.

b. Ranked bar plot for average maximum catabolic rate across all cell lines for each substrate. Plate 2 is shown, while plates 3 and 4 are not shown.

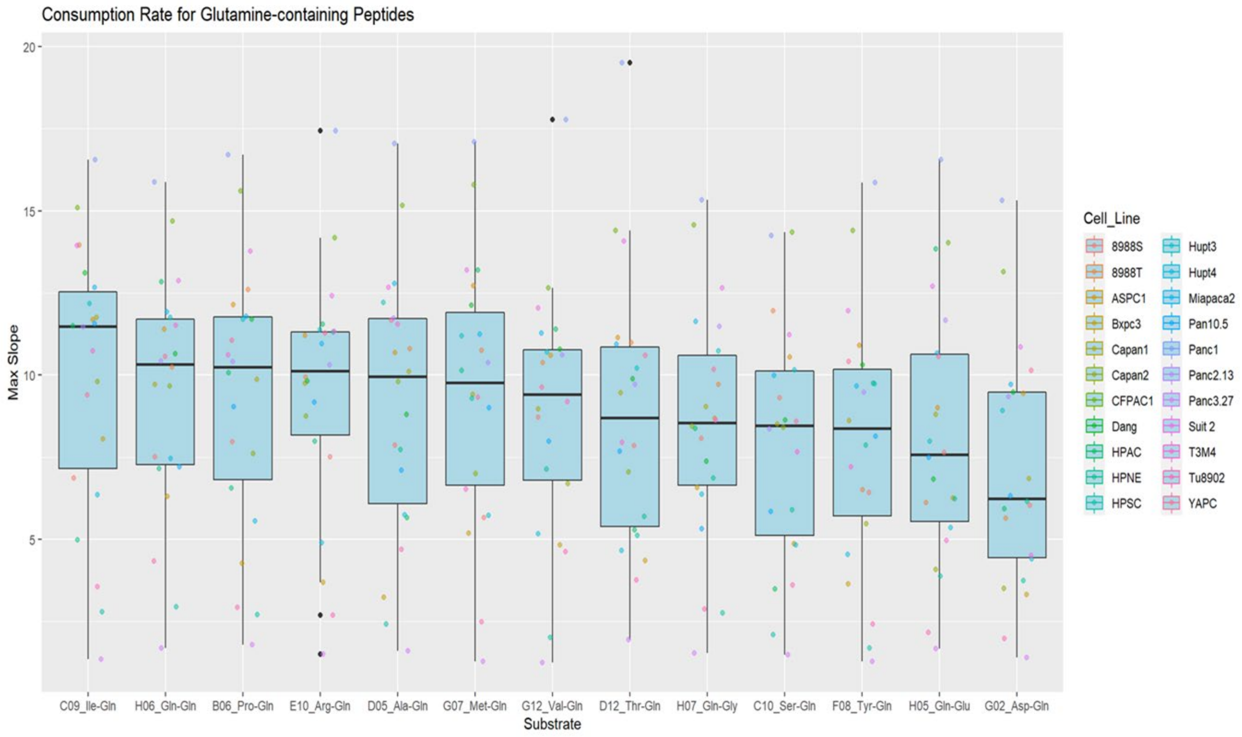

Figure 3-3 Composition of glutamine-containing peptides decide catabolic rate of consumption.

Ranked boxplots depicting the distribution of maximum slopes in glutamine-containing peptides across all three plates. Colored dots represent each cell line.

Chapter 4 Future Directions and Conclusion

4.1 Future Directions

The work presented here contributes to the growing field of cancer metabolism which has recently been deemed a hallmark of cancer[1]. Understanding the ways in which cancer cells adapt to their specific microenvironments is key in not only developing targeted therapies but improving model systems in the laboratory. By fully understanding the inner workings of the tumor microenvironment we can better model experiments in vitro to reflect these conditions. The large-scale Biolog phenotyping assay performed in this work across a wide array of PDA cell lines aims to comprehensively profile the nutrient inputs capable of sustaining cancer cells. Through the work in **Chapter 2** we identified uridine as a significant energy source for PDA metabolism through the enzyme UPP1[2]. By inhibiting UPP1 we achieved significant tumor reduction *in vivo*, indicating uridine to play a significant role in PDA metabolism. This chapter addresses future areas of study building off these findings.

UPP1 as a therapeutic target

In **Chapter 2** our findings demonstrated knockout of UPP1 reduced tumor burden in syngeneic mouse models. These findings present UPP1 as a potential therapeutic target. Our studies thus far have targeted UPP1 via genetic knockout, and modulation of expression via MAPK inhibition and nutrient deprivation. Inhibition of UPP1 by pharmacological means is the most translational approach and should be studied more extensively. The synthetic compound potassium 5-cyano-4-methyl-6-oxo-1,6-dihydropyridine-2-olate (CPBMF65) has been shown to be a potent inhibitor of UPP1[3]. In liver fibrosis studies CPBMF65 treatment showed reduced proliferation in hepatic stellate cells independent of apoptosis or senescence[4]. Contrastingly, in hepatocellular carcinoma (HCC) cells (HepG2), use of CPBMF65 to inhibit UPP1 resulted in reduction of cell proliferation through cell cycle arrest and senescence[3]. Together, these studies indicate that UPP1 inhibitors may be viable options to reduce cell proliferation. These studies reasoned that the accumulation of intracellular uridine caused by inhibiting UPP1 provides a protective effect by inhibition of inflammation and fibrosis. The reduction of cell proliferation upon UPP1 inhibition aligns well with our findings in PDA and indicates a promising avenue for future therapeutic studies.

Furthermore, the use of CPBMF65 could be a good combination therapy candidate in conjunction with the chemotherapy drug 5-fluorouracil (5-FU)[5]. 5-FU inhibits DNA replication and RNA synthesis by competing as an agonist and being incorporated in processes in place of uracil, ultimately leading to cell death. It has been shown to be an effective chemotherapy regimen and is included in the standard of care for PDA in the combination treatment FOLFIRINOX. These treatments result in significant side effects, yet preliminary studies have shown promise that CPBMF65 treatment in combination with 5-FU may reduce toxicity without impairing anti-tumoral activity. The potential for pharmacological UPP1 inhibition in combination with PDA chemotherapy regimens seem promising in both relieving side effects and providing synergistic response in anti-tumoral effects.

UPP1 and its role in metastasis

When implanting UPP1 knockout cells in immunocompetent mice we saw a significant reduction in tumor size[2]. However, when using human cell lines implanted in immunocompromised mice, we did not observe a significant change to tumor burden. Interestingly, we observed an increase in liver metastasis in these immunocompromised mice that was decreased upon UPP1 knockout[2]. We saw no difference in metastasis in the immunocompetent cohorts. In human PDA, the liver is the most common metastatic site followed by the lung[6]. Metastasis occurs through a series of events referred to as the metastatic cascade, which broadly include: invasion and migration from the primary tumor to the basement membrane, intravasation into the vasculature, survival and circulation in the bloodstream, extravasation through the endothelial barrier into the metastatic site, and colonization in the target organ[6,7]. An important process to begin this cascade is epithelial to mesenchymal transition (EMT), a process that results in adherent epithelial cells losing their E-cadherin (CDH1) anchorage and transitioning into a more motile mesenchymal phenotype[8]. Recent studies have characterized two major subtypes of PDA: classical, representing an epithelial phenotype, and basal, representing a mesenchymal phenotype, with the latter presenting significantly worse patient prognosis[8,9]. Our immunocompromised mouse models may indicate a relationship between UPP1 and metastasis, with the former potentially being used to help metastatic tumors obtain nutrients at a greater rate. Additionally, from publicly available datasets we observed UPP1 to be highly expressed in liver metastatic tumors. Together, these findings warrant further study into how UPP1 affects the EMT process and its association with different PDA subtypes. Given that PDA is often found in late stages, investigating the role that UPP1 plays in metastasis is an important area of study and one that our laboratory is actively pursuing.

Uracil accumulation upon uridine catabolism

UPP1 catabolizes uridine into uracil and ribose-1-phosphate. Thus far our studies have centered upon the fate of uridine-derived ribose. There has been little done to investigate the uracil component downstream of UPP1. While uracil has many uses in cellular processes, it is largely seen as a byproduct in uridine catabolism that is either recycled for pyrimidine synthesis or exists as a waste product[10]. From our studies in **Chapter 2** we observed an accumulation of UPP1-cleaved uracil both intracellularly and extracellularly, indicating that uracil is being transported out of the cell after uridine catabolism[2]. Preliminary studies from collaborators with our laboratory have seen a correlation between high extracellular uracil levels and metastasis in breast cancer models. Additionally, another set of collaborators have used stable isotope tracing on the nitrogen atoms in both uridine and uracil in glioblastoma cell lines and have seen that uridine-derived uracil is recycled back into pyrimidine pools, but exogenous uracil merely accumulates intracellularly. These findings and the large accumulation of uracil as a byproduct of our UPP1 studies have shaped future projects in our laboratory. Ongoing studies aim to investigate how this UPP1-cleaved uracil may play a role in metastasis in PDA.

The source of uridine in the TME

Our findings from **Chapter 2** demonstrate that uridine is imported into the cell and actively consumed by PDA as an energy source for central carbon metabolism. When measuring the levels of uridine in the tumor interstitial fluid (TIF) we observed these levels to be in the low micromolar range. Additional studies have shown uridine to be ~2-fold higher in the TIF than the plasma[11]. While we have demonstrated that PDA cells consume uridine, future studies are needed to determine the source of uridine within the TME. In our mouse models we observed immunocompetent mice to have reduced tumor growth upon UPP1 knockout. However, in our immunocompromised models we did not see this phenotype. The stark difference in phenotype may indicate that the immune compartment plays a role in supplying the uridine for uridine-driven metabolic growth. Previous datasets from our laboratory indicated that macrophages release uridine and uracil in vitro when differentiated and polarized[12]. However, when depleting macrophages from murine allograft tumors we observed a reduction in plasma uridine, but no alteration in TIF levels. Further studies into immune cell abundance in the TME and their potential excretion of uridine are ongoing in the laboratory, as these murine model differences are a key indicator of UPP1's relevant *in vivo*.

Ongoing collaborations in the laboratory present a potential source of uridine via cancer-associated fibroblasts (CAFs). These works elucidate a potential cellular crosstalk mechanism in which mitochondrial deficient or hypoxic cancer cells secrete the metabolites dihydroorotate and orotate which in turn are consumed by CAFs to produce and export uridine into the TME. These studies present a potential source of uridine in the TME, while simultaneously introducing another variable to our model in the form of hypoxia. Understanding the role of hypoxia in UPP1 is another area of active pursuit as it is well characterized that PDA exists in an extremely hypoxic TME.

Nutrient sensors regulate UPP1

Our studies have demonstrated that UPP1 expression is regulated by the MAPK signaling pathway and augmented by nutrient availability. However, the mechanisms for how UPP1 expression is altered by nutrient availability is still unknown and warrants future studies. An ongoing study to address this aims at investigating how the integrated stress response (ISR) affects UPP1 expression. The ISR is an elaborate signaling pathway which activates in response to a wide range of stimuli, including hypoxia, amino acid deprivation, endoplasmic reticulum (ER) stress, and oncogene activation, to name a few. These stimuli converge on the phosphorylation and activation of eukaryotic translation initiation factor 2 (eIF2α), which results in downstream activation of activating transcription factor 4 (ATF4) promoting cell survival and recovery[13,14]. Given that this response is integral to cell homeostasis and survival, and its stressors include nutrient deprivation, this is an important area of investigation for immediate follow-up studies stemming from our findings. The feedback mechanism of action to upregulate UPP1 in nutrient-depleted conditions could be elucidated by perturbation of the ISR. Understanding the nutrient sensor that regulates UPP1 in addition to MAPK signaling would further our characterization of PDA's dependency on uridine-driven metabolism significantly.

Further characterization of PDA via Biolog phenotyping assay

To comprehensively profile the nutrient inputs that PDA is capable of metabolizing in the absence of glucose we used carbon sources within the Biolog phenotyping assay. Alongside this we used CCLE gene expression data for all cell lines used in the assay and found a correlation between UPP1 and uridine consumption outlined in **Chapter 2**. Within these carbon datasets remain many future discoveries and areas of investigation for PDA metabolic profiling. One such is adenosine, which showed a varied response in consumption across cell lines. Adenosine is a purine nucleoside base that is highly utilized in metabolic processes, chief of which is its incorporation in the energy molecule ATP. Additionally, adenosine has been shown to be highly abundance in the TIF and functions to protect tumors against anti-tumoral immune cell response by T cells and NK cells[15]. Further exploration into the balance between consumption of adenosine to induce a mitochondrial response, as seen in the Biolog assay, versus the accumulation of extracellular adenosine levels to protect against T cell invasion may show targetable vulnerability, as this substrate is in demand for two distinct proposed mechanisms. This interplay may also explain the lower consumption of adenosine in a subset of PDA cell lines from our screen, so it would be informative to look at T cell infiltration in syngeneic mouse models from those cell lines.

In addition to the carbon and nitrogen substrates from the Biolog assay, there were a multitude of other conditions used in the large-scale screen that have yet to be analyzed. A panel of chemotherapy drugs was administered to all cell lines in nutrient-replete conditions to assess cytotoxicity. There was a varied metabolic response across cell lines, which was consistent with phenotypic clusters of cell lines throughout the Biolog screen. Overall, regardless of substrate given, cell lines clustered as either basal or classical PDA subtype, and either highly glycolytic or oxidative metabolically. While we expected the varied response among cell lines due to these classifications, the categorial variables were not considered in previous studies owing to the strong median phenotypes of the substrates being investigated. For chemotherapy responses, the relationships between PDA subtypes and metabolic response should be more heavily considered, as drug efficacy will likely be impacted and indicate specific vulnerability to a given subtype. From the analysis pipeline created in **Chapter 3** we can quantify a wide range of kinetics parameters from the Biolog assay, combine those with the background categorial variables from each cell line, and incorporate CCLE gene expression data to uncover many more relationships in PDA metabolism that warrant further investigation.

4.2 Conclusion

The work described herein has focused primarily on pancreatic cancer, its complex TME, and the nutrients capable of sustaining cancer cell metabolism. These aims provide significant findings to further PDA metabolism studies and potential therapeutic options. Through these works and my graduate studies, I have gained an appreciation for the complexity of cancer and its context dependent mechanisms. By altering existing biological processes and pathways, PDA effectively hijacks and repurposes an already well-established and efficient cellular infrastructure. Additionally, the TME provides a protective physical barrier against chemotherapies and immune cell penetration, and PDA upregulates scavenging pathways to counteract the hypoxic and serum-nutrient deprived environment. By profiling these metabolic differences via a wide range of metabolomics techniques and the Biolog phenotyping assay, we have made significant strides in further understanding another important pathway for altered PDA metabolism. Our findings demonstrate the importance of uridine in the TME and provoke many additional studies for the future. These studies also demonstrate our capabilities in interrogating metabolism through highly sophisticated and customizable metabolomics platforms that will continue to propel future studies in the laboratory.

4.3 References

1. Hanahan, D. & Weinberg, R. A. Hallmarks of cancer: the next generation. *Cell* **144**, 646–674 (2011).
2. Nwosu, Z. C. *et al.* Uridine-derived ribose fuels glucose-restricted pancreatic cancer. *Nature 2023 618:7963* **618**, 151–158 (2023).
3. da Silva, E. F. G. *et al.* CPBMF65, a synthetic human uridine phosphorylase-1 inhibitor, reduces HepG2 cell proliferation through cell cycle arrest and senescence. *Invest New Drugs* **38**, 1653–1663 (2020).
4. Gonçalves da Silva, E. F. *et al.* Therapeutic effect of uridine phosphorylase 1 (UPP1) inhibitor on liver fibrosis in vitro and in vivo. *Eur J Pharmacol* **890**, 173670 (2021).
5. Renck, D., Ducati, R. G., Palma, M. S., Santos, D. S. & Basso, L. A. The kinetic mechanism of human uridine phosphorylase 1: Towards the development of enzyme inhibitors for cancer chemotherapy. *Arch Biochem Biophys* **497**, 35–42 (2010).
6. Pereira, M. A. & Chio, I. I. C. Metastasis in Pancreatic Ductal Adenocarcinoma: Current Standing and Methodologies. *Genes (Basel)* **11**, (2020).
7. Hapach, L. A., Mosier, J. A., Wang, W. & Reinhart-King, C. A. Engineered models to parse apart the metastatic cascade. *npj Precision Oncology 2019 3:1* **3**, 1–8 (2019).
8. Rasheed, Z. A. *et al.* Prognostic significance of tumorigenic cells with mesenchymal features in pancreatic adenocarcinoma. *J Natl Cancer Inst* **102**, 340–351 (2010).
9. Puleo, F. *et al.* Stratification of Pancreatic Ductal Adenocarcinomas Based on Tumor and Microenvironment Features. *Gastroenterology* **155**, 1999-2013.e3 (2018).
10. Vértessy, B. G. & Tóth, J. Keeping Uracil Out of DNA: Physiological Role, Structure and Catalytic Mechanism of dUTPases. *Acc Chem Res* **42**, 97 (2009).

11. Sullivan, M. R. *et al.* Quantification of microenvironmental metabolites in murine cancers reveals determinants of tumor nutrient availability. *Elife* **8**, (2019).

12. Halbrook, C. J. *et al.* Macrophage-Released Pyrimidines Inhibit Gemcitabine Therapy in Pancreatic Cancer. *Cell Metab* **29**, 1390-1399.e6 (2019).

13. Pakos-Zebrucka, K. *et al.* The integrated stress response. *EMBO Rep* **17**, 1374 (2016).

14. Palam, L. R., Gore, J., Craven, K. E., Wilson, J. L. & Korc, M. Integrated stress response is critical for gemcitabine resistance in pancreatic ductal adenocarcinoma. *Cell Death Dis* **6**, (2015).

15. Hoskin, D. W., Mader, J. S., Furlong, S. J., Conrad, D. M. & Blay, J. Inhibition of T cell and natural killer cell function by adenosine and its contribution to immune evasion by tumor cells (Review). *Int J Oncol* **32**, 527–535 (2008).